ABSTRACT

Title of dissertation: MATHEMATICAL MODELS
FOR OVARIAN CANCER

Dana-Adriana Botesteanu
Doctor of Philosophy, 2017

Dissertation directed by: Professor Doron Levy
Department of Mathematics

Ovarian cancer is the most fatal cancer of the female reproductive system. High-grade serous ovarian cancer (HGSOC) represent the majority of ovarian cancers and accounts for the largest proportion of deaths from the disease. From a clinical perspective, the complex, heterogeneous behaviors of this women's cancer pose questions that cannot always be answered with contemporary clinical and experimental tools.

Studying the growth, progression, and dynamic response to treatment of ovarian cancers in an integrated systems biology/mathematical framework offers an innovative tool at the disposal of the oncological community to further exploit readily available clinical data and generate novel testable hypotheses. Developing novel

physiologically structured mathematical models to study the heterogeneous behavior of this malignancy would help us to better understand patient therapeutic responses and devise novel combination therapies.

As a first step, we developed a mathematical model for a quantitative explanation why transvaginal ultrasound-based (TVU) screening fails to improve low-volume detectability and overall survival (OS) of HGSOC. This mathematical model can accurately estimate the efficacy of screening for this cancer subtype. The model also explains the observed heterogeneity in cancer progression and duration of the pre-diagnosis stage. Our mathematical model is consistent with recent case reports and prospective TVU screening population studies, and provides support to the empirical recommendation against frequent HGSOC screening.

At the cell population level, we have quantitatively investigated the role of cell heterogeneity emerging from variations in cell-cycle parameters and cell-death. Many commonly used chemotherapeutic agents in treating ovarian cancers target only dividing cancer cells.

We recently demonstrated in a mathematical model, calibrated against published *in vitro* cell culture data, that resistance to chemotherapeutic treatment may arise from a dynamic, oscillatory balance between the dividing and non-dividing cancer cells, which is conserved through time despite high long-term drug dosages.

At the single cell level, we developed a mathematical model to explain the emerging heterogeneity in individual cancer cell responses to drugs targeting the cell-cycle, which have a broad spectrum of anti-tumor activity in ovarian cancers. This emerging heterogeneity remains a poorly understood mechanism that plays a significant role in mediating drug response, and predicts the existence of an intrinsic resistance mechanism to drug therapy.

The model incorporates an intrinsic form of heterogeneity via the duration of time single cells spend in mitosis. It uses published single cell *in vitro* experimental data for calibration. Herein, the goal is to better understand why, within a distinct cell line, cells treated with identical drugs exhibit a considerable degree of heterogeneity in response to prolonged drug exposure. The model can serve as a basis for future studies of the heterogeneity observed *in vitro* of more complex responses to anti-mitotic drugs of different cell lines.

Studying the natural history, growth, and progression of ovarian cancers in an integrated systems biology/mathematical framework represents a complementary tool that can be used to provide valuable insights into the treatment of HGSOC.

My work focuses on developing and applying quantitative, integrated mathematical modeling frameworks to pre-clinical and clinical data, in order to better understand ovarian cancer dynamics and develop new therapeutics.

MATHEMATICAL MODELS FOR OVARIAN CANCER

by

Dana-Adriana Botesteanu

Dissertation submitted to the Faculty of the Graduate School of the
University of Maryland, College Park in partial fulfillment
of the requirements for the degree of
Doctor of Philosophy
2017

Advisory Committee:
Professor Doron Levy, Chair/Advisor
Professor Maria Cameron
Professor Wolfgang Losert
Professor Matei Machedon
Professor Kasso Okoudjou

Dedication

"Two roads diverged in a wood, and We -

We took the one less traveled by,

And that has made all the difference."

(adapted from "The Road Not Taken", Robert Frost)

To my wonderful and beautiful partner, A,

My best friend and teammate,

Whose love, support and encouragement

Inspire me to pursue new heights.

You are my admiration and inspiration.

Acknowledgments

I am extremely grateful to all the people who have made this thesis possible and who have supported me throughout my graduate experience.

First and foremost, I would like to gratefully acknowledge the guidance, support and encouragement of my doctoral advisor, Professor Doron Levy. His knowledge, feedback and mentorship have been invaluable throughout the years. I am especially grateful for his continued support in my scientific endeavors, and for him allowing me the intellectual freedom to explore my interest in Mathematics and in Oncology throughout my work. I am also very thankful for his supporting my attendance at various national and international conferences, and for his encouraging me to push boundaries in Mathematical Oncology.

I would also like to thank Dr. Jung-Min Lee for her continuous support, mentorship, and collaboration. I am extremely grateful for her willingness to share with me her clinical expertise, enthusiasm for science, and for her patience in nurturing my interest in oncology. I am also very thankful for her encouraging and engaging me in new ideas and approaches in Mathematical Oncology. I am extremely grateful for her friendship and am very lucky to have met her.

Many thanks are due to Professor Maria Cameron, Professor Wolfgang Losert, Professor Matei Machedon and Professor Kasso Okoudjou for agreeing to serve on my dissertation committee and for sparing their precious time reviewing my dissertation work.

My gratitude extends to Professor Konstantina Trivisa, Jessica Sadler, Alverda

McCoy and Christiana Sabett for their prompt responses in providing assistance with administrative tasks, and most importantly, for making AMSC the successful and nurturing Ph.D. program every Ph.D. student should be a part of. Many thanks to Dorothea F. Brosius for preparing the LaTeXtemplate for this dissertation.

I am very thankful to my colleagues in the Women's Malignancies Branch at NCI, the present and past members of the Lee Lab, for creating a welcoming, friendly and cooperative atmosphere in the lab and also for their useful feedback and insightful comments on my work. I would also like to thank Dr. Stanley Lipkowitz for his support and feedback, Professor Matei Machedon for his support and mentorship, and Professor Harriet Pollatsek for her gentle guidance and support throughout the years.

I would also like to acknowledge the financial support from the Graduate School at the University of Maryland, College Park through the Wylie Dissertation Fellowship, the Jayne Koskinas and Ted Giovanis Foundation and the National Science Foundation through the grant number DMS-0758374. I am also indebted to the UMD-NCI Partnership for Integrative Cancer Research for the financial support and for the scientific growth and incredible opportunities at NCI that it offers.

Finally, I would like to acknowledge and thank Geoff Clapp, Jim Greene, Kilian Cooley, Rhyneta Gumbs, Weilin Li, Dimitris Ntogkas, Christiana Sabett, Alexandra Sarpe, Lucia Simonelli, Colleen Stock, and Matt Whiteway for their constant support, insightful discussions and friendship. My gratitude also extends to Ted and Tracy Whiteway for their love and support.

I am extremely lucky and humbled to have met during Thanksgiving 2008 my

American host family, Natalina and Lou Tulik, their daughters Joana and Sofia, and Soupy Tulik, whom I miss, looking up in the skies. They are my second family, and some of the most loving, caring and beautiful people I have ever met.

I owe my deepest thanks to my grandmother Cristina, whom I miss and think about every day, and to my mother Carmen, both of whom have always believed in me and have been there for me with their love, advice and support countries and continents away.

Table of Contents

List of Tables

List of Figures

List of Abbreviations

BRCA1	BReast CAncer Susceptibility Gene 1
BRCA2	BReast CAncer Susceptibility Gene 2
CA125	Cancer Antigen 125
CCR	Center for Cancer Research
CDF	Cumulative Distribution Function
Cdk1	Cyclin-dependent kinase 1
DNA	DeoxyriboNucleic Acid
HGSOC	High-Grade Serous Ovarian Cancer
HR	Homologous Repair
HRD	Homologous Recombination Repair Deficiency
MOMP	Mitochondrial Outer Membrane Permeabilization
NIH	National Institutes of Health
OS	Overall Survival
PARP	Poly ADP-Ribose Polymerase
PARPi	Poly ADP-Ribose Polymerase Inhibitor
PD-L1	Programmed Death Ligand-1
PLCO	Prostate, Lung, Colorectal and Ovarian Cancer Screening Trial
RMSE	Root Mean Square Error
SAC	Spindle Assembly Checkpoint
TD	Time until Detection
TKI	Tyrosine Kinase Inhibitor
TLV	Time until Life threatening tumor Volume is reached
TVU	Transvaginal Ultrasound
UKCTOCS	UK Collaborative Trial of Ovarian Cancer Screening
US	United States
USFDA	United States Food and Drug Administration
USPSTF	United States Preventive Services and Task Force

VEGFR	Vascular Endothelial Growth Factor Receptor
WMB	Women's Malignancies Branch
WOP	Window Of Opportunity

Chapter 1: Introduction

The goal of this dissertation is to develop and apply mathematical models to study ovarian cancer. It takes an interdisciplinary approach, combining modeling with experimental data, i.e., *in vitro* or *in vivo* data in order to investigate diverse aspects of ovarian cancer growth dynamics, detection and therapeutic administration. The clinical background presented in this chapter constitutes the motivation and foundation of the models subsequently presented.

1.1 Motivation

Women constitute the majority of the aging United States (US) population, as, on average, they outlive men by 5 years [1]. According to the US Bureau of the Census in 2010, the life expectancy of a female at birth was 81.1 years versus 76.2 years for a male. In this latest census, women accounted for about 60% of the population aged 70 years or older.

Based on these demographic data, the computed ratio of number of post-menopausal women to women of reproductive age was 2:3. This has substantial implications on existing clinical practices, since an increased proportion of aging women is associated with new disease patterns, such as differential incidence or prevalence rates [2,3].

Ovarian cancer is a relatively rare women's cancer, representing 1.3% of all new cancer cases in US women [4]. However, it is the most fatal gynecologic cancer type, with an $\approx$ 46.5% five-year overall survival rate [4]. Ovarian cancer is most frequently diagnosed among women aged 55-64, with a median age of 63 years [4].

From a clinical perspective, the complex, heterogeneous behaviors of this subset of women's cancers pose questions that cannot always be exclusively and feasibly answered with contemporary clinical and experimental tools. Studying the origins, growth, progression, and dynamic response to treatment ovarian cancers in an integrated systems biology/mathematical framework offers an innovative tool at the disposal of the oncological community to further exploit readily available clinical data, generate novel testable hypotheses or re-interpret existing experimental data [2].

My dissertation research involves developing novel physiologically structured mathematical models to study the heterogeneity in ovarian cancer initiation, progression and therapeutic responses.

1.2 Introduction to Human Ovarian Cancers

By the end of 2017, it is estimated that 22,440 new cases of ovarian cancer with an estimated 14,080 deaths related to this disease will occur in the US, for a computed 2:3 death to incidence ratio [4]. The high mortality rate following diagnosis has been partly attributed to the approximately two thirds of patients presenting with advanced stage, when recurrence is common and ultimately leads to the incurable disease.

The absence of accurate early detection screening methods poses additional difficulties in reducing ovarian cancer mortality levels [5]. Several studies suggest the usefulness of a symptom index tool to identify women who may have ovarian cancer; this includes new (within 1 year) and persistent (more than 12x/month) pelvic/abdominal pain, abdominal size/bloating, difficulty eating/feeling full, and urinary urgency/frequency [6, 7], which should trigger evaluation by a gynecologic oncologist. Surgical debulking is an integral part of the management of ovarian cancer patients. The extent and quality of the debulking has important prognostic value.

1.3 The Target Organ(s)

It is becoming increasingly recognized that ovarian cancers do not constitute a single disease, but rather a family of non-uterine tubo-ovarian cancers (see Figure 2 in [2]).

Ovarian tumors may develop from epithelial, stromal or germ cells [8]. About 10-15% of all ovarian malignant tumors are non-epithelial in origin, are often found at an early stage, and generally have a good prognosis [9]. Epithelial ovarian cancers constitute about 85 - 90% of all ovarian cancer cases, with a subset of these epithelial ovarian cancers, high-grade serous ovarian cancers (HGSOCs), representing nearly 70% of all ovarian cancer cases.

HGSOC is considered to be an aggressive histological subgroup of the ovarian malignancies [10]. Although the 5-year survival rate for stage I ovarian cancer is greater than 80% [11], stage I diagnoses represent the exception rather than the rule [4]. Most patients present with stage III/IV tumors, for which the 5-year survival rate is less than 30% [4].

One of the obstacles to the detection of early-stage HGSOC has been the poor understanding of its histopathogenesis. It was initially thought that epithelial ovarian tumors originate from the ovarian surface epithelium, a single cell layer covering the ovaries, coming from the coelomic epithelium [12, 13].

Recent data suggest secretory cells inside the distal Fallopian tubes give rise to the earliest precursor lesions in a proportion of HGSOC cases [12–15]. This finding was first reported in women with germline *BRCA1* and *BRCA2* mutations undergoing a prophylactic bilateral risk-reducing salpingo-oophorectomy procedure [16–18]. For the general-risk population however, it remains unclear whether diagnosed ovarian tumors commonly arise with apparently Fallopian tube involvement, or constitute truly ovarian-derived diseases.

1.4 Prophylactic and Early Detection Strategies

Any proposed screening strategy should be highly sensitive and specific to detecting truly malignant ovarian cancer cases. Transvaginal ultrasound (TVU), serum biomarkers (e.g., CA125, HE4) testing, pelvic examinations or simultaneous TVU and CA125 testing have been examined as non-invasive tools for detecting early stage ovarian cancer in general-risk women.

However, recent evidence suggests that annual screening with TVU and serum biomarkers does not reduce mortality [19]. Furthermore, high false positive rates leading to intervention are associated with potential harm, such as unnecessary surgical intervention and related complications.

The lack of utility of such screening tools is possibly due to the absence of adequate TVU sensitivity in detecting small increases in tumor volume and distinguishing between malignant and benign cases [20]. Furthermore, the addition of serum biomarkers testing (e.g., CA125 levels) does not improve early-stage detection levels either [21, 22].

The largest ever ovarian cancer screening study of 202,638 general-risk women demonstrated that multimodal screening including serial TVU and CA125 level testing yielded a 15% mortality reduction rate compared with a 0% no screening or 11% unimodal TVU-based screening cohort mortality reduction rate over 0-14 follow-up years [19, 23].

However, this study also showed increased CA125 levels can be detected in benign conditions, rendering it inadequate for use in screening asymptomatic women for early-stage ovarian cancer. The lack of adequate early-detection tools might also be explained by the fact that any epithelial ovarian cancers diagnosed in stage I might be fundamentally different from those diagnosed in advanced stages, which are preponderantly high and not low-grade cases [24, 25].

United States Preventive Services and Task Force (USPSTF) has recently reconfirmed their previous recommendation against screening in asymptomatic women without known genetic risk for ovarian cancer [26]; existing screening methods are either not recommended as uni- or multimodal prognostic markers for low HGSOC volume detection [27–29], or have not been shown to confer a mortality benefit in general-risk women [30]. High-genetic risk women should be considered for genetic counseling [31] and offered the option to undergo regular monitoring via a combination of TVU examinations and CA125 tests.

Many high-genetic risk women voluntarily choose to undergo various risk-reducing gynecologic surgeries, such as prophylactic oophorectomies, bilateral salpingo-oophorectomies or hysterectomies [32–35], which have been proven to reduce mortality from both breast [13, 36–38] and ovarian cancer [37, 38]. Collectively, the question of whether ovarian cancer is a valid target for routine screening in general- or high genetic-risk women remains highly controversial [28, 39, 40].

1.5 Current Treatment Strategies

Standard treatments for ovarian cancers include debulking surgery, (neo)adjuvant platinum-based combination chemotherapy, such as cisplatin or carboplatin, and a taxane such as paclitaxel or docetaxel [41]. In addition to systemic chemotherapy, targeted therapies such as small molecule tyrosine kinase inhibitors are also used. For example, platinum-resistant recurrent ovarian cancers have been shown to respond to angiogenesis inhibitors (e.g., bevacizumab) in combination with chemotherapy, [42, 43].

Additionally, poly ADP-ribose polymerase (PARP) inhibitors have been used in clinical trial settings and the PARP inhibitor (PARPi) olaparib (Lynparza) was recently approved by the US Food and Drug Administration (USFDA) as a therapy for germline BRCA-mutations associated recurrent ovarian cancer [44, 45].

1.6 Drug Resistance: Implications for Predicting Recurrence

Initial response rates to current standard treatments for ovarian cancer patients are high (70%-80%), but the majority of women with advanced disease relapse with within two years [46]. Recurrent ovarian cancer is not curable, and most women eventually develop a platinum-resistant disease.

Several mechanisms of cellular resistance to platinum compounds or PARPis have been described [47], such as intracellular cisplatin inactivation via augmented glutathione synthesis [48, 49], or reduced intracellular drug concentration via overexpression of MDR1 protein acting as a drug efflux transporter [50]. Another possible mechanism of platinum resistance is the development of secondary mutations restoring functions of BRCA and other proteins of homologous recombination repair (HR) in *BRCA*-mutated ovarian cancers.

However, BRCA restored functionality does not explain all cases of cisplatin resistance in these patients [51–53], since not all platinum-resistant recurrent ovarian carcinomas exhibit detectable secondary mutations.

Norquist*et al.* showed only 12 of 26 (46%) platinum-resistant recurrent cases had detectable secondary mutations restoring BRCA function [54]. Further preclinical and clinical investigations of mechanisms of platinum or PARPi resistance are thus needed.

Larger-scale prospective and retrospective cohort studies are warranted in order to better examine therapy response heterogeneity and adaptability of the ovarian cancer genome under the selective pressure of cytotoxic therapies [55–57].

1.7 Outline of Thesis

The remainder of this thesis is organized as follows. In Chapter 2, we review and provide a detailed description of the existing mathematical models aimed at describing various aspects of ovarian cancer's natural history and progression. This review was published in [2]. We then focus on a mathematical study of ovarian cancer initiation, progression, and detection *in silico* in Chapter 3. These results were published in [58]. Chapter 4 presents a mathematical study of ovarian cancer cellular population growth dynamics and therapeutic administration *in vitro*. These results were published in [59]. We then provide a single-cell analysis of cell fate kinetics in response to prolonged exposure to therapy in Chapter 5. These results were submitted for publication [60]. Finally, we provide concluding remarks and discuss future directions in Chapter 6.

Chapter 2: Mathematical Models of Ovarian Cancers

This review of mathematical models of ovarian cancers was published in [2].

2.1 Overview

In order to systematically investigate the complexity of cancer progression and response to treatment in ovarian malignancies, integrated mathematical modeling frameworks viewed from a systems biology perspective are needed. Such integrated frameworks can offer innovative contributions to the clinical women's cancers community, since answers to clinical questions cannot always be reached with contemporary clinical and experimental tools.

In the present chapter, we will focus on mathematical models of ovarian cancer dynamics, and not on statistical modeling (e.g., absolute risk prediction models, or multiple regression analyses assessing epidemiologic risk factors), or specific algorithmic approaches (e.g., machine-learning approaches to specifying rules for genetic and molecular stratification of individual patients). Additionally, we will differentiate between mathematical modeling of cancer dynamics or drug resistance and other related topics such as cancer imaging or detection algorithms, in which mathematics has historically played an instrumental role [61, 62].

Considerable mathematical modeling effort has been directed so far towards modeling carcinogenesis, cancer progression, and cancer treatment [61, 63–70]. Relatively few mathematical investigations, however, have specifically targeted ovarian cancers.

After a comprehensive literature search, we note that, to best of our knowledge, the models presented below represent the majority of the published ovarian cancer mathematical models. We thus chose to discuss these mathematical models in detail, and highlight areas where extensions to these *in silico* modeling frameworks could be further developed.

2.2 Modeling Disease Natural History and Early Detection Strategies

Focusing exclusively on unimodal TVU screening, Danesh *et al.* developed a mathematical model to study the frequency at which ovarian cancer screening should be done in order to be effective [71]. To model ovarian cancer growth and progression, Danesh *et al.* [71] developed a multi-type branching processes model, where the different types represent stages in the serous epithelial ovarian cancer progression, without differentiating between the low and high-grade subtypes.

In their model, type 0 cells are present in the primary tumor in the ovary or Fallopian tube, type 1 cells are floating in the abdominal cavity, and type 2 cells are attached to the peritoneum. Type 2 cells are assumed to infiltrate the extracellular matrix and eventually metastasize to distant organs, so that when they are present in significant (and clinically detectable) numbers, the cancer would be classified as stage III.

Therein, cells can transition from type 0 to type 1 and from type 1 to type 2 at differential rates, or give birth to nonmutant offspring or die. The transition rates between the different cell types were used as rates in a continuous time Markov chain. In this model, the transitions between cellular types are assumed to involve migration of cells rather than genetic mutations.

Below, the theorems for the multi-type branching process between cellular types enable Danesh *et al.* to quantitatively estimate the behavior of all three cell types [71].

[Theorem 2.2.1, [71]]

$Z_0(t) \sim V_0 \mathrm{e}^{\lambda_0 t}$ with $V_0 \overset{d}{\sim} \frac{b_0}{a_0}\delta_0 + \frac{\lambda_0}{a_0}\exp(\frac{\lambda_0}{a_0})$. Here, δ_0 is a point mass at 0, corresponding to the event that the branching process dies out, a_0 represents the birth rate of the type 0 cells, and $\exp(r)$ is the exponential distribution with density function $re(-rt)$.

[Theorem 2.2.2, [71]]

The function $\frac{Z_1(t)}{EZ_1(t)} \to 1$ in probability as t $\to \infty$.

[Theorem 2.2.3, [71]]

$\mathrm{e}^{-\lambda_2(t-s_2)}Z_2(t) \to V_2$, where V_2 is the sum of points in a Poisson process with mean measure $\mu_2(x,\infty) = C_2 x^{-\alpha_2}$, where $\alpha_2 = \frac{\gamma_1}{\lambda_2}$, $C_2 = \frac{1}{\alpha_2}(\frac{a_2}{\lambda_2})^{\alpha_2}\Gamma(\alpha_2)$, and $\Gamma(r) = \int_0^\infty t^{r-1}\mathrm{e}^{-t}dt$ is the Gamma cumulative distribution function (CDF).

In the theorems above, type i cells proliferate with rate a_i and die with rate b_i, yielding a net growth rate of $\lambda_i = a_i - b_i$. Herein, the primary tumor cells grow with rate λ_0, and shed with rate u_1 moving into the peritoneal cavity. There, they grow with rate λ_1, and shed with rate u_2 into secondary sites, where they grow with rate $\lambda_2 > \lambda_0$.

In order to address their motivating question (i.e., can ovarian cancer be detected early or not?), Danesh *et al.* introduced the concept of a "window of opportunity" for screening. It is defined as the difference between the time when cells of type 2 reach 10^9 cells (corresponding to a late-stage tumor) and cells of type 0 reach $6.5 \cdot 10^7$ cells (corresponding to the detection threshold).

Using data on tumor growth from Brown and Palmer [72], they concluded that the window of opportunity corresponds, on average, to 2.9 years, with most of the distribution concentrated between 2.5-3 years. According to their model, TVU-based ovarian cancer screening should occur biannually.

The underlying assumption in the Danesh *et al.* modeling framework is that metastatic ovarian cancer cells growth at a significantly higher rate than primary tumor cells. This assumption has yet to be validated clinically.

In contrast to the dynamics portrayed in this work, it is generally believed that ovarian cancers that present clinically during early stages do not necessarily represent precursors to cancers that, if left undetected, would otherwise present at advanced stages [73, 74].

Moreover, the theoretical results derived assume exponential stage residence times and an infinite time period when determining cancer growth and progression. Using non-exponential growth kinetics and a finite observation time (as done empirically) could alter the modeling outcomes.

Finally, in contrast to the biannual TVU-based ovarian screening recommendation based on the Danesh *et al.* modeling inferences, latest data from ovarian cancer screening randomized controlled trials demonstrate the failure of annual, unimodal TVU examinations to improve ovarian cancer detectability and overall survival rates [19, 30].

In another attempt to model the preclinical natural history of serous epithelial ovarian cancer as a function of tumor size, stage and its implications for TVU-based screening [72], Brown and Palmer identified and analyzed available reports on occult ovarian cancers, and used the data in a comprehensive meta-analysis of published data to model the growth, progression and TVU-based detection of ovarian cancer [13, 35, 36].

Data were collected from published studies of healthy germline *BRCA1* and *BRCA2* mutation carriers [38, 75], who had their ovaries and Fallopian tubes removed prophylactically. In some of these women, unsuspected ovarian cancers were discovered upon surgery [76].

Brown and Palmer performed a Monte Carlo simulation of tumor life histories to fit an exponential *in silico* model for tumor growth using parameters derived from their meta-analysis, with separate growth rate parameters for early and advanced stage cancers. A basic description of the theoretical tumor growth model proposed by Brown and Palmer is the following:

$$\log \text{size} = a + bt_1, \tag{2.1}$$

$$\log \text{size} = c + bt_2. \tag{2.2}$$

Herein, tumors in both early and advanced stages are assumed to grow exponentially. Specifically, the early stage tumor growth model is illustrated in Equation (2.1). Therein, a is the size at which a particular tumor is detectable by histopathology, b is the (exponential) growth rate constant and t_1 is the time since the tumor became detectable by histopathology. Detection thresholds for each individually simulated growth curve were set to match the corresponding value found in the collected tumor dataset.

The advanced stage tumor growth model is illustrated in Equation (2.2). Therein, c is the log value of the tumor size at disease progression from early to advanced stage (estimated from the Monte Carlo simulation of tumor life histories), d is the difference between the log values of the tumor size at empirical diagnosis obtained from the collected tumor dataset and the log value of the size at progression from the generated simulation. Lastly, t_2 is the *in silico* measured time since progression.

In this model, the “window of opportunity” was defined as the time duration for early detection, i.e., the time during which the tumor is expected to remain early stage (localized or regional). They estimated the window of opportunity for TVU detection of early stage cancers to be around 4.3 years, and predicted that most detected advanced stage serous cancers would have become advanced a median of 0.8 years prior to detection.

Similar to the Danesh *et al.* model, the underlying assumption in the Brown and Palmer quantitative analysis is that ovarian cancers that are clinically present during early stages are precursors to cancers that if left undetected, would otherwise present at an advanced stage. We point out that a timely detection of low volume ovarian cancer, which does not necessarily represent early stage disease, should be the goal of any screening studies as well as of any mathematical modeling framework aimed at exploring screening scheduling.

To assess dynamic plasma biomarker kinetics in relation to the genesis of cancer, Hori and Gambhir incorporated tumor growth into a linear one-compartment biomarker secretion model, beginning with a single parental tumor cell1 [77]. They aimed to quantify the time required for a growing malignant tumor cell population to reach a sufficient size so that its shed blood biomarker levels were high enough to be detectable by current clinical blood biomarker assays.

The model was used to calculate changes in the detection capability based on log-order perturbations in the parameters related to biomarker shedding. Tumor cell growth was represented by either the exponential or Gompertzian model, while the healthy cell population was assumed constant.

The plasma biomarker temporal dynamics model of Hori and Gambhir is illustrated below.

$$\frac{dq_{PL}(t)}{dt} = u_T(t) + u_H(t) - k_{EL}q_{EL}(t), \tag{2.3}$$

$$u_T(t) = f_{PL,T}R_TN_T(t), \tag{2.4}$$

$$u_H(t) = f_{PL,H}R_HN_H(t), \tag{2.5}$$

$$N_T(t) = N_{T,0}\mathrm{e}^{\left[\frac{\mathrm{k_{GR}}}{\mathrm{k_{decay}}}(1-\mathrm{e}^{-\mathrm{k_{decay}}t})\right]}, \tag{2.6}$$

$$N_T(t) = N_{T,0}\mathrm{e}^{\mathrm{k_{GR}}t}, \tag{2.7}$$

The change in the mass of the plasma biomarker with respect to time is equal to the difference between the influx of plasma biomarker shed by the tumor cells, $u_T(t)$, healthy cells, $u_H(t)$ and the outflux of biomarker from the plasma, $q_{EL}(t)$. This phenomenon is illustrated in Equation (2.3).

The rate of biomarker entry into the plasma is the sum of the input from tumor cells (as modeled in Equation (2.4)) and from healthy cells (as modeled in Equation (2.5)). Tumor cell growth is represented here by either the Gompertzian growth model (see Equation (2.6)), or the exponential growth model (see Equation (2.7)). The healthy cell population is assumed to remain constant throughout simulation time, and is set at $N_H(t) = N_{H,0}$.

Hori and Gambhir aimed to identify the biomarker-related parameters that would most greatly impact blood-based early cancer detection. Specifically, their goal was to quantify how far each baseline parameter value would need to change in order to achieve earlier, sub-millimeter tumor detection. It was found that tumors in the mm diameter range could only be detected under ideal conditions of extremely high rates of biomarker secretion by tumor-associated cells and zero background level from healthy cells.

Hori and Gambhir thus concluded that clinical implementation of a CA125 biomarker-based early serous epithelial ovarian cancer detection would be extremely difficult for the time being. We note that the relationship between tumor sizes and

CA125 biomarker levels is not entirely understood [30] and serial CA125 measurements are not common practice [19, 23, 78]. Further modeling efforts could potentially drive further cohort screening studies.

2.3 Modeling Therapeutic Targeting and Treatment

A key question related to optimal sequencing and scheduling of chemotherapy and surgery is whether the optimal therapeutic strategy would be to maximally debulk a cancerous tumor followed by chemotherapy or vice versa [79–81].

Kohandel *et al.* [82] considered one population of tumor cells, a non-cell cycle phase specific drug, and various growth/cell-kill laws in order to compare two approaches for therapy: a) chemotherapy followed by surgery, or b) surgery followed by chemotherapy.

The authors combined Gompertzian and generalized logistic growth models with different cell-kill hypotheses, and assumed that surgery instantaneously kills a fraction of the tumor cells at the time of the treatment. For both the Gompertzian and generalized growth models, chemotherapy followed by surgery proved to be the optimal approach.

The one-compartment ODE model of Kohandel *et al.* is illustrated below.

$$\frac{dN}{dt} = f(N) - G(t, N) - k_s I(t = \mathrm{t}_{\mathrm{surgery}})N, \tag{2.8}$$

$$G(t,N) = \begin{cases} c(t)N, & \text{if } \log-\text{kill model}, \\ c(t)f(N), & \text{if NS model}, \\ c(t)\frac{N}{N+\delta}, & \text{if } E_{max} \text{ model} \end{cases} \tag{2.9}$$

Equations (2.8)-(2.9) govern the dynamics of the tumor growth, under the surgical and chemotherapeutic treatments. Specifically, the dynamics of the number of tumor cells at time t, $N(t)$, is described by differential functional forms for the growth law, where $f(N)$ is the tumor cell growth dynamics (e.g., $f(N) = aN$ for the exponential growth law, where a is the constant proliferation rate). Moreover, $G(t,N)$ describes the effects of the drug on the system , and $I(t = \text{t}_{\text{surgery}})$ is an indicator function (equal to 1, if $t = \text{t}_{\text{surgery}}$, and 0 otherwise). Possible differential functional forms for $G(t,N)$ are provided in Equation (2.9). Surgery is assumed to be instantaneous, and to remove a fixed fraction of ek_s of tumor cells, where k_s is the fraction of removed cells during surgery.

The results presented are general and independent of a particular choice of parameters or drug administration protocols. However, in contrast to the mathematical modeling results, recently performed meta-analyses of randomized trials comparing chemotherapy versus surgery for initial treatment in advanced ovarian epithelial cancer [83] as well as locally advanced breast cancer [84] showed no difference between the two clinical scenarios in terms of survival or overall disease progression.

We note that a key assumption of the Kohandel *et al.* model is that chemotherapy administered prior to surgery solely alters primary tumor growth, rather than also affecting the formation and growth of (micro)metastatic tumor foci, which could be clinically occult at the time of surgery.

The clinical rationale for adjuvant chemotherapy (i.e., after surgical resection) is to eliminate any systemic, distant microscopic disease that would most likely already be present pre- or post-surgical resection. A future mathematical investigation based on the Kohandel *et al.* model could, for example, address the open clinical question of how to reliably identify the subsets of patients without any microscopic, residual disease, who would not benefit from adjuvant chemotherapy.

In a different attempt to model combination therapy, Jain *et al.* developed a mathematical model of ovarian cancer xenograft growth to study the effect of carboplatin and ABT-737, a small-molecule inhibitor of anti-apoptotic proteins Bcl-2 and Bcl-xL, on tumor growth inhibition [85].

Their model of ovarian cancer growth and treatment was based on a coupled system of ODEs and PDEs [86, 87], representing the temporal dynamics of proliferating and arrested cancer cells, and using the concentrations of the two drugs inside the peritoneum, plasma and tissue.

This combination therapy model carefully accounted for the pharmacodynamics and pharmacokinetics of both drugs, and was calibrated against *in vivo* experimental data collected from xenografted mice treated with carboplatin and/or ABT-737 on a fixed period schedule [85]. Their goal was to study dosage/timing combinations of the two drugs leading to the fastest time to minimal residual disease, or to the minimization of total drug in order to achieve a predetermined tumor growth inhibition.

Simulations of the Jain *et al.* model suggested that when combined with ABT-737, the infusion time of carboplatin doses together with the AUC of the drug were the most important predictors of the tumor long-term response to the combination therapy.

While the model is validated by *in vitro* ovarian cancer cell lines xenografted from patient ascitic tumor cells, further clinical investigations are needed to explore and examine the synergy between carboplatin and Bcl-2 family inhibitors.

Lastly, a two-compartment linear ODE model proposed by Panetta attempted to mathematically derive optimal treatment strategies in the sense of promoting the largest ovarian tumor cell burden reduction [88]. The two-compartment cell cycle framework modeled by Panetta is the following:

$$\begin{bmatrix} \frac{dP}{dt} \\ \frac{dQ}{dt} \end{bmatrix} = \begin{bmatrix} \gamma - \alpha - \delta - sf(t) & \beta \\ \alpha & -\beta - \lambda \end{bmatrix} \begin{bmatrix} P \\ Q \end{bmatrix} \tag{2.10}$$

$$f(t) = \begin{cases} \frac{T}{a}, \text{ if } nT \leq t \leq a, \\ 0, \text{ if } a + nT < t \leq (n+1)T. \end{cases} \tag{2.11}$$

In the system of equations illustrated in Equation (2.10), P is the number of proliferating tumors cells, and Q is the number of quiescent tumor cells. Additional parameters include γ, the growth rate of proliferating cells, α, the transition rate from the proliferating to the quiescent compartment, δ, the natural proliferating cell death rate, β, the transition rate from the quiescent to the proliferating compartment, and λ, the natural quiescent cell death rate.

All parameters in the model are assumed to be positive, and constant. Herein, the system outlined in Equation (2.10) represents a linear system of ODEs modeling the dynamics of the proliferating and quiescent cell compartments. The function $f(t)$ described in Equation (2.11) represents a step function describing the effects of the chemotherapeutic treatment, e.g., paclitaxel.

The periodic function modeling the paclitaxel effects is assumed to target only the proliferating cell compartment. In its functional representation, s is the strength of the drug, a is the active drug time, T is the period of paclitaxel administration and n stands for the n^{th} administered drug dose.

Using clinical variables such as treatment period, drug-infusion time, and proliferative fraction of ovarian cancerous cells, Panetta quantitatively demonstrated that for short periods (i.e., close to the active phase time) more drug is required in order to achieve a decay in the ovarian cancer cell population.

2.4 Modeling *In Vitro* Invasive Cancer Cell Kinetics

To simulate *in vitro* cancer-cell kinetics after cisplatin administration, Montalenti *et al.* developed a linear model of cell-cycle phase transitions based on experiments using IGROV-1 ovarian cancer cell line [89]. They used flow cytometry variables (derived experimentally) as the input to a quantitative description of the action of cisplatin on the carcinoma cells.

The aim was to specifically model the time between cell-cycle phases, delays and block-effects, with consequent repair or cell mortality following the exit from the blocks. It was assumed that drug administration forces cells to leave asynchronous growth, with the main effects being cell death, cell-cycle phase delays, or cell-cycle blocks. At the end of each cell-cycle phase, cells were assumed to progress to the next phase only if they passed an internal molecular checkpoint.

Montalenti *et al.* [89] considered various levels of complexity in their cell-cycle simulation: a) inter-cell differences in phase duration (modeled via a two-parameter probability distribution of the likelihood of a cell of a certain phase age leaving the specific phase); b) the probability that a cell can either bypass the quiescent phase or enter it for an indefinite period of time; and c) the probability that cells can be killed by cisplatin at a distinct rate in every phase, blocked but then repair damage and recycle, or frozen in a specific age compartment, inhibiting age maturation.

While a certain amount of information could be obtained by visual inspection of the raw experimental data performed and used, the task of the parameter-fitting simulation was to consider all experimental data together with a number of drug doses and recovery times, in order to derive a coherent kinetic scenario. Once the input baseline set of kinetic parameters was determined, the data were simulated on the cisplatin-treated IGROV-1 cells using a trial-and-error-procedure to find biologically appropriate estimates of the cisplatin-induced delays, block effects and cell mortality induced at every cell-cycle phase.

The Montalenti *et al.* modeling results yielded a very detailed kinetic description of the IGROV-1 cell cycle dynamics treated with cisplatin [89]. It remains unclear whether their modeling inferences can be easily translatable to human ovarian cancer tumor-drug interactions, an issue that warrants further exploration.

2.5 Modeling Stem Cell Dynamics

To estimate stem cell self-renewal probabilities in serous epithelial ovarian carcinomas, Ciampi *et al.* proposed a method for estimating the probability of self-renewal of serous epithelial ovarian tumor stem cells starting from experimentally derived distributions of clonal colonies obtained in cell culture [90].

The model was based on tumor cell populations being composed of a) tumor stem cells, capable of self-renewal and subsequent tumor self-regeneration; b) transitional cells, not capable of self-renewal but characterized by a limited potential for further proliferation (i.e., de-differentiation); and c) end-stage cells, incapable of further proliferation, and thus considered terminally differentiated.

The proliferation of the cancer cell population was treated as a multi-type Galton-Watson process in which stochastic fluctuations lead to probability distributions in the number of each cell type, under the assumption that cell division does not necessarily occur at the same time for same-age cells.

Using a Nelder-Mead algorithm and equating the theoretical moments of the distribution of cell types with the observed experimental colony size mean and variance, Ciampi *et al.* derived parameter estimates for the probability of self-renewal of a tumor stem cell, and the clonal expansion number expressed in the generations, i.e., the number of de-differentiated states.

We note that a key assumption of this model is that ovarian cell populations are organized in a hierarchy of decreasing proliferation potential and increasing degrees of cellular differentiation. However, it is unclear if stem cells are responsible for the initiation and progression of clinical ovarian cancers [91].

Moreover, the lack of unique markers that are able to identify stem cells in the context of ovarian cancers make it difficult to characterize the proliferative landscape of such cells *in vitro* or *in vivo*.

2.6 Remarks

From a mathematical point of view, the quantitative tools employed in the models described in Sections 2.2 - 2.5 range from probabilistic techniques (e.g., branching processes, bootstrap resampling, time-homogeneous Markov chains), through differential equation-based approaches (e.g., single or multiple compartment ODEs, PDEs or coupled ODE-PDE models).

There are, however, several underlying limiting assumptions with using such modeling approaches. Most such models rely on the “perfect mixing” assumption that cellular populations are spatially homogeneous, and are only able to quantify average cellular behavior, rather than heterogeneous genetic and phenotypic cellular profiles.

In doing so, existing models are only able to generate aggregate statistics or outcomes similar to results derived from population-based cohort studies. The extent to which such modeling results would contribute to understanding patient-specific cancer progression or subsequent therapeutic outcomes is thus unclear, but remains an active area of exploration.

Studying the natural history, growth, progression or dynamic response to treatment of breast and ovarian cancers in an integrated systems biology/mathematical framework represents a complementary tool at the disposal of the women's cancers clinical community. If accurately and realistically applied to existing clinical data, such frameworks could represent a substantial step forward, and can be performed in a relatively inexpensive manner, that relies only on computing power.

Mathematical modeling could thus provide insights about the disease dynamics that reach beyond contemporary clinical and experimental tools and are impossible to obtain even in large-scale cohort studies. Dynamic spatiotemporal mathematical models of women's cancers and their evolution could provide a quantitative understanding of the likelihood of occurrence of specific clinical scenarios in response to detection, treatment and the when and the why of emergence of resistance.

Chapter 3: Modeling the Dynamics of High-Grade Serous Ovarian Cancer Progression for Transvaginal Ultrasound-Based Screening and Early Detection

The results in this chapter were published in [58]. It focuses on a mathematical study of ovarian cancer initiation, progression, and detection *in silico*.

3.1 Introduction to HGSOC Detection Methods

The five-year survival rate for all ovarian cancer stages in the US has improved from $\sim 30\%$ in 1970 to $\sim 46\%$ in 2017. This is a result of risk-reduction prophylactic surgeries for high-genetic risk cases, the improved administration of taxane and platinum chemotherapies, and the extended life expectancy of the affected patients [92].

Despite this recent progress, ovarian cancer still remains the most fatal gynecologic cancer [4]. By the end of 2017, it is estimated that 22,440 new cases of ovarian cancer and 14,080 deaths related to this disease will occur [4].

The inability to detect aggressive, early stage ovarian cancer has substantial implications for the reported low post-diagnosis survival rates. This is possibly, in part, due to the natural history of ovarian cancers, since most women with localized disease present vague symptoms such as pelvic or abdominal pain, abdominal bloating, urinary urgency or frequency, and early satiety [7].

A recently proposed morphomolecular characterization of ovarian cancers underscores the importance of clear separation between the various subtypes of ovarian cancers with respect to the appropriate future therapeutic targeting [93]; therein, it is reported that epithelial ovarian cancers account for 85 - 90% of ovarian cancers, with a subset of epithelial ovarian cancers, HGSOCs representing nearly 70% of all ovarian cancer cases.

Existing early detection screening strategies for other cancer types, including prostate, colon, breast and cervical cancers, raise the question of whether HGSOC is amenable to similar screening strategies. Emerging insights into HGSOC's disease progression suggest that early detection of low volume advanced stage, rather than large volume early stage HGSOC, may be a more clinically actionable goal of screening studies. This is because five-year relative survival rates for advanced stage cancers at diagnosis are significantly lower than for early stage cancers at diagnosis [7, 23, 73, 76, 94].

3.1.1 Ultrasound and CA125 Blood Levels Testing

Transvaginal-ultrasound (TVU) represents an integral part of all reported major ovarian cancer screening trials, despite its well-recognized limitations (e.g., bilateral disease, or multiple foci spread throughout the peritoneal cavity). TVU is accurate in detecting abnormalities in ovarian volume and morphology, but is less reliable in differentiating benign from malignant tumors. Serum biomarkers (CA125, HE4) testing, pelvic examinations, or simultaneous TVU and CA125 testing have also been examined as non-invasive tools for detecting early stage ovarian cancer in general-risk women.

However, mounting evidence suggests that annual screening with TVU and serum biomarkers does not reduce mortality [5,30]. Furthermore, high false positive rates leading to intervention are associated with potential harm, such as unnecessary surgical intervention and related complications.

The lack of utility of such screening tools is possibly due to the absence of adequate TVU sensitivity in detecting small increases in tumor volume and distinguishing between malignant and benign cases. The addition of serum biomarkers testing (e.g., CA125 levels) does not improve early-stage detection levels, either [19,40,95,96].

The largest ever ovarian cancer screening study of 202,638 general-risk women demonstrated that multimodal screening including serial TVU and CA125 level testing yielded a 15% mortality reduction rate compared with a 0% no screening or 11% unimodal TVU-based screening cohort mortality reduction rate over 0-14 follow-up years [19].

However, this study also showed increased CA125 levels can be detected in benign conditions, rendering it inadequate for use in screening asymptomatic women for early-stage ovarian cancer. The lack of adequate early-detection tools might be explained by the fact that any epithelial ovarian cancers diagnosed in stage I might be fundamentally different from those diagnosed in advanced stages, which are preponderantly high and not low-grade cases [94].

As a result, whether HGSOC constitutes a valid target for ovarian cancer screening remains unanswered and highly contentious with respect to either general-risk or high genetic-risk women, such as germline *BRCA1* and *BRCA2* mutation carriers, or women with a significant family history of breast or ovarian cancer. A quantitative invalidation of TVU as an effective HGSOC screening strategy is a necessary next step.

3.1.2 Model Findings

Herein, we propose a mathematical model for a quantitative explanation on the reported failure of TVU-based screening to improve HGSOC low-volume detectability and overall survival.

We develop a novel *in silico* mathematical assessment of the efficacy of a unimodal TVU monitoring regimen as a strategy aimed at detecting low-volume HGSOC in cancer-positive cases, defined as cases for which the inception of the first malignant cell has already occurred. Our findings show that the median window of opportunity interval length for TVU monitoring and HGSOC detection is approximately 1.76 years. This does not translate into reduced mortality levels or improved detection accuracy in an *in silico* cohort across multiple TVU monitoring frequencies or detection sensitivities.

We demonstrate that even a semiannual, unimodal TVU monitoring protocol is expected to miss detectable HGSOC. Lastly, we find that $\sim 50\%$ of the simulated HGSOC growth curves never reach the baseline detectability threshold, and that on average, 5 - 7 infrequent, rate-limiting stochastic changes in the growth parameters are associated with reaching HGSOC detectability and mortality thresholds respectively.

Our mathematical model captures the dynamic, temporal evolution of HGSOC progression. It is consistent with recent case reports and prospective TVU screening population studies, and provides support to the empirical recommendation against frequent HGSOC screening.

3.2 Modeling Approach and Assumptions

We develop an *in silico* mathematical framework modeling incipient HGSOC growth kinetics in an untreated scenario, subject to stochastic heterogeneous fluctuations. Herein, we refer to an untreated HGSOC as a radiographically detected, clinically asymptomatic, treatment-free malignancy in which no surgery and/or other systemic therapies has yet been performed/administered.

Inspired by a stochastic numerical model of breast cancer growth [97], we follow a similar approach to model HGSOC natural history and progression until clinical TVU detectability. The key feature of this model incorporated in the present work involves modeling HGSOC progression as Gompertzian growth kinetics further characterized by infrequent, rate-limiting stochastic changes in the growth parameters.

3.2.1 HGSOC Growth Estimation

To estimate a lower bound for the initial HGSOC growth rates, we identified the existing TVU-based screening study with the largest cohort of ovarian cancer patients [98]. In this study, data concerning ovarian volumes were obtained from 13,963 patients who were undergoing annual TVU examinations from 1 to 11 years.

We define abnormal ovarian enlargement as two standard deviations above normal ovarian volume in pre- and postmenopausal women, see [29, 98, 99]. Based on 58,673 ovarian volume observations, the upper limit for normal ovarian volume therein was found to be 20 cm^3 for pre- and 10 cm^3 for postmenopausal women [98]. Menopause is defined as occurring 12 months after a womans last menstrual cycle and confirmed by follicle stimulating hormone levels > 40 IU/L [100].

We subsequently assume that any HGSOC tumor volume larger than the difference between the two pre-defined thresholds would represent a suspicious TVU finding, and subsequently be diagnosed as a radiographically detectable HGSOC case.

The data points illustrated in Figure 3.1 represent estimated lower bounds for the initial HGSOC rates used to initialize our model. They correspond to 9 reported HGSOC clinical findings based on TVU examinations of adnexal ovarian regions available 12 months or fewer prior to the preoperative diagnosis time of the malignancy [101]. The reported cases showed no apparent ovarian volume abnormalities 2 to 12 months prior to TVU diagnosis.

We note that, to the best of our knowledge, these findings represent the only available temporal data on the progression of previously occult, radiographically detected HGSOCs.

HGSOC-growth curve time is measured from the inception of the first malignant cell until the time needed to reach the baseline TVU detection threshold, or until the baseline life-threatening tumor volume is reached. Herein, we assume that the minimum, baseline TVU detectability threshold for a cancer-positive case is 10 cm^3 (equivalent to 10^{10} cells, or to a 2.673 cm spherical HGSOC tumor diameter).

Similarly, we follow the definition of the life-threatening untreated HGSOC tumor volume to be 10^3 cm^3 (equivalent to 10^{12} cells, or to a 12.407 cm spherical tumor diameter), as previously published [102]. The two thresholds can be adjusted if more sensitive diagnostic techniques are developed, or if different life-threatening untreated HGSOC tumor volume values are used.

We assume the cell number-to-volume conversion to be 1 $cm^3 = 10^9$ HGSOC cells. The baseline thresholds were chosen to estimate conservative lower bounds for the time of TVU diagnosis and time of reaching the life-threatening tumor volume distributions. Herein, we define the window of opportunity interval as the difference between the two thresholds based on the growth curves that reach both endpoints.

3.2.2 Modeling Equations

We use the incipient HGSOC growth kinetics model to study the timing of HGSOC initiation relative to reaching TVU detectability and the life-threatening untreated tumor volume sizes, as defined above, and its subsequent implications on

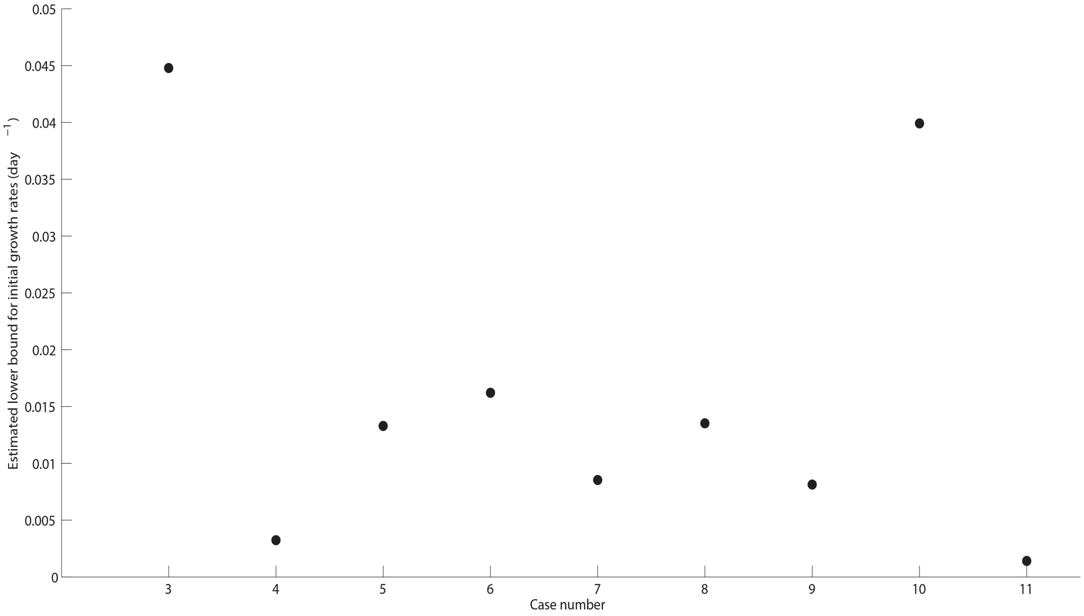

Figure 3.1: Reported bi-dimensional measurements of 9 incidental, previously undetected HGSOC tumor sizes (length, width) were converted into a weighted, one dimensional measurement (i.e., spherical radius): weighted radius $r = \sqrt{a \cdot b}$, where a and b are the radii of the minor and major axes of an ellipsoid, respectively. To compute initial tumor volumes, we assume tumors to be spherical and compute their volume according to the formula $\frac{4\pi}{3} r^3 \mathrm{cm}^3$. We assume normal ovarian volumes were 20 cm^3 for the pre- and 10 cm^3 for the postmenopausal women reported in Table 1 of [98]. We estimate the lower bounds for the initial HGSOC growth rates as follows: initial growth rate $= \frac{\ln(\text{tumor volume at diagnosis}) - \ln(\text{normal ovarian volume})}{T}$, where T represents the number of days between the timing of the previous, non-suspicious TVU examination and the malignancy diagnosis. Each point plotted (case number, estimated initial growth rate) corresponds to case number (3 11) reported in Table 1 of [101].

Term	**Definition**
Occult growth curve	*in silico* HGSOC growth curve that never reaches TVU detectability.
Succumbed growth curve	*in silico* HGSOC growth curve that reaches both a TVU-detectable and life-threatening tumor volume in between consecutive TVU monitoring events.
Cancer-positive growth curve	*in silico* HGSOC growth curve in which the inception of the first malignant cell has already occured.
Untreated growth curve	*in silico* HGSOC growth curve described as radiographically detected, treatment-free malignancy in which no surgery/therapy has yet been performed/administered.

Table 3.1: Definitions used throughout the model

TVU monitoring protocols.

We choose to use the terminology "TVU monitoring" in lieu of "TVU screening", as the latter would be a more appropriate term for a detection strategy focused on a cohort of cancer-negative, general- or high-risk otherwise asymptomatic healthy women [99], as opposed to a pre-selected, biased *in silico* cancer-positive cohort, for which the former term is more appropriate.

A main study end point for this model was HGSOC-specific mortality, specifically the number of *in silico* HGSOC growth curves that would be missed even under frequent TVU monitoring.

To this end, we developed a mathematical framework modeling incipient untreated HGSOC volume growth in order to satisfy two purposes: one, to simulate the natural history of the malignancy, and two, to quantify the relationship between TVU monitoring frequency and detection time of a non-life-threatening HGSOC volume.

To obtain a temporal estimate of the effective growth behavior of a simulated HGSOC growth curve, we let $N(t)$ be the total HGSOC tumor volume, i.e., the number of HGSOC cells located in the primary tumor site (e.g., one of the ovaries, or the Fallopian tubes) at time t. N_0 represents the initial, pre-diagnosis HGSOC cell count, set as 1 for computational convenience. Time t is measured since the inception of the first malignant cell.

If we let $\mathrm{k}_{\mathrm{growth}}$ represent the initial HGSOC growth rate constant and $\mathrm{k}_{\mathrm{decay}}$ describe the growth saturation rate, where both parameters have the dimension of inverse time (e.g., in our case, day^{-1}), the Gompertz function modeling tumor growth can be expressed as:

$$N(t) = N_0 \mathrm{e}^{\frac{\mathrm{k}_{\mathrm{growth}}}{\mathrm{k}_{\mathrm{decay}}}(1-\mathrm{e}^{-\mathrm{k}_{\mathrm{decay}} t})}, \tag{3.1}$$

$$N(0) = 1. \tag{3.2}$$

The normalized $N(t)$ thus satisfies the following differential equation:

$$\frac{dN}{dt} = N(t)[\mathrm{k}_{\mathrm{growth}} - \mathrm{k}_{\mathrm{decay}} \ln N(t)]. \tag{3.3}$$

The carrying capacity $N(\infty)$ is assumed to be finite and nonzero. It follows that $\mathrm{k}_{\mathrm{decay}} > 0$, and that $N(\infty) = \mathrm{e}^{\frac{\mathrm{k}_{\mathrm{growth}}}{\mathrm{k}_{\mathrm{decay}}}} > 1$. To find the inflection point of $N(t)$, that is $N_i(t_i)$, we require

$$\frac{d^2N}{dt^2} = [\mathrm{k_{growth}} - \mathrm{k_{decay}} \ln N(t) - \mathrm{k_{decay}}]\frac{dN}{dt} = 0, \tag{3.4}$$

i.e., the derivative of the change in HGSOC growth rate is set as 0.

Since $N(t) > 0$ for finite t, then

$$\ln N_i = \frac{\mathrm{k_{growth}}}{\mathrm{k_{decay}}} - 1, t_i = \frac{1}{\mathrm{k_{decay}}} \ln \frac{\mathrm{k_{growth}}}{\mathrm{k_{decay}}}. \tag{3.5}$$

It thus follow that $N_i = \mathrm{e}^{\frac{\mathrm{k_{growth}}}{\mathrm{k_{decay}}} - 1}, N_\infty = eN_i$. In this case, the tumor cell burden can outgrow its size at the inflection point by a factor of e. The inflection point represents a turning point in the dynamics when the observed growth trend starts decelerating.

Nonetheless, while the Gompertz equation describes a density-dependent growth rate, it does not account for any stochastic irregularities, e.g., stepwise growth patterns, also see [97]; such temporary Gompertzian plateaus (i.e., cessation in tumor growth) may be correlated, as reported *in vitro*, with tumor dormancy in ovarian cancer spheroids [103,104], human ovarian cancer cell lines [105,106], or *in vivo* with tumor xenografts implanted in mice [105], and may be associated with dormancy in untreated, undetectable HGSOC.

Thus, a constant growth rate might not be feasible to model progression. To this end, by incorporating rare but relatively large jumps in the growth saturation rate $\mathrm{k_{decay}}$, we assume that HGSOC growth slows down due to adverse environmental conditions (e.g., reactive O_2 presence, nutrient depletion).

The irregular tumor growth kinetics illustrated in our model accounts for the observed heterogeneity in the progression of clinical HGSOCs [107] and highlights

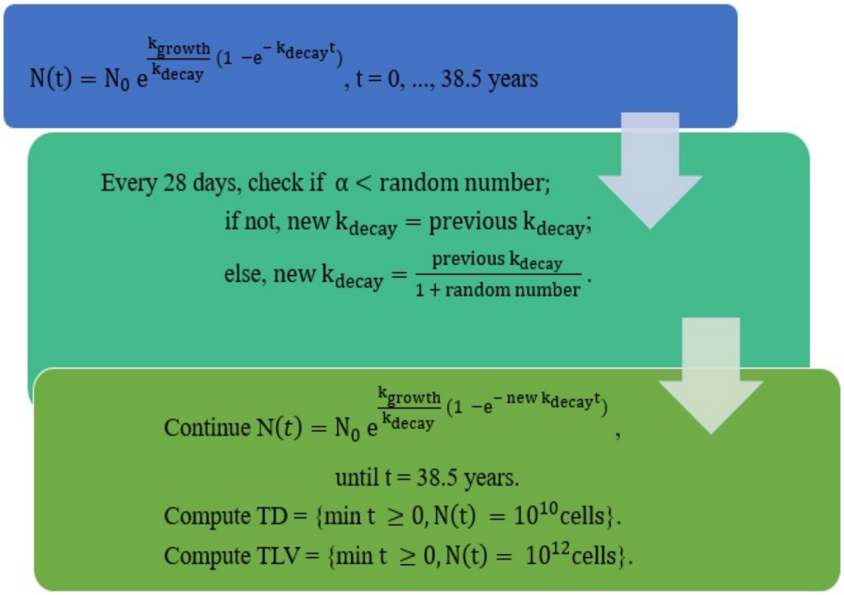

Figure 3.2: The initial HGSOC growth rate and decay values, k_{growth} and k_{decay}, respectively and their ranges are as reported in Table 3.2.

the differential HGSOC natural histories that lead to identical clinical outcomes or presentations (e.g., see case numbers (4) and (11) reported in Table 1 of [101]). The tumor growth kinetics represented herein could thus be phenomenologically valid both *in vivo* and *in vitro*.

3.2.3 Modeling Assumptions

The definitions used throughout the implementation of the HGSOC carcinogenesis, growth and progression model are provided in Tables 3.1. A flowchart of the computational model is shown in Figure 3.2.

We assume the inception of the first HGSOC malignant cell occurs sometimes during premenopausal years, and thus we increment time in intervals of 28 days

Parameter	**Value**	**Unit**	**Simulated Range**
$\mathrm{k_{growth}}$	Median $= 0.0133$	day^{-1}	$0.0014 - 0.0448$
$\mathrm{k_{decay}}$	$\frac{\mathrm{k_{growth}}}{2}$	day^{-1}	-
N_0	1	cell	-
α	Median $= 0.015$	-	$0.0094 - 0.015$

Table 3.2: Herein, $\mathrm{k_{growth}}$ represents the initial HGSOC growth rate, $\mathrm{k_{decay}}$ denotes the initial HGSOC growth saturation rate, and N_0 represents the initial, pre-diagnosis HGSOC cell count. The convention for the cell number-to-volume conversion used is $1\ \mathrm{cm}^3 = 10^9$ cells. Moreover, α denotes the probability of random change in $\mathrm{k_{decay}}$. Its value is subsequently updated according to the algorithm illustrated in Figure 3.2.

(the average length of a menstrual cycle [108]) for a total number of 460 menstrual cycles, the average cumulative length of a lifetime menstrual cycle. We set the initial $\mathrm{k_{decay}} = \frac{\mathrm{k_{growth}}}{2}$. Varying this initial parameter would not yield substantially different median or range values for the estimated cdf's.

We then implement the changes in the initial growth saturation rate, $\mathrm{k_{decay}}$, in a two-step manner. First, we generate a number $\alpha \sim \ln N(10^{-2}, 25 \cdot 10^{-2})$, that is log-normally distributed with mean $= 10^{-2}$, variance $= 25 \cdot 10^{-2}$, and range $=$ 0.0094 - 0.150 (0.01 mean probability of change in each 28-day period, or 26% mean probability of change in 2 years). Herein, α refers to the probability of random change in $\mathrm{k_{decay}}$.

In order to implement conservative estimates for the clinically occult random variable α, we choose an asymmetric, right-skewed probability distribution function. Second, we check whether α is less than a randomly generated number between 0

Volume (cm^3)	**Cell-number count (cells)**	**Equivalent spherical tumor diameter**
0.5	$0.5 \cdot 10^9$	0.98
1	10^9	1.24
1.5	$1.5 \cdot 10^9$	1.42
10	10^{10}	2.67
20	$2 \cdot 10^{10}$	3.36
1000	10^{12}	12.4

Table 3.3: Cell-number-to-volume and tumor diameter conversions used throughout the model.

and 1. If that is the case, we then generate a second random number between 0 and 1 and compute the updated $\mathrm{k_{decay}}$ as $\mathrm{k_{decay}} = \frac{\text{previous } \mathrm{k_{decay}}}{1+\text{random number}}$. We then allow the number of HGSOC cells, $N(t)$, to follow the Gompertzian growth law until the probability of a random change in $\mathrm{k_{decay}}$ occurs again, which leads to another update.

Given a fixed carrying capacity, varying either $\mathrm{k_{growth}}$ or $\mathrm{k_{decay}}$ makes little qualitative difference from a mathematical perspective; we can thus infer that modifying either parameter yields similar qualitative effects.

From a molecular perspective, we chose to focus on changes in the initial HGSOC growth saturation rate, $\mathrm{k_{decay}}$, as these infrequent, rate-limiting changes could be associated in part with the several (epi)genetic alterations in tumor suppressor genes and/or changes in genes involved in DNA damage repair pathways.

Reducing the growth saturation rate, $\mathrm{k_{decay}}$, of the HGSOC tumor cell burden the program increases the current HGSOC carrying capacity, $N(t)$ in a stochastic fashion. Changes are globally implemented, meaning that once a stochastic jump in $\mathrm{k}_{\mathrm{decay}}$ occurs, cells proliferate according to the newly updated Gompertz-type growth law.

3.3 Numerical Results

3.3.1 Model Simulation Of HGSOC *In Silico* Growth Curves

Five representative growth curves generated by the HGSOC model in our simulated cancer-positive cohort are illustrated in Figure 3.3.1. The baseline parameter set and cell-number-to-volume and tumor diameters conversions as reported in Tables 3.2 and 3.2.3 are used.

By incorporating rare but relatively large jumps in the growth saturation rate $\mathrm{k}_{\mathrm{decay}}$, we illustrate how a HGSOC volume grows in stepwise patterns and may not increase for relatively large amount of time (see Figure 3.3.1), as opposed to exhibiting a constant doubling time. This approach also enables us to generate a distribution of heterogeneous pre-clinical HGSOC natural histories in an *in silico* cancer-positive cohort.

Statistics generated from one representative simulation of the HGSOC growth and progression model using n = 1000 HGSOC growth curves are reported in Table 3.3.1. Therein, the generated data illustrate the time needed to reach the baseline TVU-detectable HGSOC volume of 10 cm^3, the baseline life-threatening tumor volume of 10^3 cm^3, and the window of opportunity interval length. The number of

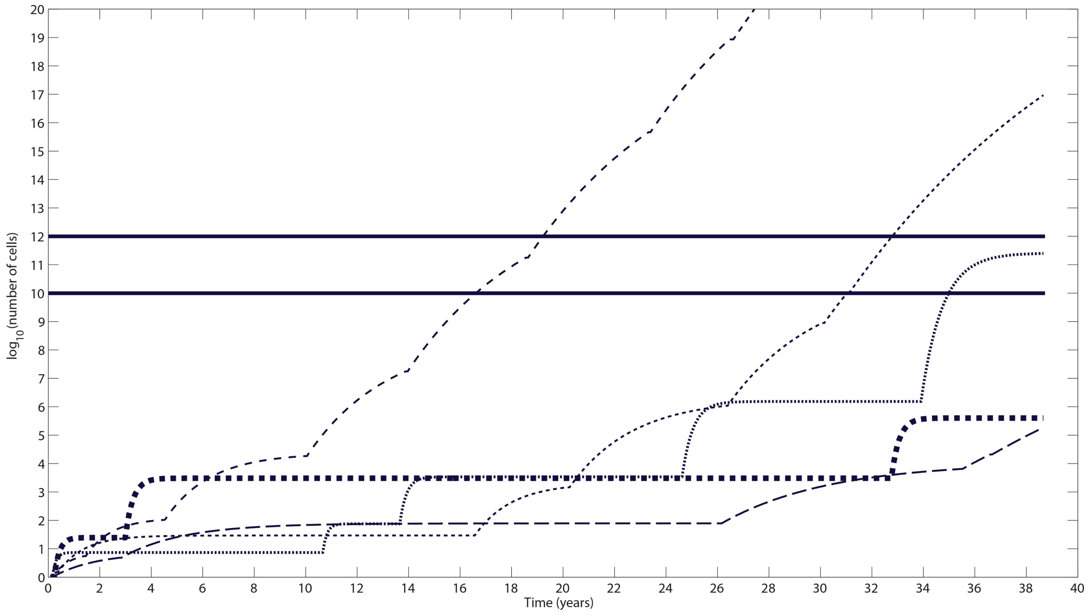

Figure 3.3: This sample simulation of the HGSOC progression model illustrating five representative growth and progression curves is generated using the same baseline parameter set outlined in Tables 3.2 and 3.2.3. Each of the representative growth curves is an independent realization of the HGSOC stochastic growth and progression model, initialized with the same parameter value set. Values the baseline TVU detectability and life-threatening untreated tumor threshold are as reported previously. In this representative simulation, two curves reach the detection threshold (lower solid line) in 16.4 and 31.2 years, respectively, and life-threatening tumor volume threshold (upper solid line) in 19.3 and 32.6 years, respectively. The calculated window of opportunity interval length is thus 2.9 and 1.4 years, respectively. One curve reaches only the detection threshold, in 35.0 years, and two curves remain below both thresholds. Time is measured since the inception of the first HGSOC cell. The curves are sorted from left to right. Note that the probability that a random change in k_{decay} occurs is independent of whether current carrying capacity is reached or not.

HGSOC growth curves that never reach the TVU baseline detectability threshold (occult), or the life-threatening threshold (succumbed) are also reported therein. Subsequent results reported below are based on the same computation that yielded the data generated in Table 3.3.1.

Baseline parameters used to simulate $n = 1000$ HGSOC growth curves are as specified in Table 3.2. Here, the following definitions are used: TD $=$ min $[t \geq 0$ such that $N(t) = 10^{10}$ cells], TLV $=$ min $[t \geq 0$ such that $N(t) = 10^{12}$ cells], WOP $=$ TLV - TD, occult represents the number of HGSOC growth curves that never reach the detectability threshold (i.e., TD $=$ 0), and regressed represents the number of HGSOC growth curves that never reach the life-threatening size threshold (i.e., TLV $=$ 0). Cell-number-to-volume and tumor diameter conversions are reported in Table 3.2.3.

The number of HGSOC growth curves that never become detectable (n $=$ 509), and life-threatening, respectively (n $=$ 582) are subtracted from n $=$ 1000 simulated HGSOC growth curves in the monitoring frequency analysis. Notice that it takes approximately 26 years for a representative HGSOC growth curve to become detectable, and about 27 years for an untreated HGSOC growth curve to become life-threatening. The expected window of opportunity interval length for curves that reach both thresholds is expected to be concentrated around 1.8 years.

Statistic	**TD (years)**	**TLV (years)**	**WOP (years)**
Median	25.85	27.3	1.76
Mean	25.7	26.73	2.6
STD	7.94	7.4	2.85
Min.	4.14	4.75	0.3
Max.	38.43	38.6	2.35

Table 3.4: Statistics generated from one sample simulation of the HGSOC growth and progression model illustrating the time needed to reach the baseline TVU detection threshold (TD), the baseline life-threatening tumor volume (TLV), the duration of the window of opportunity interval (WOP = TLV - TD), and the number of HGSOC growth curves that never reach TVU baseline detectability (occult), or the life-threatening threshold (regressed) volumes, respectively, during the sample simulation.

3.3.2 Number of HGSOC Carcinogenetic Events Leading to HGSOC Growth and Progression

Computational results indicate that for the 491 sample HGSOC growth curves that reach the baseline TVU detection threshold, the number of infrequent, rate-limiting events associated with changes in the initial growth saturation rate, k_{decay} is around 7 (median = 7, mode = 6, range = 3 10, see Figure 3.4). Interestingly, for this representative simulation, the mode number of required events was 5, and the reported maximum of such events was 10.

Note also the substantial heterogeneity in the number of events required to lead to a TVU-detectable HGSOC tumor volume. Similarly, for the 418 growth curves that reach the baseline life-threatening tumor volume threshold, the number of rate-limiting events associated with changes in the initial growth saturation rate, k_{decay}, is around 7 (median = mode = 7, range = 4 - 10, see Figure 3.4), and the reported maximum of such events was 10.

Note again the substantial heterogeneity in the number of events required to lead to a life-threatening, untreated HGSOC tumor volume since the inception of the first malignant cell. One or two extra events are required in order for a detectable HGSOC tumor volume to become life-threatening.

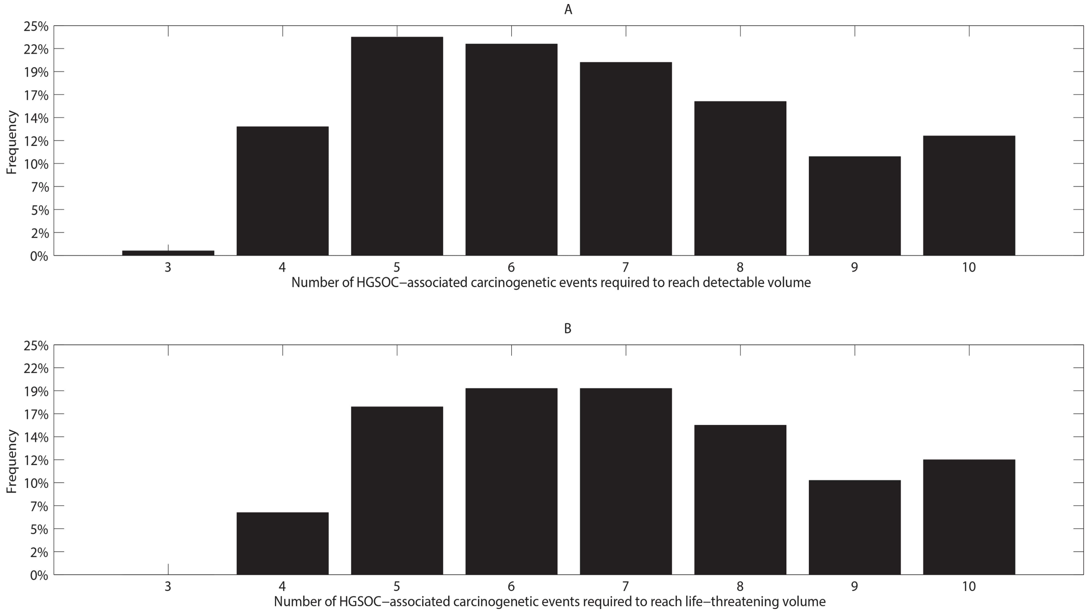

Figure 3.4: In one representative simulation of the model generating 1000 cancer-positive initially clinically occult HGSOC growth curves, (A) 491 sample HGSOC growth curves progress to reach the detectability threshold and (B) 418 reach the life-threatening volume threshold. (A) We record the frequency of rate-limiting events associated with changes in the initial growth saturation rate, k_{decay} out of the n = 491 growth curves. For this representative simulation, the mode and median number of such events are 5, and 7 respectively. (B) We record the number of rate-limiting events associated with changes in the initial growth saturation rate, k_{decay}, out of n = 418 growth curves. For this representative simulation, the mode and median of the number of such events are 7, and 7 respectively. A maximum number of 10 events associated with changes in the initial growth saturation rate, k_{decay}, is recorded in both panels.

3.3.3 Estimating the Window of Opportunity Interval Length

To produce estimates of the duration of HGSOC's pre- and post-diagnosis phases, we report the generated value ranges (median, range), with median values of the times needed to reach baseline TVU detection threshold, baseline life-threatening tumor volume, and the window of opportunity interval length; we chose to report median values as the median was a more robust statistic compared to the mean throughout all sample model simulations, and thus constitutes a more accurate descriptor of the aggregate cancer-positive HGSOC population dynamics.

The model-generated empirical cumulative distribution functions (cdf's) for reaching the baseline detection threshold, the baseline life-threatening tumor volume, and the window of opportunity length interval are reported in Figure 3.5. For this representative simulation, a total of 498 growth curves reach the baseline TVU detection threshold (median = 26.7 years, range = 4.52 38.5), a total of 418 growth curves reach the baseline life-threatening tumor volume threshold (median = 27.65 years, range = 7.28 38.6), and a total of 418 growth curves reach both thresholds, and are thus included in the window of opportunity interval length computation and cdf estimation (median = 1.76 years, range = 0.3 14, see Figure 3.5, panel C). As an alternative to panel C, we illustrate in panel D the fraction of radiographically detected, treatment-free HGSOC growth curves that progress to the life-threatening volume threshold is illustrated. Increasing the number of simulated HGSOC growth curves (n $>$ 1000) does not yield substantially different median or range values for the estimated cdf's.

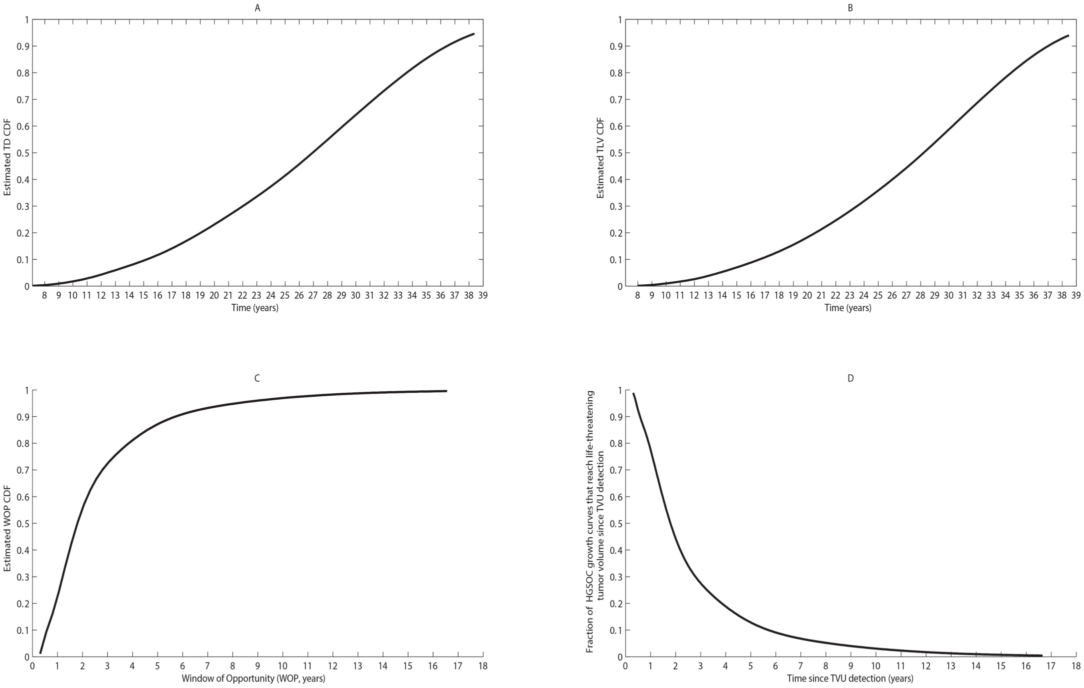

Figure 3.5: Empirical cumulative distribution functions for (A) time until baseline TVU detection threshold is reached (TD); (B) time until life-threatening tumor volume is reached (TLV); (C) the window of opportunity interval length; (D) the fraction of radiographically detected, treatment-free HGSOC cases that progressively reach the life-threatening threshold starting from the baseline detection threshold time. The progression of n = 1000 HGSOC growth curves is simulated in order to determine typical empirical cumulative distribution functions for (A) time until baseline TVU detection threshold is reached (median = 26.7 years, range = 4.52 - 38.5); in this sample simulation, a total of 498 growth curves reach this threshold; (B) time until life-threatening tumor volume is reached (median = 27.65 years, range = 7.28 - 38.6). In this sample simulation, a total of 418 growth curves reach this threshold; (C) window of opportunity interval length (median = 1.76 years, range = 0.3 - 14).

3.3.4 Assessing the Feasibility of Multiple Frequency TVU Monitoring Protocols

Figure 3.6 illustrates the relative proportions of HGSOC curves that remain occult (first, black horizontal column), that are detectable in the first or subsequent TVU monitoring events (second, grey horizontal column), and lastly, that are succumbed (third, white horizontal column) out of n = 1000 simulated HGSOC growth curves. Semiannual monitoring HGSOC progression via TVU performs the best (0.9% of total HGSOC curves succumb [see Table 3.1 for definitions]) despite the frequent TVU monitoring, compared to a 4.2% succumb rate when monitored annually, or 10.7% when monitored biannually.

It is also worth noting the relatively large proportion of HGSOC curves that remain occult (50.9% of the total n = 1000 growth curves in this representative simulation, see Figure 3.6). This representative simulation was performed using the baseline parameters outlined in Tables 3.2 and 3.2.3.

3.3.5 TVU Sensitivity Analysis

We conducted a sensitivity analysis with respect to the TVU detection thresholds, set at 0.5, 1 or 1.5 cm^3, to determine whether the percentages reported above would drastically vary. We demonstrate that the percentage of HGSOC growth curves that reach the updated baseline detection and life-threatening tumor volume thresholds in between the same monitoring events increases with less frequent TVU

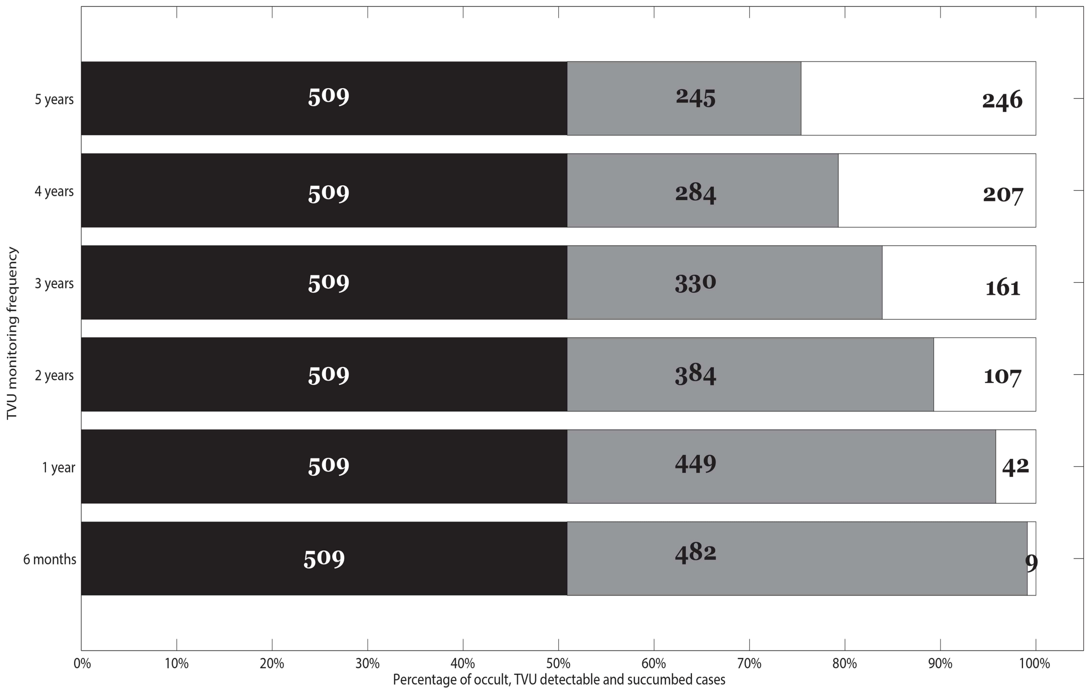

Figure 3.6: We report the relative proportions of HGSOC curves that remain occult (first, black horizontal column), that are detectable in the first or subsequent TVU monitoring events (second, grey horizontal column), and lastly, that are succumbed (third, white horizontal column) out of n = 1000 initial HGSOC growth curves. The proportions reported vary for different TVU monitoring frequencies, i.e., every 5, 4, 3, 2 years, every 1 year (annually) or every 6 months (semiannually). Importantly, the last horizontal column represents the percentage of HGSOC growth curves that would be missed even under frequent TVU monitoring.

Monitoring Frequency	**10** cm^3	**1.5** cm^3	**1** cm^3	**0.5** cm^3
6 months	9	0	0	0
1 year	26	13	3	0
2 years	61	34	23	12
3 years	70	29	37	25
4 years	78	33	46	50
5 years	79	36	60	71

Table 3.5: Each table entry represents the difference between consecutive screening frequencies (e.g., 79, the leftmost entry, bottom row, represents the number of additional HGSOC growth curves that would be missed when switching from a 4-year monitoring frequency to a 5-year monitoring frequency) or consecutive TVU detectability sensitivities (e.g., 36, the second leftmost entry, bottom row, represents the number of additional HGSOC growth curves that would be missed when switching from a 1 cm^3 TVU detection threshold to a 1.5 cm^3 TVU detection threshold).

monitoring events (Figure 3.3.5, panel A), and decreases with more sensitive TVU detection thresholds (Figure 3.3.5, panel B).

Our findings confirm that more sensitive TVU detection thresholds and more frequent TVU monitoring improve diagnostic accuracy (decreasing the number of succumbed HGSOC growth curves). These plots were generated from one representative simulation using a total number of n = 1000 simulated growth curves and performed using the same baseline parameter set and cell-number-to-volume and tumor diameters conversions as reported in Tables 3.2 and 3.2.3. The data used to produce Figure 3.3.5 is given in Table 3.5.

3.4 Discussion of Modeling Results

HGSOC constitutes an attractive target for early detection strategies if detected before reaching large volume advanced stage, when overall survival rates are grim [109]. The validation of any HGSOC tumor volume clinical detection strategy is thus whether frequent screening is capable of lowering mortality rates. However, numerous transvaginal ultrasound (TVU) detection-based population studies aimed at detecting low-volume ovarian cancer have not yielded reduced mortality rates and thus challenge the effectiveness of TVU as a HGSOC monitoring strategy aimed at improving overall survival rates [5, 19, 23, 28, 96, 98, 101, 110–112].

A quantitative invalidation of TVU as an effective HGSOC screening strategy is a necessary next step. Our mathematical modeling approach proposes a quantitative explanation for the reported failure of TVU to improve HGSOC low-volume

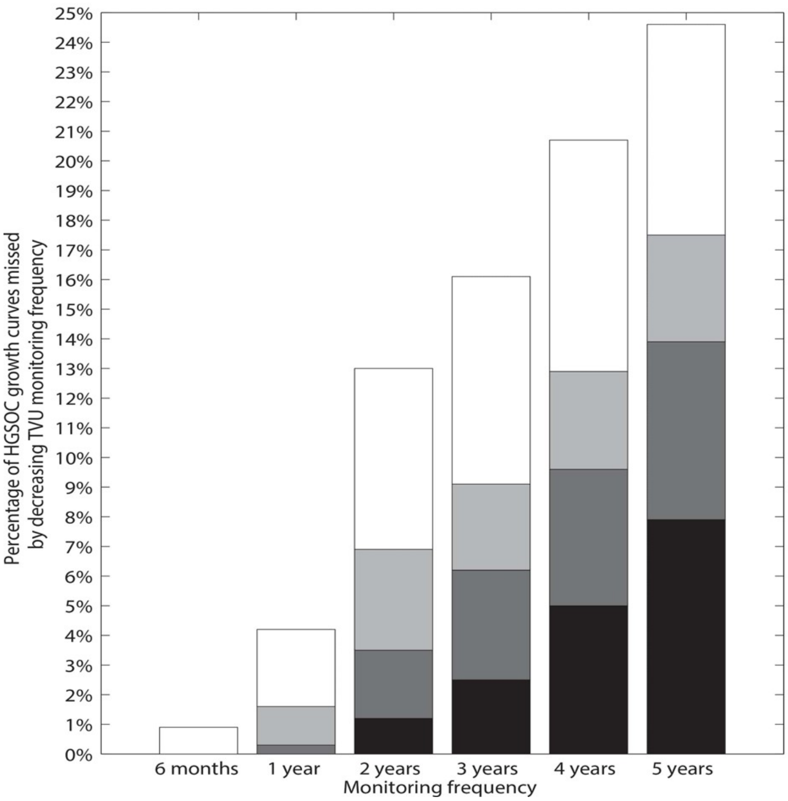

Figure 3.7: (A) Fewer HGSOC growth curves reach the succumbed status with more frequent TVU monitoring events (x-axis) and more sensitive TVU detection thresholds (0.5 cm^3, black vertical columns; 1 cm^3, dark grey vertical columns; 1.5 cm^3, light grey vertical columns; 10 cm^3, white vertical columns). In this panel, vertical columns indicate the percentage of additional HGSOC growth curves that are missed by decreasing TVU detection thresholds relative to the baseline TVU detection threshold set at 10 cm^3, out of a total of 1000 simulated HGSOC growth curves. (B) Fewer HGSOC growth curves reach the succumbed status with more sensitive TVU detection thresholds (x-axis) and more frequent TVU monitoring events ranging from six months to five years. In this panel, vertical columns indicate the percentage of additional HGSOC growth curves that are missed by decreasing the frequency of TVU monitoring events relative to a baseline 6-month frequency, out of a total of 1000 simulated HGSOC growth curves.

detectability and overall survival.

We develop a novel *in silico* mathematical assessment of the efficacy of a unimodal TVU monitoring regimen as a strategy aimed at detecting low-volume HGSOCs in cancer-positive cases; our model captures the dynamic, temporal evolution of HGSOC progression, and is characterized by several rare rate-limiting events, which can be associated in part with (epi)genetic alterations in tumor suppressor genes and DNA damage repair pathways.

We chose to focus on an unimodal, ultrasound-based HGSOC detection method (i.e., TVU), rather than on blood biomarker levels (i.e., CA125 or HE4 levels), pelvic examinations or simultaneous TVU and CA125 detection. Despite its well-recognized detection limitations in detecting localized or distant metastatic burden, TVU examinations are routinely performed when assessing ovarian volume, while the latter are either not recommended as low HGSOC volume detection unimodal prognostic markers [5,26], or have not been shown to confer a mortality benefit [5,30].

Our results suggest that multiple frequency TVU monitoring across various detection sensitivities does not significantly improve detection accuracy of HGSOCs in an *in silico* cancer-positive population. Specifically, despite the fact that semi-annual monitoring HGSOC progression via TVU performs, as expected, the best compared with annual or biannual monitoring (0.9% succumbed cases versus 4.2% and 10.7%, respectively), a nonzero percentage of succumbed cases is reported in all subsequent simulations of the HGSOC growth and progression model.

Given that our TVU monitoring algorithm is assumed to have 100% specificity and 100% positive predictive value, the actual percentage of such succumbed

HGSOC cases might be substantially higher. This invalidates the use of TVU as an effective HGSOC screening strategy aimed at lowering mortality rates in general-risk or high genetic-risk women. Our mathematical model thus represents a novel attempt to explain why multiple, large-scale TVU-based HGSOC detection screening studies have not proven significant mortality benefits, and focuses on a malignancy that has received very little attention by the mathematical oncology community.

We find that the median time until baseline TVU detection from the inception of the first HGSOC cell is 26.7 years. Given that an average patient's age at diagnosis of ovarian cancer is $55 - 65$ years [4], our findings suggest that the first HGSOC cell may appear on average around 28 - 38 years of age, during a patient's premenopausal period. This may be due to a number of factors, including reproductive history, oral contraceptive use and family history of breast or ovarian cancer [113, 114].

Furthermore, simulation results suggest that once a HGSOC tumor volume becomes clinically detectable, it takes an additional median number of 1.7 years to reach the baseline life-threatening tumor volume threshold; this implies that for a radiographically detected, treatment-free malignancy in which no surgery and/or systemic therapies have yet been performed/administered, the patient would succumb to the disease relatively quickly after initial diagnosis.

Since 90% of the diagnosed HGSOC patients do not have abnormal clinical findings based on TVU performed 12 months or more prior to HGSOC diagnosis [101], the reported median window of opportunity interval length (1.76 years) reflects a bias towards the more aggressive and fast-growing HGSOCs. This is a key prediction of our model, provided by computer simulations in the absence of clinical/experimental estimates of the period of time needed to reach the life-threatening tumor volume threshold or window of opportunity interval length.

This does not, however, translate into reduced mortality levels in an *in silico* cohort across multiple TVU monitoring frequencies or detection sensitivities. Our findings suggest that even a semiannual, unimodal TVU monitoring protocol is expected to miss detectable HGSOCs. We also find that circa 50% of the simulated HGSOC growth curves never reach the baseline detectability threshold, and that on average, 57 rate-limiting events are associated with reaching HGSOC detectability and life-threatening untreated HGSOC volumes respectively.

The predictions obtained with our HGSOC model are consistent with other published cancer progression chronologies reported for colorectal [115] or pancreatic cancers [116, 117]. Yachida *et al.* [117] analyzed genomic sequencing data of metastatic tumors from 7 patients with metastatic pancreatic cancer and calculated that the first parental (non-metastatic) founder cancer cell may require 6.8 years to generate sub-clones with metastatic potential . These sub-clones could give rise to distant metastases within 2.7 years, with clinical diagnosis occurring 1820 years after the genesis of the founder cell.

Jones *et al.* [115] also reported that a benign colorectal tumor might require 17 years to develop into an advanced carcinoma . On a larger timescale, Meza *et al.* [116] reported that the average time from an initial premalignant mutation to the ultimate conversion of a detectable cancer in pancreatic and colorectal cancers may take up to 50 years .

While tumor progression timelines may vary for different cancers, these studies share the implications that a period of at least 20 years since inception of the first malignant cell should pass before a primary tumor becomes detectable.

Our modeling results can also be correlated with published comprehensive genomic studies of clinically annotated HGSOC samples. For example, The Cancer Genome Atlas Research Network examined 489 HGSOC tumor samples, and provided the most comprehensive and integrated catalogue of (epi)genomic changes associated with HGSOC progression to date [118].

An outcome of our model is that an estimated 5 to 8 infrequent, rate-limiting events associated with changes in the initial growth saturation rate, $\mathrm{k}_{\mathrm{decay}}$, are required to reach a baseline TVU detectable or life-threatening untreated HGSOC tumor volume.

Additionally, we note the substantial heterogeneity in the number of such genomic aberrations predicted by our model, and observe that on average, one or two extra events are required in order for a detectable HGSOC tumor volume to become life-threatening. Our modeling findings align with the reported heterogeneity and number of the HGSOC-associated pathways altered in clinical HGSOC samples, as identified in [118] (see Figure 3 therein).

Our mathematical modeling approach also represents a novel *in silico* framework aimed at modeling HGSOC growth and progression. Surprisingly, few similar mathematical modeling inferences regarding the evolution of ovarian cancers or estimating the efficacy of various ovarian cancer screening strategies have been published to date.

Durrett *et al.* developed a multi-type branching processes model for ovarian cancer growth and progression to estimate the window of opportunity for screening, which they define as the time during which TVU-based tumor detection can result in a significantly reduced chance of mortality [71]. Based on their mathematical analysis, a window of opportunity of 2.9 years is predicting, implying that ovarian cancer screening should occur at least biannually.

In another example, Brown and Palmer used a Monte Carlo method to fit an exponential *in silico* model for tumor growth, with separate growth rate parameters for early and advanced stage serous ovarian cancers [72]. The Brown and Palmer study was based on occult tumor size data collected from healthy germline BRCA1 mutation carriers who had their ovaries and Fallopian tubes prophylactically removed. They estimated the window of opportunity for TVU detection of early stage occult serous cancers to be 4.3 years, and predicted that most serous cancers would progress to an advanced stage a median of 0.8 years prior to clinical, surgical detection.

Nonetheless, these existing mathematical efforts, conducted towards modeling ovarian carcinogenesis or estimating the efficacy of various ovarian cancer screening strategies, do not properly account for the considerable degree of heterogeneity of the disease [57, 118] and correlate primary tumor size with metastatic potential, disregarding clinically reported findings of low primary tumor volume advanced-stage HGSOCs or large primary tumor volume early-stage HGSOCs [94].

In contrast, our mathematical investigation focuses specifically on modeling HGSOC growth and progression, and does not link primary tumor volume to metastatic potential. Moreover, our findings show that multiple frequency TVU monitoring across various TVU detection sensitivities does not significantly improve the detection of HGSOC tumor volumes in an *in silico* cancer-positive HGSOC population.

Several limiting assumptions were made in our model. First, we do not distinctly address the underlying mechanism behind either HGSOC initiation or its progression, but it is well known that many factors may contribute to HGSOC carcinogenesis and progression (e.g., loss of function of tumor suppressor gene *p53* and the disruption of the homologous recombination repair pathway via somatic or germline mutations of the *BRCA1* and *BRCA2* genes [10, 57, 118]).

Second, we assume that the initiation of HGSOC occurs at some point during a womans premenopausal stage, and we increment time in intervals of 28 days (the average length of a menstrual cycle) to reflect subsequent potential changes in the growth saturation rate. A clinically recognized risk factor for HGSOC progression is the number of ovulatory events during a woman's lifetime [73, 94].

Third, we do not associate a direct cost to a more rapid cell cycle time (or faster doubling time), even though one probably does exist *in vivo*. Given the model sensitivity to initial conditions (the initial tumor growth rates), we chose conservative baseline TVU detection and life-threatening volume thresholds. Variation in the model parameters or baseline thresholds would only result in a faster or delayed HGSOC progression, but would not yield substantially different median or range values for the estimated cdf's. A reasonable parameter set range would, however, enable us to obtain sharper estimates.

Finally, it is possible that HGSOC rates of cellular division may vary within different subcellular populations belonging to the tumor volume. For simplicity, we do not distinguish between the various subpopulation growth rates, as such values are difficult to quantify empirically.

3.4.1 Conclusions

The HGSOC growth and progression model presented here represents an initial and novel attempt to model *in silico* a clinically occult pathological process, and obtain quantitative estimates of otherwise unknown statistics that are impossible to obtain even in large-scale prospective cohort screening studies (i.e., the time needed to reach baseline TVU detectability, the time needed to reach baseline life-threatening untreated tumor volume, and the window of opportunity interval length).

Our mathematical model provides a quantitative mathematical explanation that supports clinical findings such as the ones reported in [101] and results from prospective TVU screening trials such as the UKTOCS or PLCO, and thus represents a novel attempt to explain why multiple, large-scale TVU-based HGSOC detection screening studies have not proven significant mortality benefits.

Our model is consistent with case reports and prospective TVU screening population studies in that a key prediction of our model is that HGSOC detection is not amenable to frequent TVU monitoring. The mathematical model provides support to the empirical recommendation against frequent HGSOC monitoring or screening [26].

Chapter 4: Modeling Ovarian Cancer Cell Growth Dynamics *In Vitro* in Response to Antimitotic Drug Treatment

The results in this chapter were published in [59]. It focuses on a mathematical study of ovarian cancer cellular population growth dynamics and therapeutic administration *in vitro*.

4.1 Introduction to Antimitotic Therapies

Intratumoral cancer heterogeneity represents a major obstacle to improving the overall response and survival of cancer patients [119–122]. While most tumors initially respond well to drug therapies, many will relapse at a certain point following treatment [123, 124]. One of the major reasons behind therapeutic failure is attributed to cancer cell-intrinsic factors, such as variations in cell-cycle parameters, (e.g., cell-cycle duration, apoptosis length, mitotic index, percentage of apoptotic cells) and the presence of quiescent cancer cells, both which decrease the efficacy of therapies that rely on active cell-cycling [125–128].

Antimitotic cancer drugs represent a highly diverse and successful class of antimitotic agents, reported to have a broad spectrum of potent anti-tumor activity in various hematological and solid malignancies, including ovarian cancers [129–

136]. Examples of such drugs include microtubule-targeting agents, e.g., taxanes and vinca alkaloids, and newer agents that disrupt mitosis without affecting microtubule dynamics, e.g., kinesin spindle protein inhibitors and inhibitors of mitotic kinases [137–147].

While the primary drug target depends on the antimitotic agent used, preclinical data from *in vitro* experiments showed that prolonged mitotic arrest occurs in 100% of the cell populations under study irrespective of the agent used [148–152]. However, these data also revealed that while all proliferating cells will undergo mitotic arrest when exposed to high concentrations of antimitotic drugs, there is considerable cell-to-cell variation of apoptotic response to antimitotic drugs in human cancer cell lines.

Such observations have been reported in multiple single cell studies involving individual cancer cells in culture in the presence of various antimitotic drugs, including kinesin-5 inhibitors [149,151], taxol [148,150–156], and nocodazole [151,157–159]. In the presence of identical drug exposure times and concentrations, the extent of heterogeneity in cellular response reported both within and across cancer cell lines is considerable [148–152, 154–156].

For example, in [151], the authors analyzed 15 different cancer cell lines for their long-term response to different antimitotic drugs. They found that cellular responses to identical drugs are heterogeneous, e.g., within each distinct cell line, cells exhibit different responses following prolonged mitotic arrest, such as undergoing apoptosis after exiting mitosis, dying after completing several mitoses, or dying in interphase.

Investigating the role of intrinsic cell heterogeneity emerging from variations in cell-cycle parameters and apoptosis in ovarian cancer cell growth dynamics *in vitro* is a crucial first step towards better informing antimitotic drug administration in the treatment of ovarian cancers.

4.1.1 Previous Work

Several mathematical models have been formulated to investigate the dynamic variations among different cellular phenotypes and their role in the emergence of adaptive evolution and chemotherapeutic resistance [160–164], or the impact of cancer cell size, age and cell-cycle phase in predicting the long-term *in vitro* population growth dynamics [165–174].

For example, in [165], the authors modeled the cancer cell population dynamics using a system of four partial differential equations (PDEs) representing the four cell-cycle phases (i.e., G_0, G_1, S and M) with relative DNA content as the structuring variable. The goal therein was to obtain the steady DNA distributions for each cell-cycle phase, and match the flow cytometry DNA profiles of the human melanoma NZM13 cell line at various timepoints following the addition of paclitaxel.

In [167], the authors derived two novel mathematical models, a stochastic agent-based model and an integro-differential equation model, in order to study the effect of cell-cycle induced intrinsic tumor heterogeneity on the overall growth dynamics of the OVCAR-8 human ovarian carcinoma cell line. Both models characterized the growth of OVCAR-8 cancer cells as dynamic interactions between the proliferative, quiescent and apoptotic states. The models were designed to predict the cancer growth as a function of the intrinsic heterogeneity in the duration of the cell-cycle and apoptosis process, and also included cellular density dependency effects. An extension of these models to spatial models was done in [168].

4.1.2 Model Findings

In this chapter, we reformulate the models of [167]. Specifically, we assume that cells are structured by their age, i.e., how long each cell will spend in the cell-cycle or apoptosis. The advantages of the present approach lie in the ability to access directly the cellular age in each compartment, and to study the impact of prolonged mitotic arrest induced by antimitotic agents on the long-term ovarian cancer growth dynamics. Our model comprises of two PDEs for the proliferative and apoptotic cell compartments structured in cellular age, and one ordinary differential equation for the quiescent compartment.

We model the prolonged mitotic arrest induced by the drug as an increase in the average cell-cycle length duration, a consequence of the slowing or blocking of mitosis at the metaphase-anaphase transition [149, 153, 157, 175]. We assume that if the total time a cell spends in the cell-cycle is greater than the cell-cycle age threshold, apoptotic cell death is triggered, a phenomenon observed *in vitro* [137, 149, 152, 153, 156, 157, 175–181]. We use numerical simulations to subsequently study the impact of increasing the cell-cycle length on the overall population survival.

Our results suggest that at confluence and in the absence of any drug, quiescence is the long-term asymptotic behaviour emerging from the ovarian cancer cell growth dynamics. This pattern is maintained in the presence of a small increase in the average cell-cycle length. However, an intermediate increase in cell-cycle length markedly decreases the total number of cancer cells present, and can drive the cell population to extinction. A large "switch-on/switch-off" increase in the average cell-cycle length maintains an active cell population in the long-term, with oscillating numbers of proliferative cells and a relatively constant quiescent cell number. Intriguingly, our results suggest a large "switch-on/switch-off" increase in the average cell-cycle length may maintain an active cancer cell population in the long-term.

This work is aimed at understanding ovarian cancer cell growth dynamics in the context of cancer heterogeneity emerging from variations in cell-cycle and apoptosis parameters. The mathematical modeling framework proposed herein merits consideration as one of the few mathematical models to investigate dynamic cancer cell responses to prolonged mitotic arrest induced by antimitotic drug exposure. Our proposed modeling framework can serve as a basis for future studies of the heterogeneity observed *in vitro* of cancer cell responses in the presence of antimitotic drugs.

4.2 Modeling Approach

4.2.1 Model Setup

The system (4.1)-(4.3) is a novel physiologically motivated mathematical model that assumes continuous distributions on cellular age, i.e., the times spent in the cell-cycle and apoptosis process. The model consists of proliferative (i.e., cells actively dividing, in either a G_1, G_2, or M-like state), quiescent (i.e., a G_0-like state), and apoptotic compartments, as illustrated in Figure 4.1.

The proliferative compartment is structured by the time remaining to be spent by cells in the cell-cycle before successfully completing mitosis and doubling. The apoptotic compartment is structured by the time remaining for cells to fully degrade and complete apoptosis. Accordingly, the dynamics of the cancer cell population is governed by the following system:

$$\partial_t P(t,a) - \partial_a P(t,a) = \alpha_{QP}(t) Q(t) f_P(a) \mathbb{1}_{[0,\bar{a}]} - \alpha_{PA}(t) P(t,a), \tag{4.1}$$

$$\partial_t Q(t) = 2P(t,0) - (\alpha_{QP}(t) + \alpha_{QA}(t)) Q(t), \tag{4.2}$$

$$\begin{aligned} \partial_t A(t,a) - \partial_a A(t,a) = \Bigg[& \alpha_{QA}(t) Q(t) + \alpha_{PA}(t) \int P(t,a)\, da \\ & + \alpha_{QP}(t) Q(t) \int f_P(a) \mathbb{1}_{(\bar{a},\infty)}\, da \Bigg] f_A(a). \end{aligned} \tag{4.3}$$

Initial conditions for this system are described below.

4.2.2 Model Description

In these equations, $P(t,a)$ represents the number of proliferative cells at time t that still spend a in this compartment before doubling. The rates of change of $P(t,a)$ with respect to the experimental time course t and age a are represented by ∂_t and ∂_a, respectively. The term $\partial_a P(t,a)$ in Equation (4.1) implies that the time remaining until proliferating cells complete the cell-cycle decreases as time t advances.

When entering the cell-cycle, each cell is assigned its individual amount of time

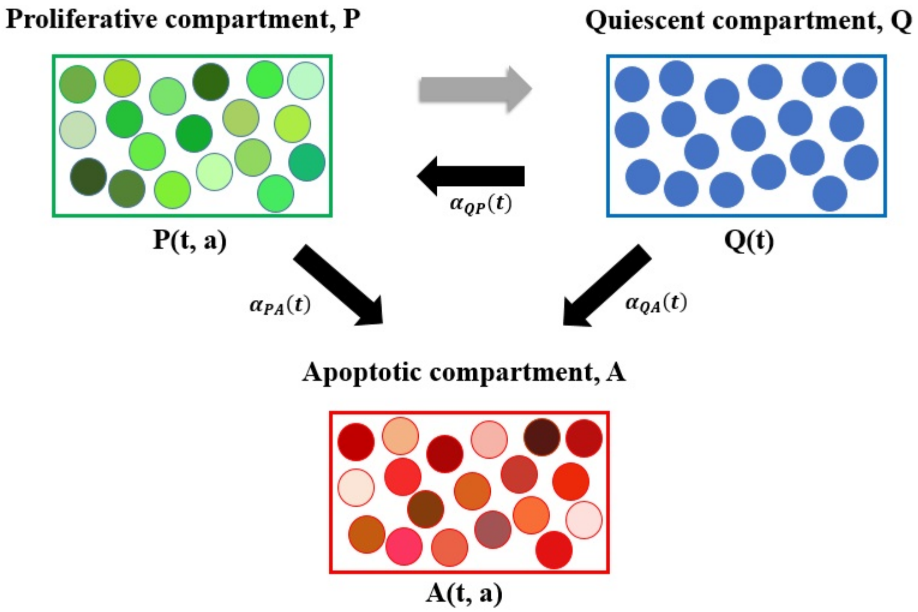

Figure 4.1: Proliferative cells can either transition to A or to Q at $a = 0$ upon completion of the cell-cycle. Quiescent cells can either transition to P with rate $\alpha_{QP}(t)$, or to A with rate $\alpha_{QA}(t)$. For illustration purposes, cells within each compartment are grouped together. The various shades of green represent the different times remaining to be spent by cells in the proliferative compartment (i.e., in the cell-cycle) before transitioning. Similarly, the various shades of red represent the different times remaining to be spent by cells in the apoptotic compartment, before completing apoptosis and being removed from the numerical simulations. The three explicit transition rates (i.e., $\alpha_{QP}(t)$, $\alpha_{PA}(t)$, and $\alpha_{QA}(t)$) are illustrated using black arrows pointing in the direction of the respective transition. The implicit transition from P to Q representing the successful completion of the cell-cycle is denoted by a grey arrow.

to be spent cycling, i.e., a, which is randomly selected from the Gaussian distribution function with mean μ and standard deviation σ, and probability density function $f_P(a)$. When reaching $a = 0$, cells in P exit the cell-cycle. The maximum length of time spent in P before exiting thus corresponds to the maximum length of the mitotic arrest induced by an antimitotic drug. We assume that the transition of cells back to Q is due to a successful (i.e., non-aberrant) mitosis.

Cells in Q act as a reservoir for the other two compartments, i.e., they either move into the apoptotic or proliferative compartment with rates $\alpha_{QA}(t)$ or $\alpha_{QP}(t)$, respectively. Intuitively, quiescent cells are not actively progressing through the cell-cycle, nor are committed to undergo apoptosis (i.e., they remain in a G_0-like state).

Cells can undergo apoptosis immediately after exiting the cell-cycle, after completing several mitoses, or during interphase. Once cells enter A, they are irreversibly committed to completing apoptosis, and cannot transition back to either P or Q. When apoptosis is completed, cells are removed from the numerical simulation. The term $\partial_a A(t, a)$ in Equation (4.3) implies that the time remaining until cells complete apoptosis decreases as time t advances.

Cells undergoing apoptosis take time to fully degrade [182,183]; until apoptosis is completed, the cells still take up space and can inhibit the growth of neighboring cells *in vitro* [156, 183]. Upon entering the apoptosis compartment, the time remaining to be spent there is randomly chosen from a probability distribution, e.g., Gamma distribution $\Gamma(\omega, \lambda)$ with shape parameter ω, rate parameter λ, and probability density function $f_A(a)$. The choice for this probability distribution is explained in greater detail in Section 4.2.5.

We note that the two age-structured PDEs for the proliferative and apoptotic cell compartments enable us to monitor a cell's progress through the cell-cycle (in the case of a cell in P), or advancement through apoptosis until complete degradation (in the case of a cell in A).

Additionally, we assume that if, upon entering P, the time a cell will spend in P, a, is greater than the threshold $\bar{a}$ (i.e., the cell-cycle age threshold corresponding to a prolonged mitotic arrest), the cell will undergo apoptosis, and will thus immediately transition to A. This phenomenon has been observed *in vitro* when the sustained prolonged mitotic arrest caused by antimitotic drug exposure leads to apoptotic cell death via the gradual accumulation of cell death signals that ultimately trigger apoptosis. Examples include the phosphorylation and subsequent inactivation of the anti-apoptotic Bcl-2 proteins (Bcl-2, Bcl-xL, and Mcl-1), PARP cleavage, and the activation of caspases 3, 7, and 9 [152,153,155–157,177,184–186].

4.2.3 Initial Conditions

Initial conditions for the system (4.1)-(4.3) are as follows:

$$P(0,a) = 0, \tag{4.4}$$

$$Q(0) = \rho(0)K, \tag{4.5}$$

$$A(0,a) = 0, \tag{4.6}$$

where $\rho(0)$ represents the initial *in vitro* plating density. Here, three different initial conditions are used, i.e., $Q(0) = 0.1\ K$, $Q(0) = 0.45\ K$, and $Q(0) = 0.8\ K$, corresponding to 10%, 45%, or 80% of the plating carrying capacity K, respectively, according to experimental setup in [167]. We note that the $Q(0) = 0.1\ K$ and $0.8\ K$ cases are identical to the initial conditions reported in [167]. For comparison purposes, we consider in this work an intermediate case, $Q(0) = 0.45\ K$, which corresponds to the mean value of the two experimental datasets reported in [167]. Therein, the OVCAR-8 growth dynamics measuring total cellular density every 24 hours for a period of 96 hours in the two different seeding densities (i.e., 10% and 80% of the *in vitro* plating density) was subsequently recorded. For a more detailed description of the experimental design, we refer to [167, Appendix B.1.2].

We note that Equation (4.1) does not require a boundary condition at $a = 0$, since this is a PDE that models a transport process with outward flux only, i.e., once proliferating cells reach $a = 0$, they double, after which both daughter cells return to quiescence before entering another cell-cycle.

4.2.4 Inter-compartmental Dynamics

Following [167], the OVCAR-8 transition rates that describe the processes of mitotic exit followed by quiescence, mitotic exit or quiescence followed by the onset of apoptosis are, respectively:

$$\alpha_{QP}(t) = c\tfrac{[\beta(\rho(t))N_{tot}(t) - P(t)]_+}{Q(t)}, \tag{4.7}$$

$$\alpha_{PA}(t) = c\gamma\tfrac{[dN_{tot}(t) - A(t)]_+}{P(t)}, \tag{4.8}$$

$$\alpha_{QA}(t) = c(1-\gamma)\tfrac{[dN_{tot}(t) - A(t)]_+}{Q(t)}. \tag{4.9}$$

$P(t)$, $Q(t)$, and $A(t)$ represent the total number of cells at time t in the proliferative, quiescent, and apoptotic compartments. Herein, the total number of proliferative and apoptotic cells are integrated over the cellular age, i.e., $\int P(t,a)\,da$ and $\int A(t,a)\,da$, respectively. The total number of cells which occupy the plate at time t is described by $N_{tot}(t) = P(t) + Q(t) + A(t)$. The total number of non-apoptotic cells at time t is described by $N(t) = P(t) + Q(t)$. OVCAR-8 cell density is denoted by $\rho(t) = N_{tot}(t)/K$, with K representing *in vitro* confluence. Here, $\rho = 1$ when $N_{tot}(t) = K$ implies that cells have reached confluence at time t. For a complete explanation and derivation of the transition rates in (4.7)-(4.9) we refer to [167].

We note that the functional forms in Equations (4.7)-(4.9) are time- and density-dependent, and reflect the *in vitro* experimental conditions used in [167], where OVCAR-8 cells were seeded at different cell densities, and initially synchronized to be quiescent using starvation media.

Additionally, we assume that for a given *in vitro* cell density at time t, there exists an equilibrium distribution of cells actively in the cell-cycle. This is represented in the model by the function $\beta(\rho(t))$, i.e., the fraction of proliferating cells as a function of the *in vitro* cell density $\rho(t)$ at equilibrium.

Experimentally, in order to determine $\beta(\rho(0))$, in [167], OVCAR-8 human ovarian carcinoma cells seeded at different cell densities were initially synchronized as quiescent, using two distinct cell-cycle arrest experiments performed by changing the starvation media and duration of the experiment. For a more detailed description of the experimental design, we refer to [167, Appendix B.1.1].

In the model, $\beta(\rho(t))$ is described by:

$$\beta(\rho) = \beta_m \, \mathrm{e}^{\frac{-\theta(\rho-\rho_m)^2}{\rho(1+\varepsilon-\rho)^2}}, \tag{4.10}$$

where θ is defined as $\theta = \frac{\varepsilon^2 \log(\frac{\beta_m}{d})}{(1-\rho_m)^2}$.

A complete list of the variables and parameters used throughout the modeling framework (4.1)-(4.10) and their interpretation can be found in Tables 4.1 and 4.2. We note that the parameters and functional forms described above are adapted from [167].

4.2.5 Intra-compartmental Dynamics

The age-structured mathematical model proposed above incorporates an intrinsic form of cell heterogeneity in the *in vitro* cancer cell growth dynamics, specifically in the distribution of times individual cells spend in the cell-cycle and apoptosis process.

To the best of our knowledge, there are no *in vitro* studies describing the distribution of times individual OVCAR-8 cells spend in the cell-cycle. In [167], Greene *et al.* chose to model the amount of time OVCAR-8 cells spend in the proliferative compartment, P, as a normal distribution, $\mathcal{N}(\mu, \sigma)$, with probability density function $f_P(a)$. In our model, the density function is re-normalized to integrate to 1 on the interval $[0, \infty)$.

Based on the temporal OVCAR-8 growth dynamics reproduced in Figure 4 in [167], the mean cell-cycle length obtained when fitting to the experimental data is $\mu = 19.12$ hours, when the initial plating density is set at $Q(0) = 10\%$ of the

Variable	**Value**	**Definition**
t	$[0, 200]$ (hours)	Time
a	$[0, 80]$ (hours)	Maximum time remaining to be spent in P or A
$P(t, a)$	$[0, \infty)$ (cells)	Number of proliferative cells at time t with time a to spend in P
$Q(t)$	$[0, \infty)$ (cells)	Number of quiescent cells at time t
$A(t, a)$	$[0, \infty)$ (cells)	Number of apoptotic cells at time t with time a to spend in A
$N_{tot}(t)$	$[0, \infty)$ (cells)	Total number of cells at time t
$N(t)$	$[0, \infty)$ (cells)	Total number of non-apoptotic cells at time t
$f_P(a)$	$[0, \infty)$	PDF of $\mathcal{N}(\mu, \sigma)$, describing the cell-cycle length without drug
$f_{P,c}(a)$	$[0, \infty)$	PDF of $\mathcal{N}(\mu + c(t), \sigma)$, describing the cell-cycle length with drug
$c(t)$	$[0, \infty)$ (hours)	Drug-induced mitotic arrest extending the average cell-cycle length
$f_A(a)$	$[0, \infty)$	PDF of $\Gamma(\omega, \lambda)$ describing the length of apoptosis
$\rho(t)$	$[0, \infty)$	*In vitro* cell density at time t
$\beta(\rho(t))$	$[0, 1]$	Fraction of total number of cells in P as a function of $\rho(t)$
$\alpha_{QP}(t)$	$[0, \infty)$	Transition rate from Q to P
$\alpha_{PA}(t)$	$[0, \infty)$	Transition rate from P to A
$\alpha_{QA}(t)$	$[0, \infty)$	Transition rate from Q to A

Table 4.1: List of variables used throughout the OVCAR-8 growth dynamics model.

Parameter	**Value**	**Definition**
ω	4.9436	Shape parameter for the length of apoptosis
λ	.19117	Rate parameter for the length of apoptosis
$\bar{a}$	$[24.23, 28.12]$ (hours)	Cell-cycle age threshold
K	40401 (cells)	*In vitro* carrying capacity
μ	$[15.23, 19.12]$ (hours)	Mean cell-cycle length without drug
σ	3 (hours)	Standard deviation of the cell-cycle length without drug
c	$[0.37, 0.64]$(hour^{-1})	Cellular reaction rate
γ	$[0.0005, 0.9999]$	Transition probability to enter A
d	0.03	Fraction of total number of cells in A
β_m	$[0, 1]$	Maximum of $\beta(\rho(t))$
ρ_m	$[0, 1]$	Maximizing density of $\beta(\rho(t))$
ε	$[0, 1]$	Parameter governing the shape of $\beta(\rho(t))$

Table 4.2: List of parameters used throughout the OVCAR-8 growth dynamics model.

maximum plating density, K. When the initial plating density is $Q(0) = 80\%$ of the maximum plating density, K, the mean cell-cycle length obtained when fitting to the experimental data is $\mu = 15.23$ hours. When fitting the system (4.1)-(4.3) to the experimental data for both plating density conditions, the mean cell-cycle length obtained is $\mu = 18.33$ hours. Experimentally, the doubling time reported for OVCAR-8 cells decreases with higher plating density, and varies between 14.57 hours (see [187]) and 26.1 hours [188].

The amount of time cells spend in the apoptosis compartment, A, is assumed to follow a Gamma distribution, $\Gamma(\omega, \lambda)$, where ω and λ denote the shape and rate parameters, respectively, with probability density function $f_A(a)$. These parameters are set at $\omega = 4.9436$ and $\lambda = 0.19117$, respectively, to match the experimental results of [182] on the length of the apoptotic process. They are identical to the ones used in [167] to characterize this process.

We note, however, that the study of [182] investigated the individual responses of PC12 rat adrenal gland tumor cells to serum deprivation. Therein, the authors performed a comprehensive study on the fate of distinct cells undergoing apoptosis following serum removal. To the best of our knowledge, no such studies performed on human cancer cell lines have reported a distribution of the time individual cells spend in apoptosis at a such a fine resolution, either in the absence or the presence of antimitotic drugs. We thus chose to model the probability density function of the length of apoptosis process based on the experimental data in [182]. The remaining model parameters listed in Table 4.2 are obtained following the parameter estimation procedure described in [167].

4.2.6 Cellular Response to Antimitotic Drugs

In our model, we consider an antimitotic drug whose effect on the OVCAR-8 cellular dynamics is to induce mitotic arrest, extending the average cell-cycle length. We assume the administered drug to be homogeneously distributed, such that all cells in P are equally susceptible to its effect.

Specifically, the impact of the drug is to increase the time cells spend in the proliferative compartment, P, corresponding to a sustained mitotic arrest. Upon exiting quiescence and entering the cell-cycle, a cell can undergo one of two fates: i) if the time chosen to be spent in P is lower than the threshold $\bar{a}$, the cell enters P, progresses through the cell-cycle, and either successfully completes mitosis with rate α_{QP}, or undergoes apoptosis with rate α_{PA}; ii) otherwise, the cell commits to undergoing apoptosis, and immediately moves to the apoptotic compartment, A. The parameter $\bar{a}$ serves as the cell-cycle age threshold corresponding to a prolonged mitotic arrest, after which cells exit the cell-cycle and undergo apoptosis.

It is a well-known phenomenon *in vitro* that a sustained mitotic arrest (i.e., slowing or blocking of mitosis at the metaphase-anaphase transition, thus increasing cell-cycle length), predisposes cancer cells to undergoing apoptosis following mitotic exit [129, 130, 137, 149, 152, 153, 155–157, 175, 186]. This was revealed using time-lapse microscopy data, where exposure of cancer cells to saturating antimitotic drug concentrations delayed to various extents the cells from exiting drug-induced mitotic arrest and undergoing subsequent apoptosis.

In our model formulation, the antimitotic drug acts directly on the OVCAR-8 cell-cycle dynamics by increasing the average cell-cycle length, and as a consequence, causing cells to transition to the apoptotic compartment. To include the effect of such a drug, we shift the expected value μ of the normal distribution by the function $c(t)$ corresponding to the cell-length increase induced by the antimitotic drug, i.e., $f_{P,c}(a)$ is the probability density function of the normal distribution $\mathcal{N}(\mu + c(t), \sigma)$. The system (4.1)-(4.10) remains otherwise unchanged. Here, $c(t)$ can, for example, be modeled as a constant or bang-bang function throughout the duration of the simulation time $t = 200\text{h}$, corresponding to either a sustained, constant mitotic arrest or a switch-on/switch-off arrest.

Experimentally, the sustained, constant mitotic arrest corresponds to the large cell-to-cell variations in the duration of mitotic arrest and the timing of drug-induced cell death via apoptosis observed *in vitro* when single cells are exposed to saturating drug concentrations using various antimitotics for prolonged periods of time, e.g., 96 hours or more [151, 152, 156].

We further investigate the impact of an *in silico* switch-on/switch-off mitotic arrest on the overall OVCAR-8 cancer cell growth dynamics. This type of "bang-bang" mitotic arrest could, for example, be induced *in vitro* by the periodic addition and wash-off of the antimitotic drug under study, along with growth media refreshment. In this setting, when the drug is withdrawn, proliferating cells do not necessarily revert to the cell-cycle length assigned to them in the absence of the drug. Rather, these cells can still undergo a period of mitotic arrest, in which the progression through the cell-cycle can be slowed down or blocked, leading to an increase in the cell-cycle length, after which the cell-cycle is completed and cells exit proliferation.

We note that our age-structured modeling framework allows us to estimate the number of cells present in each compartment at any given time, and to temporally trace the distribution of the times remaining to be spent in the proliferative phase during the cell-cycle or in the apoptotic phase. This framework enables us to dynamically estimate the amount of time remaining to be spent in each of these processes, and to track cells in their progression through each cellular phase.

4.2.7 Remarks

In [167], Greene *et al.* recently proposed two mathematical frameworks for studying the role of cell density in the dynamics of the propagation of intrinsic drug resistance: a stochastic agent-based model (ABM) and an integro-differential equation (IDE) model, each describing the growth of cancer cells as dynamic transitions between the proliferative, quiescent and apoptotic states.

These models incorporated an intrinsic form of cellular heterogeneity in the durations of the cell-cycle and the apoptosis process. They were designed to predict the cancer cell growth as a function of the intrinsic heterogeneity in the durations of the cell-cycle and the apoptosis process, and included cellular plating density dependencies. Model parameters were estimated in [167] using experimental data collected from the OVCAR-8 cell line (i.e., *in vitro* growth rate, cell density and apoptosis fraction measurements).

For example, in the IDE model, the dynamics of the proliferative (N_p), quiescent (N_q), and apoptotic (N_a) compartments, respectively, are governed by:

$$\begin{aligned}\frac{\mathrm{d}}{\mathrm{d}t}N_p(t) &= \alpha_p(t)N_q(t) - \alpha_{a_p}(t)N_p(t)\\ &\qquad - \int_0^t f_p(t-t_*;\mu,\sigma)\alpha_p(t_*)N_q(t_*)\left(1-\int_{t_*}^t \alpha_{a_p}(s)\,\mathrm{d}s\right)\mathrm{d}t_*,\end{aligned} \tag{4.11}$$

$$\begin{aligned}\frac{\mathrm{d}}{\mathrm{d}t}N_q(t) &= -\alpha_{a_q}(t)N_q(t) - \alpha_{a_p}(t)N_q(t)\\ &\qquad + 2\int_0^t f_p(t-t_*;\mu,\sigma)\alpha_p(t_*)N_q(t_*)\left(1-\int_{t_*}^t \alpha_{a_p}(s)\,\mathrm{d}s\right)\mathrm{d}t_*,\end{aligned} \tag{4.12}$$

$$\begin{aligned}\frac{\mathrm{d}}{\mathrm{d}t}N_a(t) &= \alpha_{a_q}(t)N_q(t) + \alpha_{a_p}(t)N_p(t)\\ &\qquad - \int_0^t f_a(t-t_*)\alpha_{a_q}(t_*)N_q(t_*)\mathrm{d}t_* - \int_0^t f_a(t-t_*)\alpha_{a_p}(t_*)N_p(t_*)\mathrm{d}t_*.\end{aligned} \tag{4.13}$$

Here, α_p, α_{a_p}, and α_{a_q} represent the transition rates between compartments. The exact formulation of these transition rates was described in Section 4.2.4. The factor of 2 on the right hand side of Equation (4.12) denotes a successful mitosis, where a mother cell in the proliferative compartment completes the cell-cycle, and 2 daughter cells enter the quiescent compartment.

Additionally, μ and σ are the mean and standard deviation of the cell-cycle length, assumed to be a normally distributed random variable with corresponding probability density function $f_p(\cdot)$. Apoptosis is assumed to vary according to a fixed Gamma distribution with the density function $f_a(\cdot)$, following the experimental data from [182].

By examining the role the parameters played in the evolution of the intrinsic tumor heterogeneity in the absence of any drug, the authors concluded that the distribution in the cell-cycle length has the most significant contribution to the cancer growth dynamics.

The models of [167] were extended in [168] to include different initial geometric seeding arrangements of OVCAR-8 cells exposed to paclitaxel, an antimitotic drug, in order to investigate and quantify the spatiotemporal density of cancer cells. The spatiotemporal differences in cancer cell growth rates, and proportions of proliferative and apoptotic cells were shown to influence the evolution of intratumoral heterogeneity under anti-mitotic drug exposure. The effects of paclitaxel on the cancer cell growth dynamics were quantified, based on a stochastic ABM framework.

Therein, the authors assumed cell movement could be described by a stochastic differential equation, which took into account attractive and repulsive forces between cells. Additionally, transitions between the proliferative, quiescent, and apoptotic compartments were also included in the model. By keeping the global plating cell density constant, Greene *et al.* concluded that cell movement and local plating conditions are responsible for the significant differences in cancer cell proliferation and paclitaxel-induced apoptosis rates across the different seeding arrangements.

We note that the IDE model presented in [167] represents a sophisticated continuum mathematical formulation that enabled the authors to estimate the expected values of the number of cells in time in each of the three cellular compartments, i.e., proliferative, quiescent and apoptotic. Their IDE modeling results are based on the ability to provide accurate approximation of the stochastic ABM dynamics, using the individual ABM realizations. Their numerical simulations thus demonstrated that the IDE is able to faithfully describe the cellular dynamics of the ABM, and that given a wide range of model parameters, the results obtained from both models fit the OVCAR-8 experimental data.

The age-structured mathematical model we propose here is a novel alternative to the ABM and IDE models previously published in [167, 168]. The intrinsic heterogeneity in time cells spend in these compartments governs the population growth dynamics and dictates the response to anti-mitotic therapy. Using an age-structured modeling framework allows us to estimate the number of cells present in each compartment at any time, and to temporally trace the distribution of the times remaining to be spent in the proliferative phase during the cell-cycle or in the apoptotic phase.

In contrast, this information was not accessible in the IDE model, as the only quantities that were followed over time were the total number of cells in each compartment. This information could have been obtained from the ABM, but had to be extracted from the multiple individual agents, and hence was not amendable to optimization or other algorithms that function better with continuous densities and variables. The age-structured framework enables us to dynamically estimate the amount of time remaining to be spent in each of these processes, and to track cells in their progression through each cellular phase.

4.3 Numerical Results

4.3.1 Cancer Cell Growth Dynamics in the Absence of the Drug

We illustrate in Figure 4.2 the OVCAR-8 cancer cell growth dynamics modeled by the system (4.1)-(4.3), with transition rates (4.7)-(4.9), and initial conditions (4.4)-(4.6). Specifically, we consider three sets of initial conditions, i.e., $Q(0) =$

0.1 K in Figures 4.2(a), 4.2(d), and 4.2(g), $Q(0) = 0.45\ K$ in Figures 4.2(b), 4.2(e), and 4.2(h), and $Q(0) = 0.8\ K$ in Figures 4.2(c), 4.2(f), and 4.2(i), corresponding to 10%, 45%, or 80% of the plating carrying capacity, K, respectively.

The initial plating density, with all cells being experimentally synchronized as quiescent (described in Section 4.2.3) substantially alters the overall growth dynamics throughout the simulation time. This can be observed in the relative and absolute numbers of proliferating cells (solid green line), or quiescent cells (solid blue line), and in the total number of cells, i.e., proliferating and quiescent cells (solid magenta line).

In the $Q(0) = 0.1\ K$ case, the ratio $Q/P = \frac{Q(t)}{\int P(t,a)\,da}$ (henceforth referred to as Q/P) is greater than 1 until around $t = 2$ hours, after which it becomes smaller than 1 until around $t = 63$ hours. Afterwards, the ratio Q/P increases with time. In the $Q(0) = 0.45\ K$ case, the ratio Q/P becomes less than 1 only for a brief period of time, $t \in [7, 13]$, after which it continues to increase with time. In the $Q(0) = 0.8\ K$ case, the number of quiescent cells only decreases for a brief period of time, $t \in [0, 11]$, after which the number of quiescent cells continues to increase until almost reaching carrying capacity. The ratio Q/P remains higher than 1 throughout the duration of the simulation.

For comparison purposes, we also illustrate the distribution of the times remaining to be spent in the proliferative (P), or apoptotic (A) compartment at the end of simulation time ($t = 200$ hours), for each of the initial plating densities: $Q(0) = 0.1\ K$ in Figure 4.2(g), $Q = 0.45\ K$ in Figure 4.2(h), and $Q(0) = 0.8\ K$ in Figure 4.2(i). The solid green lines correspond to the distribution of the time

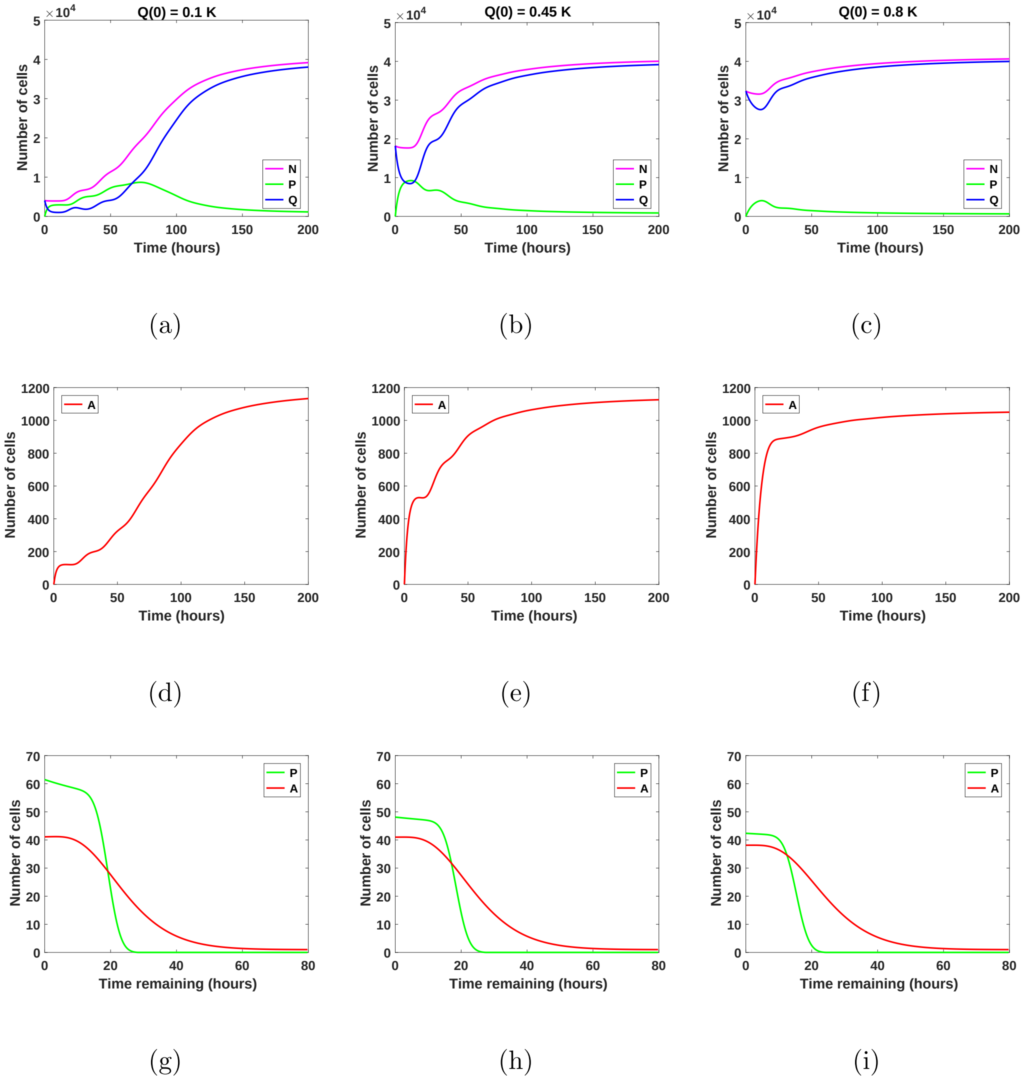

Figure 4.2: Numerical solutions for the system (4.1)-(4.3) in the absence of the drug with (a)-(d)-(g) $Q(0) = 10\%$, (b)-(e)-(h) $Q(0) = 45\%$, and (c)-(f)-(i) $Q(0) = 80\%$ of the *in vitro* carrying capacity, K. Panels (a), (b), and (c) show the dynamics of the proliferating (P), quiescent (Q), and the total number of non-apoptotic cells (N). Panels (d), (e), and (f) show the dynamics of the apoptotic cells (A). Panels (g), (h), and (i) illustrate the distribution of the times remaining to be spent by cells in the proliferative (P) and apoptotic (A) compartments as seen at the end of the simulation time, $t = 200$ hours, with (g) $Q(0) = 10\%$, (h) $Q(0) = 45\%$, and (i) $Q(0) = 80\%$ of plating carrying capacity, K.

remaining to be spent by cells in P, and the solid red lines to the times remaining to be spent by cells in A.

In each of the three scenarios, all cells are synchronized to be quiescent at the start of the simulation time $t = 0$ hours. The long-term dynamics of the system (4.1)-(4.3) reveals that the majority of OVCAR-8 cells are quiescent at the end of the simulation time $t = 200$ hours, with $N_{tot}(t)$ close to the carrying capacity. There are few remaining proliferating cells, suggesting that once cells approach confluence, proliferation will be inhibited. The initial plating density does not alter the quantitative nor qualitative dynamics of the apoptotic cell compartment throughout the simulation time (solid red lines). We conclude that at confluence and in the absence of the drug, quiescence is the long-term asymptotic behaviour emerging from the OVCAR-8 cancer cell growth dynamics.

4.3.2 Cancer Cell Growth Dynamics under Antimitotic Drug Action

We now investigate the dynamic behavior of the system (4.1)-(4.3) using two distinct antimitotic drug effects, i.e., a sustained, constant mitotic arrest and a switch-on/switch-off arrest, with three different levels of increase in the average cell-cycle length.

In the numerical simulations depicted below, the function $c(t)$, corresponding to the drug-induced mitotic arrest extending the average cell-cycle length, can take two functional forms: it is set to be a constant function $c(t) = \mathrm{c}_{\mathrm{arrest}}$ set at either 2, 10, or 20 hours (solid lines); or a bang-bang function $c(t) = 2\mathrm{c}_{\mathrm{arrest}}$ for $0 \leq t \leq 2$, and $c(t) = 0$ for $2 \leq t \leq 4$ hours, repeated periodically with period 4 until $t = 200$ hours (dashed lines).

4.3.2.1 Cancer Cell Growth Dynamics Given Small Increases in Cell-cycle Length

We study the cancer cell growth dynamics given the action of the drug as modeled by the system (4.1)-(4.3), with initial conditions (4.4)-(4.6).

To begin with, we consider small increases in the average cell-cycle length setting $\mathrm{c}_{\mathrm{arrest}} = 2$ hours. There is a relatively small difference between the two distinct antimitotic drug effects, see Figure 4.3 (solid versus dashed lines for each color representing the different cellular compartments). Therein, panels (a), (b), and (c) show the dynamics of the proliferating (P), quiescent (Q), and the total number of non-apoptotic cells (N). Panels (d), (e), and (f) show the dynamics of the apoptotic cells (A). Panels (g), (h), and (i) illustrate the distribution of the times remaining to be spent by cells in the proliferative (P) and apoptotic (A) compartments as seen at the end of the simulation time, $t = 200$ hours, with (g) $Q(0) = 10\%$, (h) $Q(0) = 45\%$, and (i) $Q(0) = 80\%$ of plating carrying capacity, K.

Specifically, in both cases, the number of proliferative cells, i.e., solid and dashed green lines in Figure 4.3(a), initially increases then starts to decrease at around $t = 73$ hours. The number of quiescent cells, i.e., solid and dashed blue lines in Figure 4.3(a), initially decreases, and continues to oscillate until around $t = 40$ hours, when it begins to increase with time. These oscillations are due to the

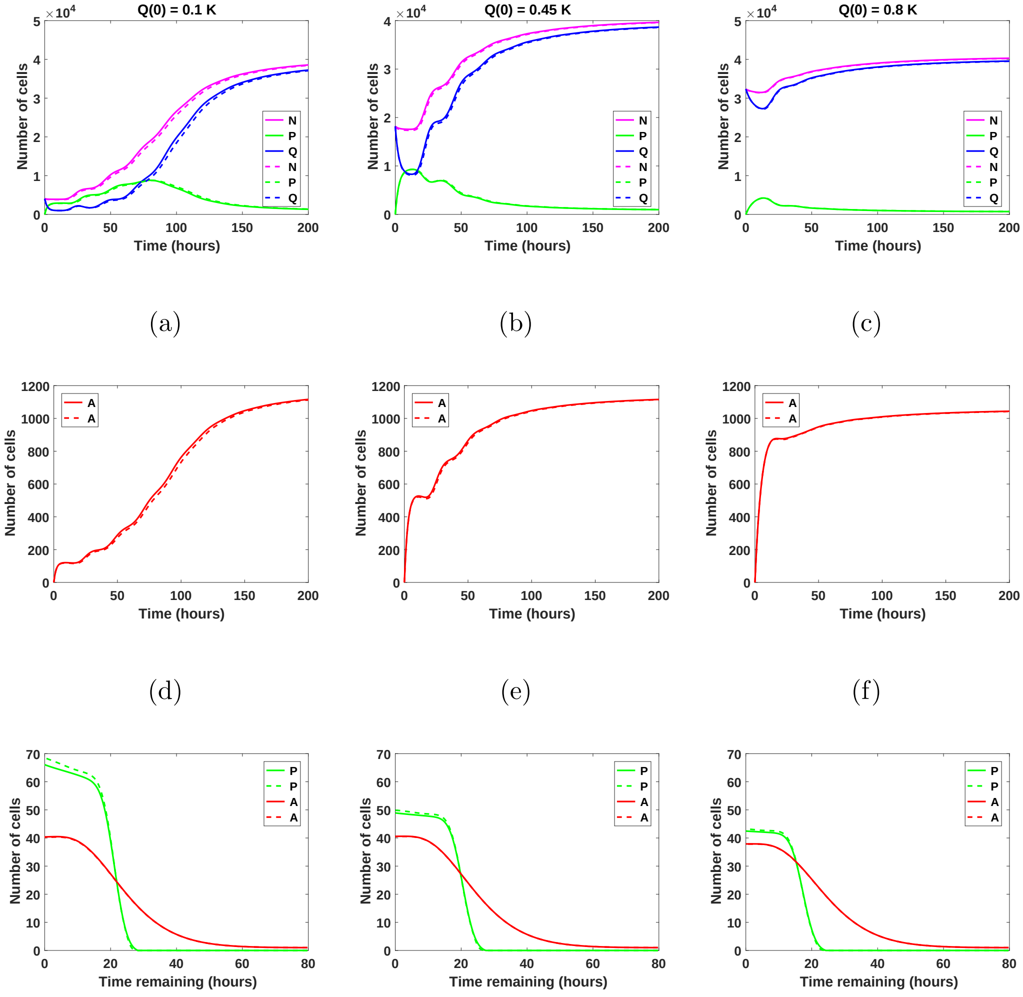

(a) (b) (c)

(d) (e) (f)

(g) (h) (i)

Figure 4.3: Numerical solutions for the system (4.1)-(4.3) given small increases in the average cell-cycle length with (a)-(d)-(g) $Q(0) = 10\%$, (b)-(e)-(h) $Q(0) = 45\%$, and (c)-(f)-(i) $Q(0) = 80\%$ of the *in vitro* carrying capacity, K. The cellular dynamics in each compartment given a sustained, constant mitotic arrest or a switch-on/switch-off arrest is illustrated using solid or dashed lines, respectively.

transitions from Q to P and back to Q. Initially, the ratio Q/P becomes less than 1 ($t \in [2, 73]$), after which it steadily increases beyond 1 throughout the rest of the simulation time.

The total number of apoptotic cells integrated over the cellular age, $\int A(t, a)\, da$, i.e., solid and dashed red lines in Figure 4.3(d), steadily increases with respect to time. In Figure 4.3(g), we show the distribution of the times remaining to be spent by proliferating cells (green lines), and apoptotic cells (red lines) at the end of simulated time $t = 200$ hours given small increases in average cell-cycle length, using the the sustained, constant mitotic arrest (solid lines) and switch-on/switch-off arrest (dashed lines).

The two antimitotic drug effects have no noticeable difference with regards to the cellular dynamics in either of the three compartments. Compared with the cancer cell growth dynamics in the absence of the drug (see Figures 4.2 and 4.3), the ratio Q/P becomes greater than 1 and subsequently increases at a slightly later timepoint, i.e., at around $t = 73$ versus $t = 63$ hours in the absence of the drug.

Similar results are obtained when considering $Q(0) = 0.45\ K$ (see Figures 4.3(b), 4.3(e), and 4.3(h)), and when considering $Q(0) = 0.8\ K$ (see Figures 4.3(c), 4.3(f), and 4.3(i)). We conclude that nearing confluence and in the presence of small increases in average cell-cycle length, quiescence emerges as the long-term asymptotic behaviour resulting from the cancer cell growth dynamics.

4.3.2.2 Cancer Cell Growth Dynamics Given Intermediate Increases in Cell-cycle Length

We now consider intermediate increases in the average cell-cycle length, setting $\mathrm{c}_{\mathrm{arrest}} = 10$ hours. Results are shown in Figure 4.4. Therein, panels (a), (b), and (c) show the dynamics of the proliferating (P), quiescent (Q), and the total number of non-apoptotic cells (N). Panels (d), (e), and (f) show the dynamics of the apoptotic cells (A). Panels (g), (h), and (i) illustrate the distribution of the times remaining to be spent by cells in the proliferative (P) and apoptotic (A) compartments as seen at the end of the simulation time, $t = 200$ hours, with (g) $Q(0) = 10\%$, (h) $Q(0) = 45\%$, and (i) $Q(0) = 80\%$ of the plate carrying capacity, K.

The case $Q(0) = 0.1\ K$ is illustrated in Figures 4.4(a), 4.4(d), and 4.4(g). Specifically, the number of proliferative cells (solid and dashed green lines) fluctuates significantly at the beginning of the numerical simulation for both antimitotic drug effects considered. However, at around $t = 77.5$ hours, the number of proliferative cells exposed to the sustained, constant mitotic arrest starts to decrease with time. The number of proliferative cells exposed to the switch-on/switch-off arrest oscillate slightly around the number of quiescent cells.

After the initial decrease in absolute numbers at around $t = 15$ hours, the quiescent cells exposed to the sustained, constant mitotic arrest exhibit a pattern of damped oscillations. They continue to slightly decrease in numbers throughout simulation time (solid blue line). The quiescent cells exposed to the switch-on/switch-off arrest seem to have reached a steady state at around $t = 88$ hours. Interestingly, for

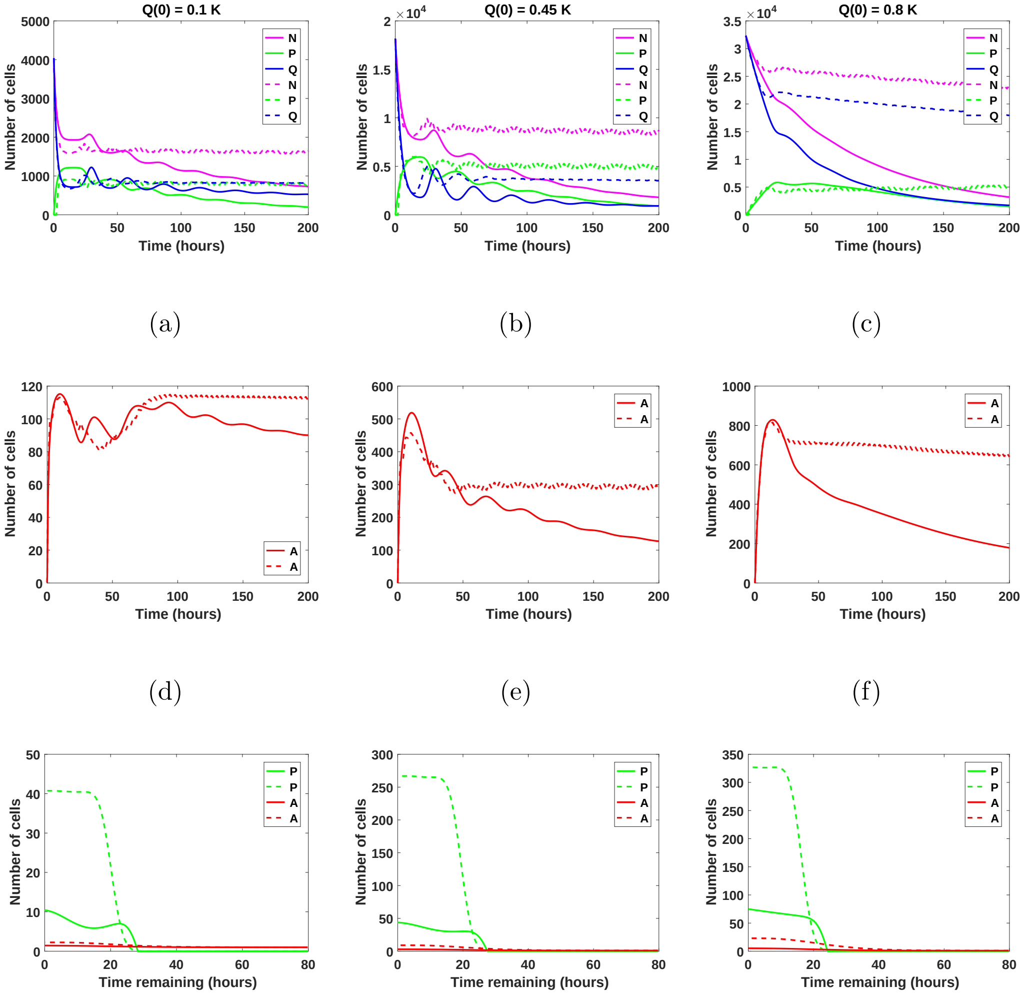

(a) (b) (c)

(d) (e) (f)

(g) (h) (i)

Figure 4.4: Numerical solutions for the system (4.1)-(4.3) given intermediate increases in the average cell-cycle length with (a)-(d)-(g) $Q(0) = 10\%$, (b)-(e)-(h) $Q(0) = 45\%$, and (c)-(f)-(i) $Q(0) = 80\%$ of the *in vitro* carrying capacity, K. The cellular dynamics in each compartment given a sustained, constant mitotic arrest or a switch-on/switch-off arrest is illustrated using solid or dashed lines, respectively.

the sustained, constant mitotic arrest, the ratio Q/P becomes greater than 1 and increases slightly with time starting at around $t = 78$ hours.

However, for the switch-on/switch-off arrest, the same ratio remains consistently around 1 throughout simulation time, suggesting the existence of a steady state equilibrium between the proliferative and quiescent populations. A similar pattern can be observed in the dynamics of the total number of proliferating and quiescent cells (solid and dashed magenta lines).

The total number of apoptotic cells (solid and dashed red lines in Figure 4.4(d)) oscillates with time. Figure 4.4(g) shows the distribution of the times remaining to be spent by proliferating cells (green lines), and by apoptotic cells (red lines) at $t = 200$ hours. Similar results are obtained when considering $Q(0) = 0.45\ K$, see Figures 4.4(b), 4.4(e), and 4.4(h).

However, for $Q(0) = 0.8\ K$, the dynamics of the proliferative (green lines), quiescent (blue lines), and apoptotic (red lines) cell compartments are quantitatively and qualitatively distinct between the two distinct antimitotic drug effects, see Figures 4.4(c), 4.4(f), and 4.4(i).

Specifically, the number of proliferative cells, i.e., solid green line in Figure 4.4(c), in the sustained, constant mitotic arrest case starts to decrease around $t = 50$ hours. Given the switch-on/switch-off arrest however, the number of proliferative cells oscillates slightly (dashed green line) starting around $t = 20$ hours, and continues until the end of the simulated time. The number of quiescent cells (dashed green and blue lines, respectively) continues to steadily decrease for both antimitotic drug effects, with the quiescent cells decaying at a faster rate in the sustained arrest case than in the switch-on/switch-off one, see Figure 4.4(c).

A similar pattern can be observed in the dynamics of the total number of cells (proliferating and quiescent), as represented by the solid and dashed magenta lines in Figure 4.4(c). The total number of apoptotic cells, i.e., solid and dashed red lines in Figure 4.4(f), starts to decrease at around $t = 18$ hours. In Figure 4.4(i), we show the distribution of the times remaining to be spent by proliferating cells (green lines), and apoptotic cells (red lines) at $t = 200$ hours.

The two antimitotic drug effects at intermediate increases in cell-cycle length have a marked distinct impact on the cellular dynamics in each of the three cellular compartments for the $Q(0) = 0.8\ K$ case. Specifically, the number of quiescent cells decreases in time, and implicitly, the total number of cells decreases at a slower (dashed magenta line) or faster rate (solid magenta line).

The dynamics of the cell population illustrated in Figure 4.4(c) is overall substantially different from the oscillatory dynamics observed in the $Q(0) = 0.45\ K$ and $Q(0) = 0.1\ K$ cases. We conclude that in the presence of intermediate increases in the cell-cycle length, the sustained, constant mitotic arrest markedly decreases the total number of cancer cells present. A switch-on/switch-off arrest maintains an active cell population in the long-term, with proliferative cell numbers exhibiting a steady oscillatory state, and quiescent cell numbers remaining relatively constant in time.

4.3.2.3 Cancer Cell Growth Dynamics Given Large Increases in Cell-cycle Length

We now consider increases in the average cell-cycle length, setting $c_{\text{arrest}} = 20$ hours. Results are shown in Figure 4.5. Therein, panels (a)-(f) show the dynamics of the proliferating (P), quiescent (Q), and the total number of non-apoptotic cells (N). Panels (g), (h), and (i) show the dynamics of the apoptotic cells (A). Panels (j), (k), and (l) illustrate the distribution of the times remaining to be spent by cells in the proliferative (P) and apoptotic (A) compartments as seen at the end of the simulation time, $t = 200$ hours, with (j) $Q(0) = 10\%$, (k) $Q(0) = 45\%$, and (l) $Q(0) = 80\%$ of the plate carrying capacity, K.

When the initial density is low ($Q(0) = 0.1\ K$), the number of proliferative cells given the sustained, constant mitotic arrest case (solid green line in Figure 4.5(a)) remains essentially zero for the entire simulation. Given the large increase in the average cell-cycle length induced by the drug, any cells that transition from Q to P subsequently transition to A, instead doubling successfully at the end of the cell-cycle.

However, given the switch-on/switch-off arrest, see dashed green line in Figure 4.5(a), proliferative cell numbers exhibit a steady oscillatory state throughout the duration of the simulated time. The ratio Q/P oscillates around 1 as time increases for the duration of simulation. A similar pattern can be observed in the dynamics of the total number of cells (proliferating and quiescent), as shown by the magenta lines in Figure 4.5(d).

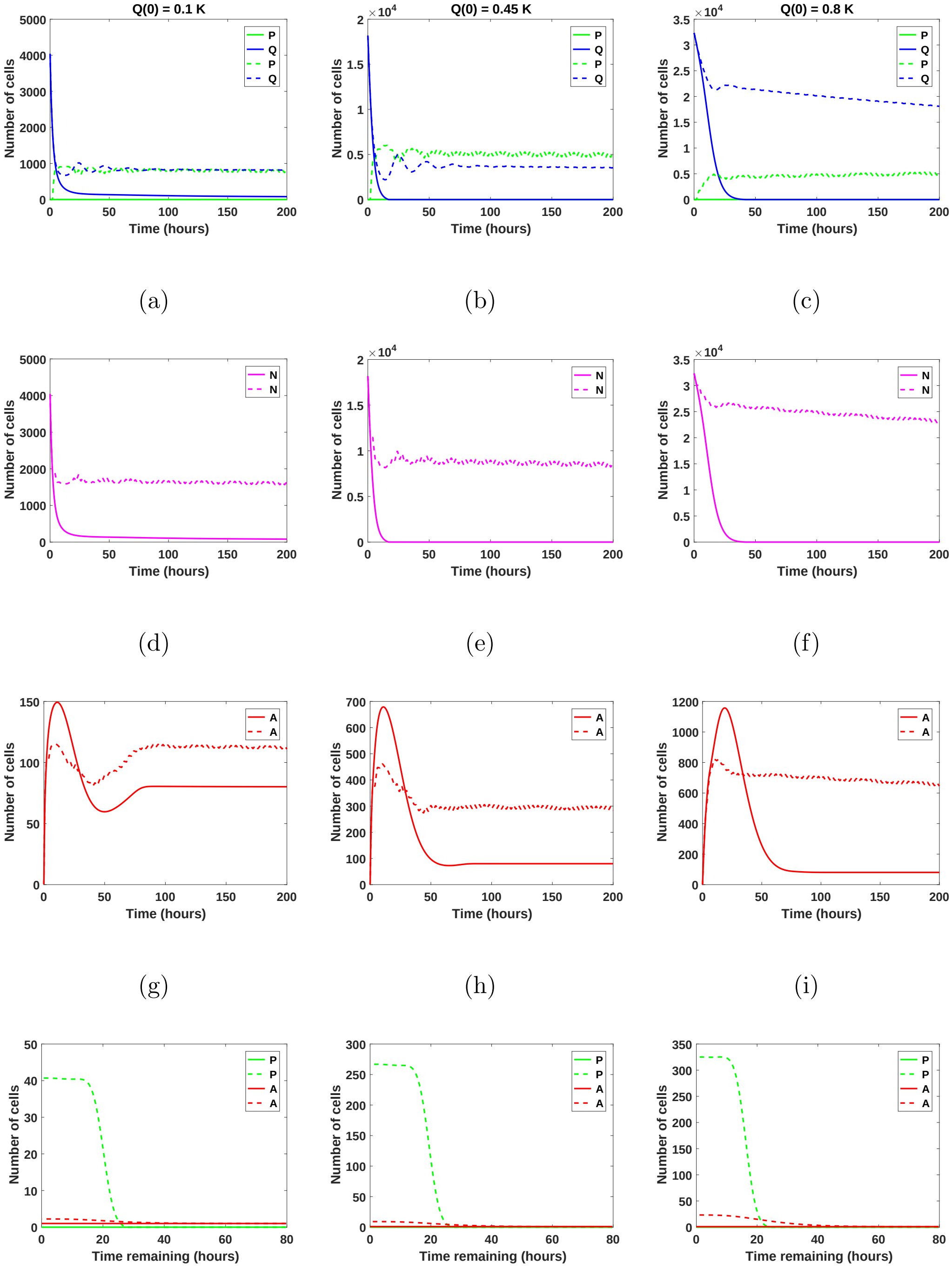

(a) (b) (c)

(d) (e) (f)

(g) (h) (i)

(j) (k) (l)

Figure 4.5: Numerical solutions for the system (4.1)-(4.3) given large increases in the average cell-cycle length with (a)-(d)-(g)-(j) $Q(0) = 10\%$, (b)-(e)-(h)-(k) $Q(0) = 45\%$, and (c)-(f)-(i)-(l) $Q(0) = 80\%$ of the *in vitro* carrying capacity, K.

The total number of apoptotic cells, i.e., solid and dashed red lines in Figure 4.5(g), oscillates with time. In Figure 4.5(j), we show the distribution of times remaining to be spent by proliferating cells (green lines), and apoptotic cells (red lines) at $t = 200$ hours.

Our numerical simulations suggest that in the presence of a sustained, constant mitotic arrest, the cancer cell population is nearly driven to extinction, see solid lines in Figures 4.5(a) and 4.5(d). Intriguingly, in the presence of a long-term switch-on/switch-off arrest, it is possible to maintain an active cancer cell population even when starting with a small initial plating density ($Q(0) = 0.1\ K$) and large increase in the average cell-cycle length.

The balance between the quiescent and proliferative cell-turnover is maintained over time, see dashed lines in Figures 4.5(a) and 4.5(d). Similar results are obtained when considering $Q(0) = 0.45\ K$, shown in Figures 4.5(b), 4.5(e), 4.5(h), and 4.5(k).

However, when $Q(0) = 0.8\ K$, the dynamics of the proliferative (green lines), quiescent (blue lines), and apoptotic (red lines) cell compartments are quantitatively and qualitatively distinct between the two antimitotic drug effects, with a clear difference between the sustained, constant and switch-on/switch-off mitotic arrest, see Figures 4.5(c), 4.5(f), 4.5(i), and 4.5(l) (solid versus dashed lines for each color representing the different cellular compartments).

Specifically, the number of proliferative cells given the sustained, constant mitotic arrest, i.e., solid green line in Figure 4.5(c), remains essentially zero for the entire simulation, similar to the 10% and 45% initial density cases. However, given the switch-on/switch-off mitotic arrest, i.e., dashed green line in Figure 4.5(c), proliferative cell numbers exhibit a steady oscillatory state throughout the duration of the simulation.

The number of quiescent cells (dashed green and blue lines, respectively) continues to steadily decrease for both drug effects, with quiescent cells decaying at a faster rate in the sustained, constant arrest case than in the switch-on/switch-off one, see Figure 4.5(c). A similar pattern can be observed in the dynamics of the total number of cells (proliferating and quiescent), as represented by the solid and dashed magenta lines in Figure 4.5(f). The total number of apoptotic cells, i.e., solid and dashed red lines in Figure 4.5(i), oscillates with time.

Our numerical simulations suggest that in the presence of a large sustained increase in the average cell-cycle length induced by the drug, the cancer cell population is nearly driven to extinction, despite the large initial starting density, see solid lines in Figures 4.5(c) and 4.5(f). Conversely, in the presence of a long-term switch-on/switch-off arrest, it is possible to maintain an active cancer cell population even when starting with a large initial plating density ($Q(0) = 0.8\ K$) and a large increase in the average cell-cycle length.

The dynamic balance between the quiescent and proliferative cell-turnover is maintained over time, see dashed lines in Figures 4.5(c) and 4.5(f). We conclude that in the presence of large increases in the average cell-cycle length induced by the drug, a sustained, constant mitotic arrest drives both the proliferating and quiescent cell numbers to extinction. A switch-on/switch-off arrest maintains an active cell population in the long-term, with proliferative and quiescent cell numbers exhibiting a steady oscillatory state in time.

4.4 Discussion of Modeling Results

The dynamics of cellular response to antimitotic drug exposure has only recently begun to be investigated *in vitro* using time-lapse microscopy on single cells in culture [137, 148, 149, 151–157, 175, 177, 184, 185].

Several studies have demonstrated that antimitotic drugs characteristically induce a period of prolonged mitotic arrest (that can last for as long as 72 hours or more) followed predominantly by cell death via apoptosis [151]. As such, mitotic arrest constitutes the first cellular response to antimitotic drug exposure, but the mechanisms behind the drug-induced prolonged mitotic arrest and subsequent cancer cell death remain, however, unclear [149–152, 154–156, 184, 185, 189].

To investigate this issue, multiple antimitotic drugs and different drug concentrations have been used in cancer cell studies. Accordingly, multiple *in vitro* single cell live imaging studies have demonstrated that cancer cells display widely varying responses to antimitotic drugs given different exposure times and drug concentrations [149–152, 154–156, 175, 184, 185, 189]. These findings provided strong evidence that the duration of the mitotic arrest is not identical for all cells, both across and within distinct cancer cell lines, in the presence of various antimitotic drugs such as nocodazole, Kinesin-5 (Eg5) inhibitors, monastrol, or taxol [148–151, 154, 155].

Even within identical types of cell cultures or drugs used, cells exhibit a considerable degree of heterogeneity in response to prolonged antimitotic drug exposure. For example, cells may either exit mitosis and remain in interphase for an indefinite period of time, undergo programmed cell death, (i.e., apoptosis) after exiting mitosis or interphase, or proceed through mitosis via multipolar spindle formation [148, 150–152, 154–156, 189]. In the case of multipolar spindle formation, cells divide into daughter cells by segregating their chromosomes in more than two different directions, dying during the second mitosis, or remaining in interphase for the duration of the experiments [152, 189, 190].

Motivated by these experimental findings, we introduce a *novel* mathematical modeling framework of OVCAR-8 cancer cell dynamics given drug exposure that incorporates an intrinsic form of heterogeneity in response to prolonged antimitotic drug exposure via the duration of times cells spend in the cell-cycle and apoptosis process. The system (4.1)-(4.3) is an age-structured physiologically motivated modeling framework for describing *in vitro* cancer cell growth dynamics given a drug that induces mitotic arrest, thus extending the average cell-cycle length.

To reflect the intrinsic cell heterogeneity, cells in the proliferative and in the apoptotic compartment are structured by the amount of time they spend in each phase. Herein, we considered a drug that extends the average cell-cycle length, and studied its impact on the long-term cancer cell growth dynamics and response to antimitotic drug exposure using two distinct antimitotic drug effects, i.e., a sustained, constant mitotic arrest and a switch-on/switch-off arrest, and three different levels of increase in the average cell-cycle lengths.

Our numerical simulations suggest that at confluence and in the absence of any drug, quiescence is the long-term asymptotic behaviour emerging from the cancer cell growth dynamics. Upon drug addition, the cancer cell dynamics significantly changes. Specifically, the prolonged mitotic arrest induced by the antimitotic drug results in a strong growth-inhibitory activity *in vitro* in a time-dependent manner.

In the presence of small increases in the average cell-cycle length, quiescence emerges as the long-term asymptotic behaviour resulting from the cancer cell growth dynamics. Our numerical simulations suggest that quiescence can emerge relatively quickly, and can thus constitute an intrinsic resistance mechanism to antimitotic drug exposure. The small increases in the average cell-cycle length result in a period of slowing-down of the cell-cycle from which cancer cells can recover and continue proliferating until reaching confluence.

From a therapeutic point of view, the presence of quiescent cancer cells has serious implications for chemotherapy regimens, which rely on active cell-cycling to target and kill proliferating cells. The long-term maintenance of a quiescent cancer cell population acts as a reservoir for proliferating cells, and can ultimately lead to cancer recurrence and shorter disease-free survival periods [125–127, 191, 192].

However, in the presence of intermediate increases in the average cell-cycle length, a sustained, constant mitotic arrest markedly decreases the total number of cancer cells present, and can drive the cell population to extinction. A switch-on/switch-off arrest maintains an active cell population in the long-term, with proliferative cell numbers exhibiting a steady oscillatory state, and quiescent cell numbers remaining relatively constant in time.

The transient behavior in the cancer cell growth dynamics signals the emergence and maintenance of a steady quiescent cell population, which in turn, represents a form of intrinsic, non-genetic resistance that results from variations in cell-cycle parameters [193, 194]. This can potentially decrease the efficacy of therapies that rely on active cell-cycling for their killing effects, such as traditional chemotherapies [195–197].

Moreover, given large increases in the average cell-cycle length induced by antimitotics, cells do not resume proliferation, and are driven to extinction by a sustained, constant mitotic arrest. Intriguingly, a switch-on/switch-off arrest may maintain an active cancer cell population in the long-term. This suggests that unless exposed to saturating drug concentrations for prolonged periods of time, cancer cells may not experience a mitotic arrest for long enough in order to trigger apoptosis, which may have therapeutic implications as clinical responses depends on apoptosis rates, and not exclusively on mitotic arrest [137, 189].

Additionally, the fate of cells following drug treatment also depends on the cell type. For instance, cell lines sensitive to mitotic cell death tend to reach the MOMP threshold before cyclin B1 levels reach the threshold required for cells to slip out of mitosis [148, 151, 152, 154, 156, 189]. Conversely, cell lines resistant to mitotic cell death tend to have a faster rate of cyclin B1 degradation and/or slow rate of intrinsic cell death activation [153, 155, 157, 177].

These molecular-based variations in sensitivity to apoptosis and mitotic arrest are likely to substantially contribute to the observed heterogeneity in cell responses, and potentially represent the crucial factor in determining cell fate in response to antimitotic drug exposure.

4.4.1 Conclusions

The fate of cells following drug treatment may depend on the drug concentrations and on the drug exposure times [148, 151, 152, 154, 156, 189]. The prolonged mitotic arrest induced by anti-mitotic drugs (i.e., an increased period of time spent in the cell-cycle) can lead to gradual accumulation of cell death signals that ultimately trigger apoptosis in cancer cell cultures [153, 155, 157, 177]. Investigating the role of intrinsic cell heterogeneity emerging from variations in cell-cycle parameters and apoptosis is thus a crucial step towards better informing drug administration in the treatment of ovarian cancer.

In this work, we investigated OVCAR-8 growth dynamics under the effect of a drug that extends the average cell-cycle length, and studied its impact on the long-term cancer cell growth dynamics and response to antimitotic drug exposure. We used two distinct antimitotic drug effects, i.e., a sustained, constant mitotic arrest and a switch-on/switch-off arrest, and three different levels of increase in the average cell-cycle lengths. Intrguingly, our results suggest that the transient behavior in the cancer cell growth dynamics signals the emergence and maintenance of a steady quiescent cell population, which in turn, represents a form of intrinsic, non-genetic resistance that results from variations in cell-cycle parameters [193, 194]. This can potentially decrease the efficacy of therapies for ovarian cancer that rely on active cell-cycling for their killing effects.

Chapter 5: Modeling Single Cell Heterogeneity in Response to Distinct Antimitotic Therapies

The results in this chapter were submitted for publication [60]. It focuses on a mathematical study of cell fate kinetics in response to prolonged exposure to antimitotic drugs *in vitro*.

5.1 Introduction to Cellular Heterogeneity in Response to Prolonged Antimitotics Exposure

Classic microtubule-targeting drugs such as taxanes and vinca alkaloids constitute a highly successful class of antimitotic drugs, with potent anti-tumor activity in many human solid tumors, including ovarian cancers [140,147,186,190]. In an effort to reduce the hematological and neuronal toxicity induced by these drugs and thus improve efficacy-to-toxicity ratios, newer antimitotic drugs such as spindle-targeting agents were recently developed.

However, these agents demonstrated limited anti-tumor activity in the clinic [198–206]. Despite their distinct primary targets, antimitotic drugs disrupt mitotic spindle assembly, activating the spindle assembly checkpoint (SAC), and leading to a prolonged mitotic arrest in 100% of the *in vitro* cells in the study irrespective of the antimitotic drug used [151].

Following prolonged mitotic arrest, cancer cells predominantly undergo one of two fates: death in mitosis via intrinsic apoptosis, or slippage out of mitotic arrest following the gradual proteolysis of cyclin B1 and subsequent survival in a G1 state [181, 207–209].

The proportion of cells that undergo each alternative fate and the timing of these events vary significantly between different drugs and cell types [137, 148, 149, 151, 154, 202, 207]. Even within identical types of cell cultures or drugs used, cells treated with antimitotics exhibit a considerable degree of heterogeneity in response to prolonged drug exposure [203, 208, 210]. Such observations have been reported in multiple single cell studies involving individual cancer cells in culture in the presence of various antimitotic drugs, including paclitaxel and Eg5 kinesin inhibitors.

Additionally, it has been experimentally demonstrated that even though the death in mitosis and mitotic slippage pathways are simultaneously active, they function independently of each other during mitotic arrest [149, 153, 157]. These studies confirmed Gascoigne and Taylor's proposed "competing pathways model", where the death in mitosis and mitotic slippage pathways are hypothesized to be competing against each other (i.e., the fastest process to execute in an individual cell wins) [151].

The first pathway consists of the activation of cell death pathways, where caspase-dependent cell death signals become stronger in time, simultaneously as cyclin B1 degrades [149–151, 155, 156, 158, 159, 181, 208, 210–213]. The second pathway involves cells that exit mitosis following a prolonged mitotic arrest, when cyclin B1 is slowly degraded and Cyclin-dependent kinase-1 (Cdk1) activity levels fall below the threshold needed to keep cells in mitosis and thus trigger mitotic exit, despite continued SAC signaling [156,158,184,185,190,208,211,214,215].

For example, in the case of Gascoigne and Taylors *in vitro* results on the colon carcinoma RKO cell line, the competing networks model would suggest that cell death signals in RKO cells accumulate faster than cyclin B1 levels degrade, though not at the same constant rate, as the different durations of mitotic arrest that RKO cells exhibit would suggest [151]. To the best of our knowledge, no such similar studies have been, to date, performed on human ovarian cancer cell lines.

Thus, we chose to focus on the experimental results of [151] in order to better understand the effects of antimitotic therapy (which is a primary treatment modality for ovarian cancer patients) on individual cancer cells.

The quantitative understanding of the cellular apoptosis and slippage rates and their dependency on the length of mitotic arrest is essential in order to decode and better understand the effect of the molecular mechanisms that govern cellular fate in response to antimitotic therapy. Furthermore, it remains to be elucidated whether any common features in the cellular responses to the different antimitotics characterizing each pathway exist both in cell culture studies and in the clinic [137, 186,190,216,217]

We propose a quantitative description of the kinetics of colon carcinoma RKO cells in response to the microtubule-targeting agents nocodazole and taxol, and the spindle-targeting Eg5 inhibitors AZ138 and monastrol. Our mathematical model is calibrated using the *in vitro* observations of [151], wherein time-lapse microscopy data demonstrated prolonged and variable durations of mitotic arrest in RKO cells prior to subsequent cell death or slippage.

Our aim is to provide a quantitative perspective on the kinetics behind the variability in RKO cell drug responses to distinct antimitotic drugs. We hypothesize that the death in mitosis and mitotic slippage pathways exhibit differential kinetic cellular apoptosis and slippage rates depending on the length of mitotic arrest.

Our mathematical model is the first study of its kind to provide the cellular apoptosis and slippage rates and their dependency on the length of mitotic arrest for the death in mitosis and mitotic slippage pathways in the RKO cell line. We demonstrate numerically that these rates increase with the duration of mitotic arrest.

Additionally, given that the cellular fate is known, the hazard rates are identical among the different antimitotic drugs. This result is based on a previously unrecognized fact emerging from our quantitative analysis, i.e., that the proportions of RKO cells that survive until time “a” in mitotic arrest and subsequently undergo death in mitosis and mitotic slippage are identical when cells are exposed to non-taxol drugs. Moreover, we demonstrate that RKO cells display a higher hazard of undergoing death in mitosis than mitotic slippage throughout the 72-hour experimental time-course.

Overall, our results indicate that RKO cells exhibit a triphasic response curve irrespective of cell fate or antimitotic drug. Interestingly, our quantitative analysis suggests that the taxol-treated RKO cells display the slowest cell death in mitosis responses across all antimitotic drugs. Despite taxol being the slowest inducer of cell death in mitosis in the RKO cell line as evidenced by its specific hazard function, it turns out that its slow induction of cell death is not a good measure for predicting its likelihood to induce death in mitosis, as 98% of RKO cells exposed to taxol do undergo death in mitosis following a prolonged mitotic arrest. Further investigations are needed to establish whether this is a concentration-dependent effect.

Based on these results, we formulate hypotheses on the dynamics behind the death in mitosis and mitotic slippage pathways in RKO cells. These could potentially expand our understanding of the mechanisms which dictate whether a cell dies or survives a prolonged mitotic arrest, if tested in more focused experiments.

5.1.1 Model Findings

Both classic and newer antimitotics commonly induce a prolonged mitotic arrest in cell culture. As first hypothesized and demonstrated by [151], during mitotic arrest, cells predominantly undergo one of two fates governed by alternative pathways: cell death by apoptosis, or mitotic slippage and survival. To go beyond this binary description, a better quantitative understanding of these cell responses is needed.

In this chapter, we propose a quantitative description of the kinetics of colon carcinoma RKO cell fates in response to the microtubule-targeting agents nocodazole and taxol, and the spindle-targeting Eg5 inhibitors AZ138 and monastrol. The mathematical model is calibrated using the *in vitro* experiments of [151]. Therein, time-lapse microscopy data demonstrated long and variable durations of mitotic arrest in RKO cells prior to subsequent cell death or slippage.

We show that the time-dependent probability cells die in mitosis or slip is identical for nocodazole, AZ138, and monastrol but significantly different for taxol. Cell death and slippage responses across drugs can be characterized by Gamma distributions. We subsequently quantify the hazard rates corresponding to the RKO cells undergoing death in mitosis and slippage. We demonstrate numerically that these rates increase with prolonged mitotic arrest.

Additionally, given that the cellular fate is known, the hazard rates are identical among the different antimitotic drugs. We also demonstrate that RKO cells display a higher hazard of undergoing death in mitosis than mitotic slippage throughout the 72-hour experimental time-course. Our model demonstrates that RKO cells exhibit a triphasic response -first, remain in mitosis, then undergo fast and slow transition, respectively- dependent on the length of mitotic arrest and irrespective of cell fate or drug.

This study provides a novel, quantitative perspective on the kinetics behind the variability in RKO cell drug responses to distinct antimitotic drugs. It represents the first study of its kind to provide the RKO cellular apoptosis and slippage rates and their dependency on the length of mitotic arrest.

5.2 Modeling Approach

5.2.1 Data and Modeling Calibration

In [151], RKO cells in culture were continuously incubated with 0.03 µM AZ138, 0.03 µM AZ138, 100 µM monastrol, 30 ng/mL nocodazole, and 0.1 µM taxol during a 72-hour imaging period (Figures 5.1(a) - 5.1(e), respectively).

We note that these drug concentrations represent equivalent, minimal saturating dosages of antimitotics required to ensure the efficient induction of mitotic arrest and a maximal induction of a 4N DNA peak, as analyzed by flow cytometry and reported in Figure S4B in [151].

Figure 5.1 illustrates cellular fates in response to the prolonged drug exposure. Specifically, cells can either: (i) successfully divide (black bars), (ii) undergo mitotic slippage and remain in interphase throughout the duration of the experiment (blue bars), (iii) die in mitosis (red bars), (iv) undergo division, remain in interphase, then enter a second mitosis from which they slip and remain in interphase throughout the duration of the experiment (black, grey, and blue bars), (v) undergo mitotic slippage then die in interphase (blue and green bars); or (vi) die in interphase without having entered mitosis (green bars).

The times spent in mitosis (Figure S5A and C in [151], red bars), or in mitosis following drug addition and before slippage (Figure S5A and C in [151], blue bars) were subsequently recorded. Therein, “0 min” on the x-axis of the cell fate profiles observed in Figures S5A and C in [151] represents the time when cells entered mitosis

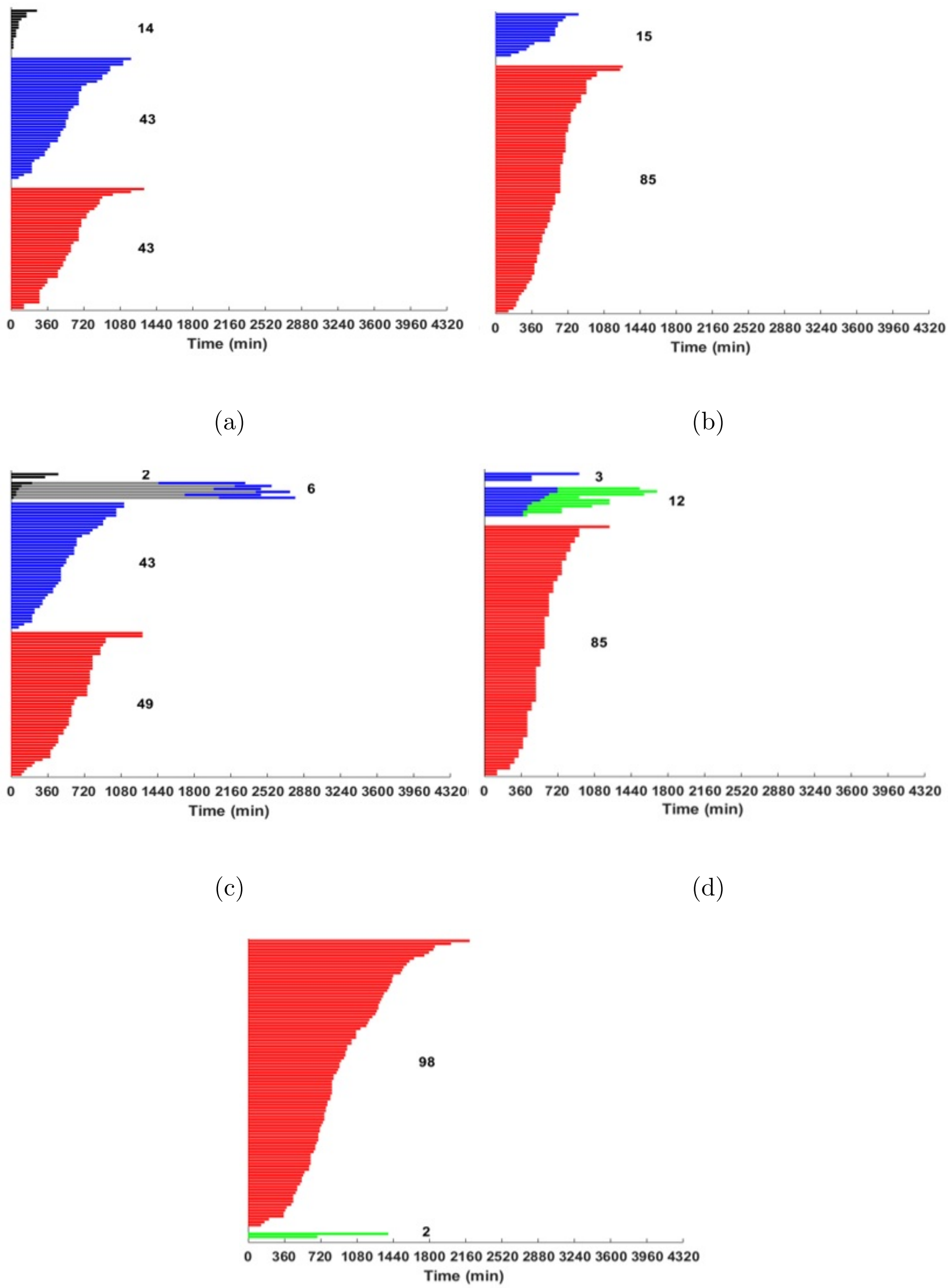

(a)

(b)

(c)

(d)

(e)

Figure 5.1: RKO cell response to (a) 0.03 µM AZ138, (b) 0.03 µM AZ138, (c) 100 µM monastrol, (d) 30 ng/mL nocodazole, and (e) 0.1 µM taxol during a 72-hour imaging period. Each horizontal bar represents the fate of a single RKO cell. For each panel (a)-(e), 100 distinct cell responses are represented.The number of cells corresponding to each category is shown in bold black.

(K. Gascoigne, personal communication).

In [151], data were pooled from recordings performed on individual cells synchronized in early S phase, using a thymidine block. Thymidine was added for 16 hours, before cells were released from the block. Drug medium was subsequently added 4.5 hours later. Imaging using automated time-lapse light microscopy was started at the same time. Images of RKO cells were then collected every 5 minutes for a total duration of 4320 minutes, equivalent to 72 hours (see Figure 1A in [151] for a timeline of the setup). Therein, mitosis was defined as the cellular state between nuclear envelope breakdown and the onset of anaphase (Figure S1 in [151]).

In these experimental findings, fewer than 5% of the total number of RKO cells were reported to have successfully completed mitosis and divided into daughter cells in response to the microtubule-targeting agents nocodazole and taxol, and the spindle-targeting Eg5 inhibitors AZ138 and monastrol (see Figure 5.1 for representative RKO cell responses). We note that in the absence of any antimitotic drugs, unsynchronized RKO cells are observed to undergo approximately three mitoses during a 72-hour imaging period [156].

Additionally, since in the experimental setup, the cells were spatially separated, the quantitative live-cell imagining technique employed by [151] reported individual cell behavior, independent of spatial or global density considerations. As a result, we did not consider an explicit cellular density or a spatial component in our mathematical model. Subsequent results reported below are based on the data reported in Figure 5.1.

5.2.2 Statistical Tests

We chose to focus on the predominant fates experienced by the RKO cells under prolonged antimitotic drug exposure, i.e., the fates governed by the death in mitosis and mitotic slippage pathways. To determine any statistically significant differences between the different RKO cell responses under prolonged exposure to the specific antimitotic drugs reported above, we first use the non-parametric Kruskal-Wallis test (or one-way ANOVA test for ranks) for $n = 5$ independent samples [218].

These samples correspond to the five RKO populations that undergo death in mitosis following exposure for a 72-hour period to 0.03 µM AZ138, 1 µM AZ138, 100 µM monastrol, 30 ng/mL nocodazole, and 0.1 µM taxol, respectively. We note that this test indicates whether the samples tested originate from the same distribution and identifies whether at least one of these samples is statistically significant (i.e., stochastically dominates). It does not, however, indicate in which sample(s) this dominance occurs.

We then performed pairwise non-parametric Mann-Whitney tests using all possible combinations between the groups of cells that died in mitosis (red bars) or that underwent mitotic slippage (blue bars); n.s., non-significant, $^{*}p < 0.05$, $^{**}p < 0.01$, $^{***}p < 0.005$ [219]. We note that this test is a non-parametric test that assesses whether two independent samples have similarly ranked distributions. It does not require the assumption of normal distributions.

5.2.3 Distribution of Times Spent in Mitotic Arrest before Dying or Slipping out of Mitosis

We use the experimental data to obtain the empirical CDF for the times spent in mitotic arrest corresponding to the death in mitosis and mitotic slippage pathways (illustrated in Figure 5.2). This is done by fitting a kernel smoothing function estimate to the CDF describing the duration of mitotic arrest corresponding to each drug, describing the duration of mitotic arrest reported in Figure S5A-B in [151]. The procedure is performed using MATLAB's "ksdensity" function.

This function returns a cumulative density function, based on the sampled data. The amount of time a cell spends in mitotic arrest is thus assumed to be a continuous variable. The empirical CDF corresponding to each drug obtained using the kernel smoothing procedure is illustrated for cells that die in mitosis or slip out of mitosis in Figures 5.2(b) and 5.2(c), respectively.

Data are adapted from the experimental findings reported in Figure S5A in [151]. Therein, the RKO cellular fate following prolonged exposure to four different drugs (monastrol, nocodazole, taxol and AZ138) was measured, based on the duration of drug-induced mitotic arrest. Cell death or slippage responses across drugs can be characterized by the cell-cycle age "a"-dependent Gamma distribution $\Gamma(a; k, \theta)$, with shape parameter k and scale parameter θ.

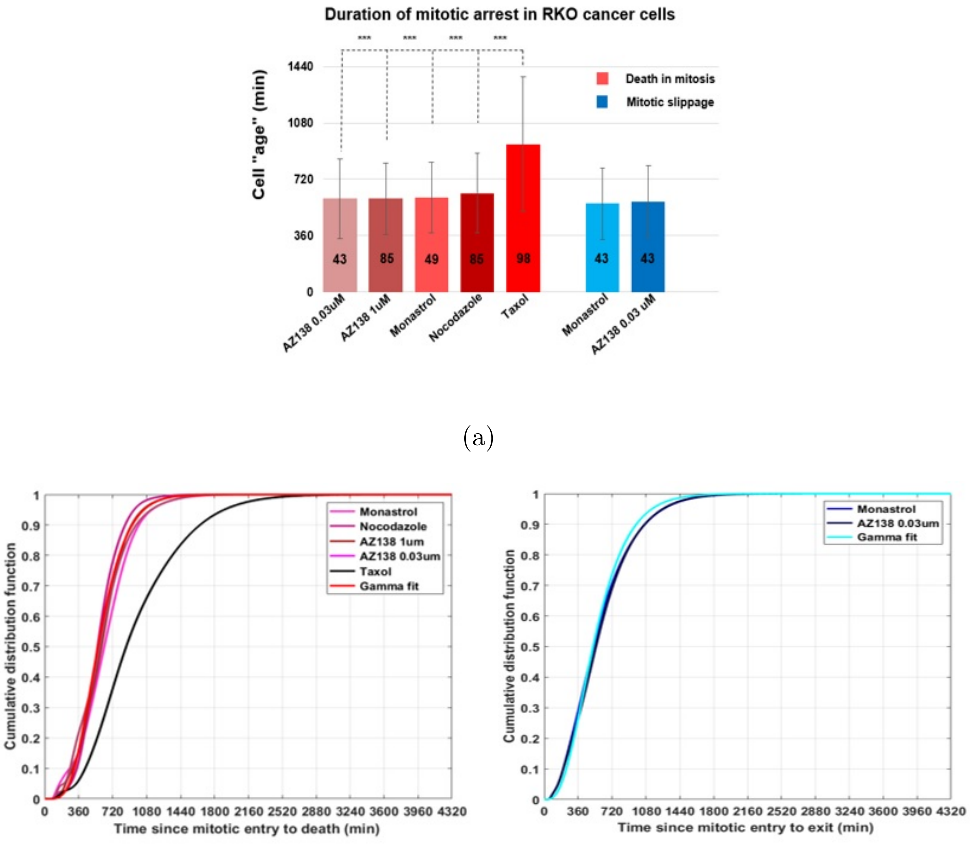

(a)

(b)

(c)

Figure 5.2: (a) Statistical differences between the different RKO cell responses under prolonged exposure to a specific antimitotic drug were analyzed using the non-parametric Mann-Whitney test; n.s., non-significant, $*p < 0.05$, $**p < 0.01$, $***p < 0.001$. Pairwise comparisons were performed among all possible combinations between the groups of cells that died in mitosis (red bars) or that underwent mitotic slippage (blue bars). The vertical bar plots represents the mean ± s.d. duration of the drug-induced mitotic arrest in either death in mitosis (red bars) or mitotic slippage (blue bars). The reported values are in minutes. The number of cells corresponding to each category is shown in bold black inside each vertical bar plot. The cumulative distribution functions (CDF) for (c) death in mitosis and (c) mitotic slippage show the fraction of RKO cells that either died or slipped after entering mitosis as a function of time.

5.2.4 Polynomial Fitting

To quantify the transition rates from mitotic arrest to cell death or interphase, we perform a polynomial least-squares fitting to the empirical transition rate derived from the Gamma CDF representing the fraction of RKO cells that either died or slipped after entering mitosis.

The fitting procedure is done using MATLAB's "polyfit", "polyval" and "polyfix" functions [220]. The first function returns the coefficients for a polynomial of a user-specified degree, that represents the best fit in the least squares sense for the input data. The second is used to evaluate the fitted polynomials on a prescribed set of gridpoints.

It also obtains error estimates in the Root-Mean-Square-Error (RMSE) sense between the approximate and fitted transitions rates from mitotic arrest to death in mitosis and mitotic slippage. The third function computes the coefficients for a polynomial of a user-specified degree, that represents the best fit in the least squares sense for the input data, with the added constraint that the polynomial must pass through a user-specified value at a specific point [220].

To best describe the corresponding transition rates from mitosis to death in mitosis for the non-taxol and taxol drugs, as well as the transition rate from mitosis to mitotic slippage, we chose to fit piecewise linear polynomials to the empirical data. Using linear polynomials, as opposed to higher-degree polynomials, enables us to easily interpret the modeling results into biologically meaningful observations that could be further tested with more focused experiments.

5.2.5 Modeling Approach

To study the emerging heterogeneity in RKO cell responses to prolonged antimitotic drug exposure, we model the dynamics of the RKO cancer cell population as the following system:

$$\frac{d}{da}\mathbf{M}(a) = \begin{bmatrix} \alpha_{MA}(a) & 0 \\ 0 & \alpha_{MI}(a) \end{bmatrix} \mathbf{M}(a), \tag{5.1}$$

with initial conditions:

$$\mathbf{M}(0) = \begin{bmatrix} p \\ 1-p \end{bmatrix} \mathbf{M}(a). \tag{5.2}$$

Herein, the mitotic compartment $\mathbf{M}$(a) is structured by the amount of time "a" cells spend in mitosis before dying, or slipping out of mitosis into interphase. The rate of change of $\mathbf{M}$(a) with respect to the experimental time course "a" (i.e., cell-cycle age) is represented by $\frac{d}{da}$. The derivative $\frac{d}{da}\mathbf{M}(a)$ implies that mitotic cells advance in cell-cycle age as time progresses.

From mitotic arrest, cells transition with time-dependent rate $\alpha_{MA}(a)$ and probability p to intrinsic cell death (i.e., apoptosis) or slip out of mitosis into interphase with time-dependent rate $\alpha_{MI}(a)$ and probability $1-p$.

In doing so, we implicitly assume that the death in mitosis and mitotic slippage pathways are simultaneously active, but function independently of each other during mitotic arrest (i.e., their outcomes are mutually exclusive). This assumption is supported experimentally by various cancer cell studies [186], and numerically by predictive modeling in [149]. Additionally, we assume that the amount of time "a" cells spend in mitotic arrest can be represented as a continuous variable.

The total number of RKO cells exposed to 0.03 µM AZ138, 1 µM AZ138, 100 µM monastrol, 30 ng/mL nocodazole, and 0.1 µM taxol that undergo either death in mitosis or mitotic slippage, as depicted in Figure 1A-E, is $\mathbf{M}_{total} = 86, 85, 92, 85, 98$, respectively. Thus, the initial number of RKO cells arrested in mitosis, corresponding to each drug and cell fate, as evidenced in Figure 5.2 is:

$$\mathbf{M}(0)_{0.03\,\mu\mathrm{M}\ AZ138} = \begin{bmatrix} 43 \\ 43 \end{bmatrix}, \ \mathbf{M}(0)_{1\,\mu\mathrm{M}\ AZ138} = \begin{bmatrix} 85 \\ 0 \end{bmatrix}, \mathbf{M}(0)_{100\,\mu\mathrm{M}\ monastrol} = \begin{bmatrix} 49 \\ 43 \end{bmatrix},$$

$$\mathbf{M}(0)_{30\ ng/mL\ nocodazole} = \begin{bmatrix} 85 \\ 0 \end{bmatrix}, \mathbf{M}(0)_{0.1\,\mu\mathrm{M}\ taxol} = \begin{bmatrix} 98 \\ 0 \end{bmatrix}. \tag{5.3}$$

Thus, Equation (5.2.5) yields a drug-dependent probability p of undergoing death in mitosis following mitotic arrest of $\frac{1}{2}$, 1, $\frac{49}{92}$, 1, and 1 in the case of 0.03 µM AZ138, 1 µM AZ138, monastrol, nocodazole, and taxol, respectively. The solution of the linear system (5.1) - (5.2) is:

$$\mathbf{M}(a) = \begin{bmatrix} p\mathrm{e}^{-\int_0^a \alpha_{MA}(a')da'} \\ (1-p)\mathrm{e}^{-\int_0^a \alpha_{MI}(a')da'} \end{bmatrix} \mathbf{M}_{total}. \tag{5.4}$$

In order to determine the hazard functions corresponding to the RKO cells undergoing death in mitosis and slippage, we estimate the proportion of RKO cells that survive until time "a" in mitotic arrest and subsequently undergo death in mitosis or mitotic slippage as the exponentially decaying process:

$$\mathbf{M}(a) = \begin{bmatrix} \mathrm{e}^{-\int_0^a \alpha_{MA}(a')da'} \\ \mathrm{e}^{-\int_0^a \alpha_{MI}(a')da'} \end{bmatrix} \sim \overline{\mathbf{F}(a)} = \begin{bmatrix} 1 - F_{MA}(a;k,\theta) \\ 1 - F_{MI}(a;k,\theta) \end{bmatrix}, \tag{5.5}$$

where the cell death or slippage responses across drugs are characterized by the cell-cycle age "a"-dependent Gamma CDF $F_{MA}(a;k,\theta)$ or $F_{MI}(a;k,\theta)$, corresponding to the death in mitosis and mitotic slippage pathways, respectively. Here, the notation "$\sim$" represents "is distributed as".

Each Gamma CDF models the fraction of RKO cells that either die or slip after entering mitosis as a function of time, and is characterized by its corresponding shape k and scale parameters θ (see Figures 5.2(b) and 5.2(c) for the quantification). Herein, $\overline{\mathbf{F(a)}}$ denotes the vector of survival functions corresponding to each pathway, where the survival function is defined as 1 - CDF.

To determine $\alpha_{MA}(a)$ and $\alpha_{MI}(a)$, we obtain from Equation (5.5):

$$\mathbf{M}(a) = \begin{bmatrix} \int_0^a \alpha_{MA}(a')da' \\ \\ \int_0^a \alpha_{MI}(a')da' \end{bmatrix} \approx \begin{bmatrix} -\ln[1 - F_{MA}(a;k,\theta)] \\ \\ -\ln[1 - F_{MI}(a;k,\theta)] \end{bmatrix}. \tag{5.6}$$

Taking the discrete derivative of Equation (5.6) yields:

$$\mathbf{M}(a) = \begin{bmatrix} \frac{\int_0^{a+\Delta a} \alpha_{MA}(a')da' - \int_0^a \alpha_{MA}(a')da'}{\Delta a} \\ \\ \frac{\int_0^{a+\Delta a} \alpha_{MI}(a')da' - \int_0^a \alpha_{MI}(a')da'}{\Delta a} \end{bmatrix} \approx \begin{bmatrix} \alpha_{MA}(a) \\ \\ \alpha_{MI}(a) \end{bmatrix} \approx \begin{bmatrix} \frac{f_{MA}(a;k,\theta)}{1-F_{MA}(a;k,\theta)} \\ \\ \frac{f_{MI}(a;k,\theta)}{1-F_{MI}(a;k,\theta)} \end{bmatrix}, \tag{5.7}$$

where "Δa" represents the discrete time-step, which is set in our numerical simulations to one minute. We note that the right-hand side of Equation (5.7) is equal to $\begin{bmatrix} \frac{d}{da}\ln[1 - F_{MA}(a;k,\theta)] \\ \\ \frac{d}{da}\ln[1 - F_{MI}(a;k,\theta)] \end{bmatrix}$, with $f_{MA}(a;k,\theta)$ and $f_{MI}(a;k,\theta)$ representing the Gamma probability distribution functions corresponding to the fraction of RKO cells that either died or slipped after entering mitosis as a function of time "a", respectively.

5.3 Numerical Results

5.3.1 The Time-dependent Probability Cells Die in Mitosis or Slip Is Identical for All Drugs Except for Taxol

To determine whether the type of antimitotic drug used affects the duration of mitotic arrest in RKO cells, we compare the variable durations of mitotic arrest illustrated in Figure 5.1 corresponding to cells that either died in mitosis or exited mitosis and returned to interphase.

We first analyze the statistical differences between the different RKO cell responses under prolonged exposure to a specific antimitotic drug using the non-parametric Kruskal-Wallis test for $n = 5$ independent samples. These correspond to the five RKO populations that undergo death in mitosis following exposure for a 72-hour period to 0.03 µM AZ138, 1 µM AZ138, 100 µM monastrol, 30 ng/mL nocodazole, and 0.1 µM taxol, respectively. The observed aggregate difference among the five samples was significant beyond the $<$ 0.0001 significance level (data not shown).

We then performed pairwise non-parametric Mann-Whitney tests using all possible combinations between the groups of cells that died in mitosis (red bars) or that underwent mitotic slippage (blue bars); n.s., non-significant, $*p < 0.05$, $**p < 0.01$, $***p < 0.005$.

RKO cells exposed to taxol exhibit a markedly distinct response to the prolonged taxol exposure, i.e., the duration of mitotic arrest induced by taxol in RKO

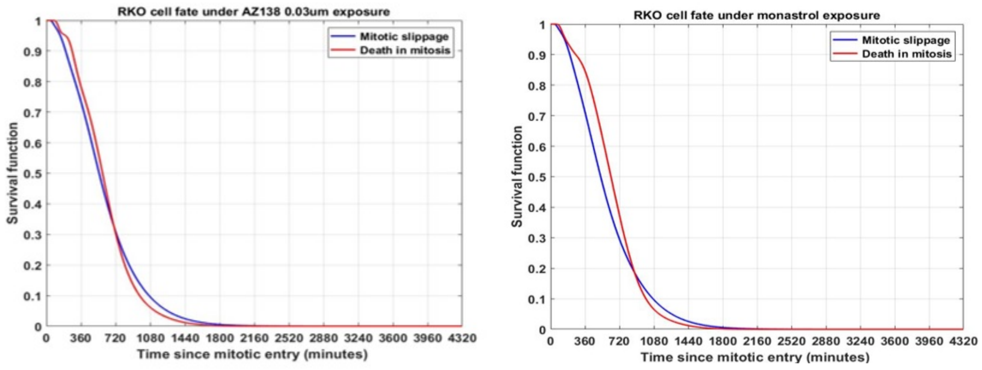

(a) (b)

Figure 5.3: Under prolonged (a) 0.03 µM AZ138 and (b) 100 µM monastrol exposure, RKO cells are more likely to undergo mitotic slippage (blue lines) rather than death in mitosis (red lines) for a shorter duration of mitotic arrest, i.e., 11.73 and 14.65 hours, respectively.

cells is significantly different compared to the durations of the arrest induced by nocodazole, monastrol, or AZ138. This effect achieves statistical significance beyond the < 0.001 level (Figure 5.2(a)).

5.3.2 Cell Death and Slippage Responses Across Drugs Can Be Characterized by Gamma Distributions

As indicated by our statistical analysis, the time-dependent probability cells undergo death in mitosis or mitotic slippage is identical for all drugs except for taxol. To best describe the duration of mitotic arrest cells experience before dying in mitosis or slipping from mitosis and returning to interphase, we chose to represent the RKO cell death or slippage responses across drugs by corresponding Gamma distributions $\Gamma(a; k, \theta)$.

Each distribution represents the fraction of RKO cells that either died or slipped after entering mitosis as a function of time (i.e., cell-cycle age “a”), is characterized by its corresponding shape k and scale parameters θ, as illustrated in Figures 5.2(b) and 5.2(c). The choice of the Gamma distribution to model the duration of mitotic arrest is motivated by this distribution’s asymmetry and right-skewness, and is confirmed by the excellent fit to the empirical data.

Specifically, in Figure 5.2(b) the death in mitosis CDF for the non-taxol drugs can be represented by $\Gamma(5.91, 101.15)$, with 95% confidence intervals [5, 6.98] and [85, 120.36] for k and θ, respectively. The RMSE between the empirical CDF (i.e., based on the sampled data and obtained by using MATLAB’s “ksdensity” function) and the Gamma fit is equal to $1.1 \cdot 10^{-2}$.

Similarly, the death in mitosis CDF for taxol can be represented by $\Gamma(4.43, 212.9)$, with 95% confidence intervals [3.38, 5.8] and [159.9, 283.5] for k and θ, respectively. The RMSE between the empirical CDF and the Gamma fit is equal to $1.23 \cdot 10^{-2}$. In Figure 5.2(c), the mitotic slippage CDF can be represented by $\Gamma(3.55, 161)$, with 95% confidence intervals [2.66, 4.72] and [118.4, 218.8] for k and θ, respectively. The RMSE between the empirical CDF and the Gamma fit is equal to $1.2 \cdot 10^{-2}$.

We note that using the Gamma CDF instead of the empirical CDF obtained by using MATLAB’s “ksdensity” function enables us in subsequent simulations to obtain a closed-form expression for the age-dependent transition rates from mitosis to death in mitosis and mitotic slippage, i.e., $\alpha_{MA}(a)$ and $\alpha_{MI}(a)$, respectively, as demonstrated in Equations (5.5) - (5.7).

5.3.3 RKO Cells Are More Likely to Slip in Interphase for Shorter Durations of Mitotic Arrest, and Die in Mitosis for Longer Durations of Mitotic Arrest

Under prolonged 0.03 µM AZ138, and 100 µM monastrol exposure, RKO cells are more likely to undergo mitotic slippage (blue lines in Figures 5.4(a) and 5.4(b)) rather than death in mitosis (red lines in Figures 5.4(a) and 5.4(b)) for a shorter duration of mitotic arrest, i.e., 11.73 and 14.65 hours, respectively. However, for durations longer than 11.73 and 14.65 hours of mitotic arrest in RKO cells exposed to 0.03 µM AZ138 and 100 µM monastrol, respectively, cells are more likely to undergo death in mitosis rather than mitotic slippage.

5.3.4 RKO Cells Exhibit a Triphasic Response Curve Irrespective of Cell Fate or Antimitotic Drug

From mitotic arrest, cells undergo death in mitosis (i.e., apoptosis) with probability p and age-dependent transition rate $\alpha_{MA}(a)$. Alternatively, they can undergo mitotic slippage and return to interphase with probability $1 - p$ and age-dependent transition rate $\alpha_{MI}(a)$, as shown in Equation (5.1). We note that these functions increase with prolonged mitotic arrest, irrespective of cell fate or antimitotic drug, see Figure 5.4.

We subsequently fit piecewise linear polynomials to the transition rates from mitosis to apoptosis, $\alpha_{MA}(a)$, for the non-taxol and taxol drugs, as illustrated in

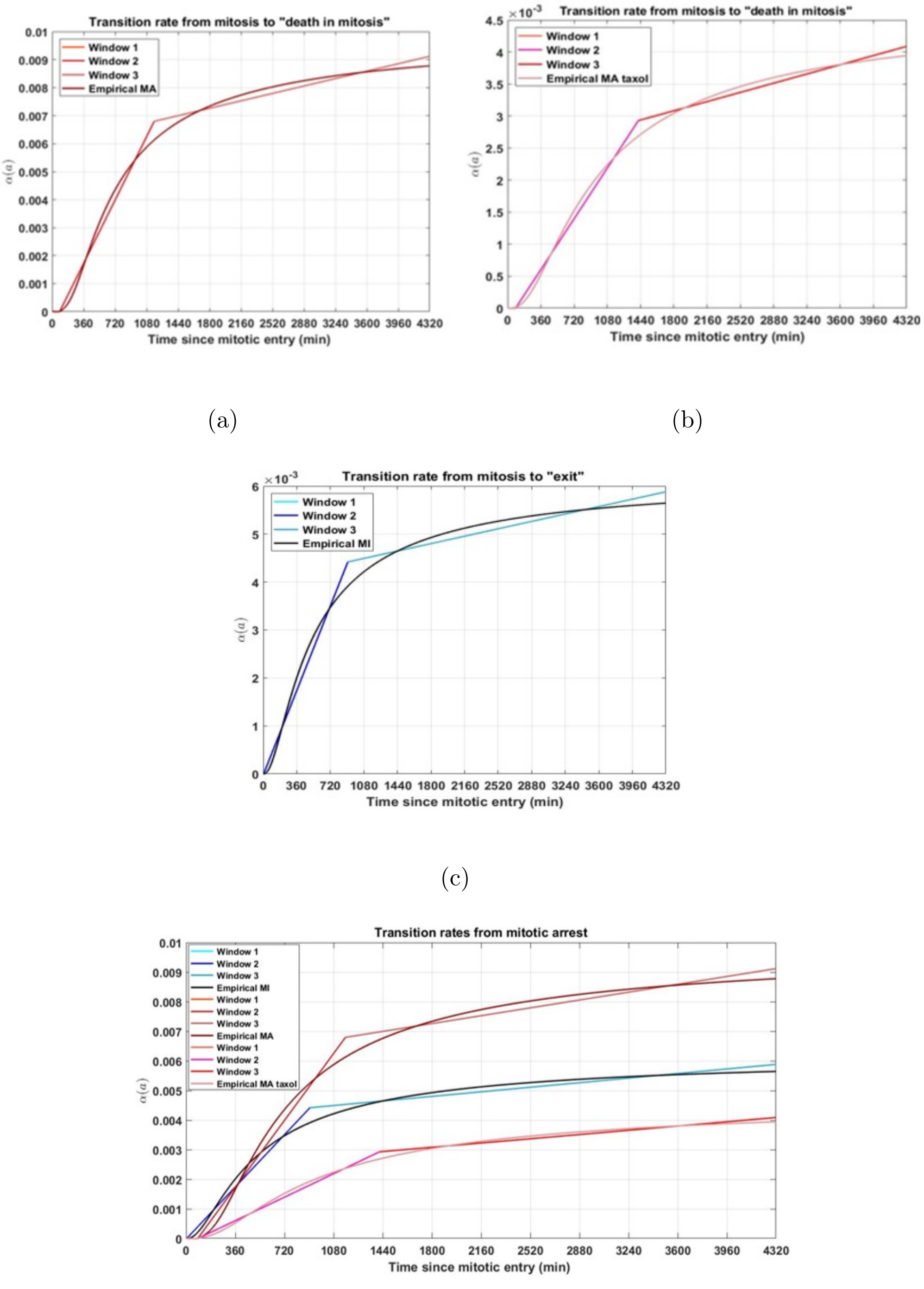

(a) (b)

(c)

(d)

Figure 5.4: The hazard functions corresponding to the RKO cells undergoing death in mitosis for (a) non-taxol drugs and (b) taxol and to the RKO cells undergoing mitotic slippage (c) increase monotonically with time, i.e., the duration of mitotic arrest.

Figures 5.4(a) and 5.4(b), respectively (red bars), and from mitosis to slippage into interphase, as illustrated in Figure 5.4(c) (blue bars).

Each labeled "Window" in the Figure 5.4 legends corresponds to time period during the mitotic arrest RKO cells undergo one of the following: (i) remain in mitotic arrest with probability 1 ("Window 1" in Figures 5.4(a) - 5.4(d), respectively), (ii) fast transition from mitotic arrest to cell death in mitosis, or mitotic slippage ("Window 2" in Figures 5.4(a) - 5.4(d), respectively), or (iii) slow transition from mitotic arrest to cell death in mitosis, or mitotic slippage ("Window 3" in Figures 5.4(a) - 5.4(d), respectively).

The hazard functions $\alpha_{MA}(a)$ and $\alpha_{MI}(a)$, corresponding to the death in mitosis induced by non-taxol drugs, taxol (red lines) and mitotic slippage (blue lines), derived empirically from solving Equation (5.7) are illustrated as the non-linear functions in Figures 5.4(a) - 5.4(c), respectively. In Figure 5.4(d), the distinct hazard functions corresponding to the death in mitosis responses induced by the non-taxol drug, taxol, and mitotic slippage responses are plotted, in order to better visualize and compare RKO cell fate responses across drugs.

The piecewise linear polynomials that best describe the hazard functions corresponding to the death in mitosis and mitotic slippage cell responses are reported below.

$$\alpha_{MA}(a) = \begin{cases} 0, & \text{for } 0' \leq a \leq 82', \\ 6.28 \cdot 10^{-6} a - 1.96 \cdot 10^{-5}, & \text{for } 82' \leq a \leq 1164', \\ 7.36 \cdot 10^{-7} a + 4 \cdot 10^{-3}, & \text{for } 1164' \leq a \leq 4320'. \end{cases} \tag{5.8}$$

$$\alpha_{MA}(a) = \begin{cases} 0, & \text{for } 0' \leq a \leq 86', \\ 2.2 \cdot 10^{-6}a - 1.89 \cdot 10^{-4}, & \text{for } 86' \leq a \leq 1416', \\ 3.99 \cdot 10^{-7}a + 2.4 \cdot 10^{-3}, & \text{for } 1416' \leq a \leq 4320'. \end{cases} \tag{5.9}$$

$$\alpha_{MI}(a) = \begin{cases} 0, & \text{for } 0' \leq a \leq 4', \\ 4.89 \cdot 10^{-6}a - \cdot 10^{-4}, & \text{for } 4' \leq a \leq 907', \\ 4.29 \cdot 10^{-7}a + 4 \cdot 10^{-3}, & \text{for } 907' \leq a \leq 4320'. \end{cases} \tag{5.10}$$

The RMSE values between the empirically-derived and fitted $\alpha_{MA}(a)$ and $\alpha_{MI}(a)$ corresponding to the death in mitosis induced by non-taxol drugs, induced by taxol, and to mitotic slippage, respectively are $3.27 \cdot 10^{-4}$, $1.25 \cdot 10^{-4}$, and $2.34 \cdot 10^{-4}$, respectively. The fitted polynomials are illustrated in Figures 5.4(a) - 5.4(c), respectively.

Overall, RKO cells display a higher hazard of undergoing death in mitosis than mitotic slippage throughout the 72-hour experimental time-course (top red and blue lines in Figure 5.4(d)). Moreover, the transition from mitotic arrest to cell death in mitosis for the non-taxol drugs ("Windows 2-3" in Figure 5.4(a)) is overall faster than the transition from mitotic arrest to mitotic slippage ("Windows 2-3" in Figure 5.4(c)), with a 1.3 - 1.7-fold difference in the slopes of the piecewise linear polynomials corresponding to the two alternative pathways.

We additionally note that the taxol-treated RKO cells display the slowest cell death in mitosis responses across all antimitotic drugs (Figure 5.4(b)), as evidenced by 1.8 - 2.8-fold difference in the slopes of the piecewise linear polynomials corresponding to the non-taxol drugs and taxol, illustrated in Figure 5.4(d).

Interestingly, despite taxol being the slowest inducer of cell death in mitosis in the RKO cell line as evidenced by its specific hazard function (illustrated in Figure 5.4(d)), this observation is not a good measure for predicting its likelihood to induce death in mitosis, as 98% of RKO cells exposed to taxol do undergo death in mitosis following a prolonged mitotic arrest (see Figure 5.1(e) herein and Figure S5A in [151]). However, this effect might be dose-dependent, as in [151], RKO cells were only exposed to 0/1 µM taxol during a 72-hour imaging period.

5.4 Discussion of Modeling Results

The mechanisms behind drug-induced prolonged mitotic arrest and cancer cell death using different antimitotic drugs have only recently begun to be elucidated using live quantitative cell imaging [148, 149, 151, 154, 213].

Using live quantitative single cell imaging, several studies have demonstrated that individual cancer cells display widely varying responses to antimitotic drugs. These studies have expanded our understanding of the mechanisms which determine whether a cell dies in mitosis or survives a prolonged mitotic arrest by returning to interphase following exposure to antimitotics.

For example, in [151], the authors proposed a model where the two predominant cancer cell fates, i.e., mitotic slippage and death in mitosis, are governed by two independent networks. The first network involves the cell-cycle regulator cyclin B1 and its kinase partner Cdk1 as follows: an active anaphase promoting complex APC/C, an E3 ubiquitin ligase, targets cyclin B1 for proteasome degradation past the threshold necessary to maintain sufficient Cdk1 activity and promotes mitotic exit.

Cells thus escape mitotic arrest without completing mitosis, which can lead to tetraploidy, senescence, or apoptosis following a subsequent mitosis [137, 189, 221]. The second network involves caspase activation and signal accumulation during mitotic arrest, the destabilization of the survivin/XIAP complex, and alterations in the intracellular localization and activation status of Bcl-2 family members [203,215].

Several major questions regarding cancer cell fate and cell response to prolonged antimitotic therapies remain unresolved: (1) Does duration of mitotic arrest predict cell fate? (2) What are the cellular apoptosis and slippage rates corresponding to the death in mitosis and mitotic slippage? (3) Are these rates dependent on the length of mitotic arrest? and finally (4) Do any universal features in the cellular responses to the different antimitotics characterizing each pathway exist? [150, 151, 156, 211, 222–224].

In this paper, we provide for the first time the cellular apoptosis and slippage rates and their dependency on the length of mitotic arrest for the death in mitosis and mitotic slippage pathways in the RKO cell line.

We demonstrate numerically that these rates increase with the duration of mitotic arrest. Given the cellular fate is known, they are identical among the distinct non-taxol antimitotic drugs whose effect on RKO cell fate was investigated in [151]. Importantly, this is a previously unrecognized fact which emerges from our quantitative analysis, i.e., that the proportions of RKO cells that survive until time “a” in mitotic arrest and subsequently undergo death in mitosis and mitotic slippage are identical when cells are exposed to non-taxol drugs.

Moreover, we demonstrate that RKO cells display a higher hazard of undergoing death in mitosis than mitotic slippage throughout the 72-hour experimental time-course. Additionally, our results indicate that RKO cells exhibit a triphasic response curve irrespective of cell fate or antimitotic drug. Interestingly, taxol induces the slowest cell death in mitosis responses across all antimitotic drugs in RKO cells.

However, its slow induction of cell death is not a good measure for predicting its likelihood to induce death in mitosis, as experimentally, almost all RKO cells exposed to taxol do undergo death in mitosis following a prolonged mitotic arrest, as reported in [151, 207].

We now briefly comment upon several aspect emerging from our quantitative modeling results. First, it is intriguing that RKO cells exposed to the microtubule-destabilizing nocodazole, and Eg5-kinesin inhibitors AZ138 and monastrol exhibit similar responses to prolonged antimitotic exposure. To the best of our knowledge, this is a previously unrecognized fact. Our statistical analysis indicates that the duration of mitotic arrest induced by these drugs is not statistically different between these drugs, as both cells that die in mitosis or exit mitosis and slip into interphase display the same CDFs, respectively.

While death in mitosis and slippage kinetics are highly variable from cell to cell, our results suggests that the microtubule-destabilizing nocodazole and Eg5-kinesin inhibitors AZ138 and monastrol induce the same duration of mitotic arrest in RKO cells corresponding to each pathway, despite the different drug targets and pharmacokinetics. This highlights a potential functional convergence between the different non-taxol antimitotic drugs used in the study with respect to inducing similar distributions of times spent in mitotic arrest before dying or slipping out of mitosis. This intriguing observation merits further experimental investigation.

However, this effect might be dose-dependent, as in [151], RKO cells were only exposed to specific antimitotic drug concentrations (i.e., 0.03 μM AZ138, 1 μM AZ138, 100 μM monastrol, 30 ng/mL nocodazole, and 0.1 μM taxol during a 72-hour imaging period), and no dose-response experiments were performed. Further investigations of such dose-response effects are warranted.

Second, RKO cells exposed to taxol exhibit a markedly distinct response to the prolonged taxol exposure, i.e., the duration of mitotic arrest induced by taxol in RKO cells is significantly longer compared to the durations of the arrest induced by nocodazole, monastrol, or AZ138. This effect achieves statistical significance beyond the ¡ 0.001 level. Our results suggest that taxol is more efficient at inducing RKO cell death compared to the kinesin-5 inhibitors and nocodazole, but requires a longer duration of mitotic arrest to induce its proapoptotic effect compared to other antimitotic drugs, an observation also pointed out in [207].

Third, our results indicate that the fraction of RKO cells that either die or slip after entering mitosis following continued exposure to nocodazole, monastrol, AZ138, and taxol can be well-approximated by Gamma distributions. Specifically, our results indicate that the shape parameter k of the Gamma distributions corresponding to the fraction of RKO cells that die in mitosis under non-taxol and taxol exposure, or slip back into interphase is 5.91, 4.43, or 3.95, respectively. Interestingly, these values suggests the existence of approximately six or four independent, exponentially distributed random variables, each modeling an event responsible for inducing RKO cell death by the non-taxol drugs, and taxol, respectively.

These events could, for example, be correlated with the activation of executive caspases, Bcl-xL expression levels, the depletion of the anti-apoptotic protein Mcl-1, increased microtubule stabilization leading to interference with cellular trafficking and microtubule-mediated cellular transport, or sequestration of Bax/Bak sufficient to trigger Mitochondrial Outer Membrane Permeabilization (MOMP).

Additionally, our results also suggest the existence of four independent exponentially distributed random variables responsible for inducing mitotic slippage and survival of the RKO cells in interphase. These events could, for example, be correlated with cyclin B1 level degradation, or the prolonged activation of Cdk1.

Fourth, our results indicate that RKO cells exhibit a triphasic response curve irrespective of cell fate or antimitotic drug. To the best of our knowledge, this observation was previously unrecognized. Interestingly, RKO cells remain in mitotic arrest for periods of time shorter than 1.5 hours, then undergo a fast transition from arrest to death in mitosis or to mitotic slippage and return in interphase as long as the duration of mitotic arrest is shorter than 24 hours. If cells continue to remain in mitotic arrest for more than 24 hours, their subsequent transition to cellular death or slippage is slower compared to the first phase of transition.

Lastly, our numerical simulations provide quantitative evidence to support the hypothesis that the duration of mitotic arrest predicts cell fate in RKO cells. Under prolonged 0.03 µM AZ138 and 100 µM monastrol exposure, RKO cells are more likely to undergo mitotic slippage rather than death in mitosis for shorter durations of mitotic arrest, i.e., 11.73 and 14.65 hours, respectively. One possible explanation for this observation is that cyclin B1 degradation in RKO cells might cause cyclin B1 levels to fall below its mitotic exit threshold before the accumulation of cell death signals sufficient to trigger MOMP.

A short mitotic arrest might thus not allow proapoptotic signals to accumulate sufficiently in order to trigger cell death in RKO cells. Conversely, for longer durations of mitotic arrest, cells are more likely to undergo death in mitosis rather than mitotic slippage. This suggests that for antimitotic drugs to be able to exert their proapoptotic effect, exposing cancer cells to antimitotics for prolonged periods of time and to constant drug concentrations might be more efficient in inducing cell death than withdrawing the drug after a short exposure. This effect is especially relevant in taxol-treated RKO cells, as our quantitative modeling results suggest.

In the current work, we provide an *in silico* modeling framework for studying the emerging heterogeneity in the response of the colon carcinoma RKO cell line to antimitotic drugs. Our *in silico* quantitative approach incorporates experimental results and uses mathematical models in order to better inform *in vitro* phenomena. Our modeling framework will serve as a basis for future studies of cancer cell heterogeneity *in vitro* of more complex responses in the presence of antimitotic drugs of both apoptosis-resistant and apoptosis-sensitive cell lines other than the RKO cell line.

Chapter 6: Conclusion

Ovarian cancer is the most lethal gynecologic malignancy and the 5^{th} leading cause of death among U.S. women [4]. In addition to optimized surgery and chemotherapy protocols, significant progress has been made in recent years through the development of drugs targeting deficiencies in the double-stranded DNA repair mechanisms, i.e., homologous-recombination repair deficiency (HRD) [225].

For example, PARP inhibitors, such as olaparib or niraparib, have shown promising activity both *in vitro* and *in vivo* as maintenance therapy and as treatment for advanced recurrent platinum-sensitive or resistant ovarian cancers [93]. In coming years, combination strategies involving PARP inhibitors are likely to bring further major improvements in the management and treatment of ovarian cancers, e.g., in combination with the Vascular Endothelial Growth Factor (VEGFR), Tyrone Kinase Inhibitor (TKI) cediranib, the angiogenic inhibitor bevacizumab, or the programmed death-ligand 1 (PD-L1) inhibitor, durvalumab [3, 226, 227].

This represents an exciting time for the mathematical oncology community studying ovarian cancer natural history, growth, progression or dynamic response to treatment in an integrated systems biology/mathematical framework. If accurately and realistically applied to existing clinical data, such frameworks can complement existing clinical results, obtained from large-scale cohort studies or *vitro*, as these mathematical experiments can be performed in a relatively inexpensive manner that relies only on computing power.

Moreover, mathematical models can be used to investigate and highlight potential underlying mechanisms behind the observed experimental data. They provide an inexpensive framework in which various hypotheses can be tested before performing time-consuming experiments or awaiting clinical trial results.

In addition, mathematical modeling can potentially identify the most relevant parameters in order to guide the experimental design, and subsequently reveal temporal or spatial information related to these parameters. Once a modeling framework has undergone calibration and validation, it can be used to generate and predict long-term effects of therapies that would otherwise not be available without large prospective cohort studies.

In this dissertation we constructed and studied various mathematical modeling framework aimed at studying the natural history, growth and progression of ovarian cancers from a population and single-cell level perspective.

First, in Chapter 3, we provided a quantitative mathematical explanation for why HGSOC detection is not amenable to frequent TVU monitoring, supporting the clinical findings reported in [101] and results from prospective TVU screening trials such as the UKTOCS or PLCO.

Next, in Chapter 4, we introduced a mathematical modeling framework of OVCAR-8 cancer cell dynamics under prolonged antimitotic drug exposure that incorporates an intrinsic form of heterogeneity via the duration of times cells spend in the cell-cycle and apoptosis process. Our work highlighted the fact that the transient behavior in the cancer cell growth dynamics can signal the emergence and maintenance of a steady quiescent cell population.

This, in turn, represents a form of intrinsic, non-genetic resistance that results from variations in cell-cycle parameters [193, 194]. The resulting form of resistance can potentially decrease the efficacy of therapies that rely on active cell-cycling for their killing effects, such as traditional chemotherapies [195–197].

Moreover, our result suggest that, unless exposed to saturating drug concentrations for prolonged periods of time, cancer cells may not experience a mitotic arrest for long enough in order to trigger apoptosis, which may have therapeutic implications as clinical responses depends on apoptosis rates, and not exclusively on mitotic arrest [137, 189].

Lastly, in Chapter 5, we used published single-cell data [151] to study the kinetics of the death in mitosis and mitotic slippage pathways, responsible for mediating the two predominant cancer cell fate responses following prolonged mitotic arrest. Our modeling results suggest that biochemically distinct antimitotic drugs can induce functionally similar responses in cancer cells.

Moreover, our study highlights the fact that taxol is more efficient at inducing cell death compared to other drugs, yet it requires a longer duration of mitotic arrest to induce its proapoptotic effect, an observation also pointed out in [207].

Several open questions remain unresolved: what are the rates and thresholds characterizing each network? Why are some cell lines more prone to being apoptosis-sensitive regardless of the anti-mitotic drug used, but others are more apoptosis-resistant and exhibit a diverse range of cell fates during prolonged mitotic arrest?

Future methodological approaches used to address these questions could involve a variety of ODE-PDE models for representing cellular age, as a cell's progression through the cell-cycle and mitosis is stalled during mitotic arrest.

Phenotypically structured equations, which arise in population dynamics, could potentially be used to represent the different cell phenotypes as cells undergo mitotic arrest. Examples include cells that die in mitosis during the arrest, cells that return to interphase and die in a subsequent mitosis, cells that return to interphase and survive, or cells that successfully divide. We leave this for a future work.

This dissertation represents the product of an active collaboration between mathematicians, clinicians, and experimentalists with the goal of ultimately improving ovarian cancer patient care in the long-term. I strongly believe that in order to achieve this goal, the design of future mathematical models will have to closely follow women's cancers biology, be driven by it, and be closely supported and informed by clinical and experimental data.

Bibliography

[1] US Census Bureau. US Census Bureau Age and Sex Composition: 2010. `https://www.census.gov/2010census/data/`, 2015. [Online; accessed September-17-2017].

[2] D. A. Botesteanu, S. Lipkowitz, J. M. Lee, and D. Levy. Mathematical models of breast and ovarian cancers. *Wiley Interdiscip Rev Syst Biol Med*, 8(4):337–362, Jul 2016.

[3] J. M. Lee, A. Cimino-Mathews, C. J. Peer, A. Zimmer, S. Lipkowitz, C. M. Annunziata, L. Cao, M. I. Harrell, E. M. Swisher, N. Houston, D. A. Botesteanu, J. M. Taube, E. Thompson, A. Ogurtsova, H. Xu, J. Nguyen, T. W. Ho, W. D. Figg, and E. C. Kohn. Safety and Clinical Activity of the Programmed Death-Ligand 1 Inhibitor Durvalumab in Combination With Poly (ADP-Ribose) Polymerase Inhibitor Olaparib or Vascular Endothelial Growth Factor Receptor 1-3 Inhibitor Cediranib in Women's Cancers: A Dose-Escalation, Phase I Study. *J. Clin. Oncol.*, 35(19):2193–2202, Jul 2017.

[4] R. L. Siegel, K. D. Miller, and A. Jemal. Cancer Statistics, 2017. *CA Cancer J Clin*, 67(1):7–30, Jan 2017.

[5] S. S. Buys, E. Partridge, M. H. Greene, P. C. Prorok, D. Reding, T. L. Riley, P. Hartge, R. M. Fagerstrom, L. R. Ragard, D. Chia, G. Izmirlian, M. Fouad, C. C. Johnson, and J. K. Gohagan. Ovarian cancer screening in the Prostate, Lung, Colorectal and Ovarian (PLCO) cancer screening trial: findings from the initial screen of a randomized trial. *Am. J. Obstet. Gynecol.*, 193(5):1630–1639, Nov 2005.

[6] S. Sundar, C. Rick, F. Dowling, P. Au, K. Snell, N. Rai, R. Champaneria, H. Stobart, R. Neal, C. Davenport, S. Mallett, A. Sutton, S. Kehoe, D. Timmerman, T. Bourne, B. Van Calster, A. Gentry-Maharaj, U. Menon, J. Deeks, H. Nagar, P. Abedin, K. Jermy, F. Ghazal, T. Duncan, T. Hughes, M. Willett, S. Abdi, P. Keating, S. Kaushik, M. Roberts, P. Sengupta, A. Sharma, M. Balogun, H. Khan, H. Rai, V. Ames, S. Johnson, E. Nagaraju, T. Butcher,

L. Vitta, Y. McGrady, R. Kent, and A. Sinha. Refining Ovarian Cancer Test accuracy Scores (ROCkeTS): protocol for a prospective longitudinal test accuracy study to validate new risk scores in women with symptoms of suspected ovarian cancer. *BMJ Open*, 6(8):e010333, Aug 2016.

[7] B. A. Goff, L. S. Mandel, C. W. Drescher, N. Urban, S. Gough, K. M. Schurman, J. Patras, B. S. Mahony, and M. R. Andersen. Development of an ovarian cancer symptom index: possibilities for earlier detection. *Cancer*, 109(2):221–227, Jan 2007.

[8] I. Meinhold-Heerlein, C. Fotopoulou, P. Harter, C. Kurzeder, A. Mustea, P. Wimberger, S. Hauptmann, and J. Sehouli. The new WHO classification of ovarian, fallopian tube, and primary peritoneal cancer and its clinical implications. *Arch. Gynecol. Obstet.*, 293(4):695–700, Apr 2016.

[9] D. J. Storey, R. Rush, M. Stewart, T. Rye, A. Al-Nafussi, A. R. Williams, J. F. Smyth, and H. Gabra. Endometrioid epithelial ovarian cancer : 20 years of prospectively collected data from a single center. *Cancer*, 112(10):2211–2220, May 2008.

[10] D. D. Bowtell. The genesis and evolution of high-grade serous ovarian cancer. *Nat. Rev. Cancer*, 10(11):803–808, 11 2010.

[11] J. K. Chan, C. Tian, B. J. Monk, T. Herzog, D. S. Kapp, J. Bell, and R. C. Young. Prognostic factors for high-risk early-stage epithelial ovarian cancer: a Gynecologic Oncology Group study. *Cancer*, 112(10):2202–2210, May 2008.

[12] J. M. Piek, P. J. van Diest, R. P. Zweemer, J. W. Jansen, R. J. Poort-Keesom, F. H. Menko, J. J. Gille, A. P. Jongsma, G. Pals, P. Kenemans, and R. H. Verheijen. Dysplastic changes in prophylactically removed Fallopian tubes of women predisposed to developing ovarian cancer. *J. Pathol.*, 195(4):451–456, Nov 2001.

[13] N. D. Kauff, J. M. Satagopan, M. E. Robson, L. Scheuer, M. Hensley, C. A. Hudis, N. A. Ellis, J. Boyd, P. I. Borgen, R. R. Barakat, L. Norton, M. Castiel, K. Nafa, and K. Offit. Risk-reducing salpingo-oophorectomy in women with a BRCA1 or BRCA2 mutation. *N. Engl. J. Med.*, 346(21):1609–1615, May 2002.

[14] M. L. Carcangiu, B. Peissel, B. Pasini, G. Spatti, P. Radice, and S. Manoukian. Incidental carcinomas in prophylactic specimens in BRCA1 and BRCA2 germline mutation carriers, with emphasis on fallopian tube lesions: report of 6 cases and review of the literature. *Am. J. Surg. Pathol.*, 30(10):1222–1230, Oct 2006.

[15] Y. Lee, A. Miron, R. Drapkin, M. R. Nucci, F. Medeiros, A. Saleemuddin, J. Garber, C. Birch, H. Mou, R. W. Gordon, D. W. Cramer, F. D. McKeon,

and C. P. Crum. A candidate precursor to serous carcinoma that originates in the distal fallopian tube. *J. Pathol.*, 211(1):26–35, Jan 2007.

[16] M. J. Callahan, C. P. Crum, F. Medeiros, D. W. Kindelberger, J. A. Elvin, J. E. Garber, C. M. Feltmate, R. S. Berkowitz, and M. G. Muto. Primary fallopian tube malignancies in BRCA-positive women undergoing surgery for ovarian cancer risk reduction. *J. Clin. Oncol.*, 25(25):3985–3990, Sep 2007.

[17] P. A. Shaw, M. Rouzbahman, E. S. Pizer, M. Pintilie, and H. Begley. Candidate serous cancer precursors in fallopian tube epithelium of BRCA1/2 mutation carriers. *Mod. Pathol.*, 22(9):1133–1138, Sep 2009.

[18] K. K. Mehra, M. C. Chang, A. K. Folkins, C. J. Raho, J. F. Lima, L. Yuan, M. Mehrad, S. S. Tworoger, C. P. Crum, and A. Saleemuddin. The impact of tissue block sampling on the detection of p53 signatures in fallopian tubes from women with BRCA 1 or 2 mutations (BRCA+) and controls. *Mod. Pathol.*, 24(1):152–156, Jan 2011.

[19] I. J. Jacobs, U. Menon, A. Ryan, A. Gentry-Maharaj, M. Burnell, J. K. Kalsi, N. N. Amso, S. Apostolidou, E. Benjamin, D. Cruickshank, D. N. Crump, S. K. Davies, A. Dawnay, S. Dobbs, G. Fletcher, J. Ford, K. Godfrey, R. Gunu, M. Habib, R. Hallett, J. Herod, H. Jenkins, C. Karpinskyj, S. Leeson, S. J. Lewis, W. R. Liston, A. Lopes, T. Mould, J. Murdoch, D. Oram, D. J. Rabideau, K. Reynolds, I. Scott, M. W. Seif, A. Sharma, N. Singh, J. Taylor, F. Warburton, M. Widschwendter, K. Williamson, R. Woolas, L. Fallowfield, A. J. McGuire, S. Campbell, M. Parmar, and S. J. Skates. Ovarian cancer screening and mortality in the UK Collaborative Trial of Ovarian Cancer Screening (UKCTOCS): a randomised controlled trial. *Lancet*, 387(10022):945–956, Mar 2016.

[20] L. J. Havrilesky, G. D. Sanders, S. Kulasingam, J. P. Chino, A. Berchuck, J. R. Marks, and E. R. Myers. Development of an ovarian cancer screening decision model that incorporates disease heterogeneity: implications for potential mortality reduction. *Cancer*, 117(3):545–553, Feb 2011.

[21] S. S. Buys, E. Partridge, A. Black, C. C. Johnson, L. Lamerato, C. Isaacs, D. J. Reding, R. T. Greenlee, L. A. Yokochi, B. Kessel, E. D. Crawford, T. R. Church, G. L. Andriole, J. L. Weissfeld, M. N. Fouad, D. Chia, B. O'Brien, L. R. Ragard, J. D. Clapp, J. M. Rathmell, T. L. Riley, P. Hartge, P. F. Pinsky, C. S. Zhu, G. Izmirlian, B. S. Kramer, A. B. Miller, J. L. Xu, P. C. Prorok, J. K. Gohagan, C. D. Berg, C. D. Berg, J. K. Gohagan, P. C. Prorok, A. W. Hsing, J. V. Lacey, M. Purdue, R. B. Hayes, A. Black, W. Y. Huang, N. K. Simpson, R. Cumberlin, S. Rossi, C. Zhu, G. Marquez, J. E. Browne, S. Hoffman, D. M. Coleman, C. Jackson, E. Lange, D. McMillan, E. Papadopoulos, D. Sylver-Foust, D. Sullivan, M. Brown, J. Gaegler, L. Gray, A. Hansborough, P. Greenwald, J. F. Fraumeni, R. M. Fagerstrom, P. Hu, G. Izmirlian, D. L. Levin, P. Pinsky, J. L. Xu, A. Kreimer, P. M. Marcus,

A. F. Subar, A. Black, P. Hartge, R. N. Hoover, R. G. Ziegler, R. Costlow, A. F. Laine, A. B. Miller, D. Pearson, J. R. van Nagell, F. L. Stallings, D. S. Miller, B. S. Kramer, D. Chia, S. Dry, D. Seligson, P. Terasaki, J. Reiss, S. Tze, A. Acalinovich, S. Besada, H. Chan, G. Cheung-Lau, S. Corbett, P. Durongwong, M. Eeva, L. Folayan, B. Gruebel, O. Habeeb, K. Huynh, C. Kanegai, H. Kim, S. Kim, A. Ko, S. Kohlmeier, C. Lamb, M. Lu, J. Martin, S. Maynard, F. Noravian, O. Schirrippa, G. Padilla, A. Rumbin, L. Shevlin, R. Ty, Q. Wang, J. Wong, S. Xu, H. Yu, J. Koci, W. Kopp, H. Rager, C. Smith, D. Roser, J. Cahill, B. O'Brien, S. Gardner, D. Carrick, S. Yurgalevitch, M. Dunn, C. Bailey, Y. Bodenstein, P. Burr, J. Cutrin, J. Eisen, A. Frias, S. Glashofer, K. Hurt-Mullen, K. Kavounis, P. Ke, F. Khanani, B. Laimon, L. Mechanic, M. Mesnard, L. Nichaman, S. Novey, C. Palace, S. Peace, K. Pettit, S. Pratt, L. Ragard, J. Rosenbaum, D. Sanchez, S. Schuman, M. Stewart, M. B. Waterman, K. Umbel, D. Ferrantello, B. Havel, M. A. Hasson, B. Bridgeman, E. Martinusen, M. Sabastianelli, A. Miller, F. Menacker, M. Miedzinski, S. Chowdry, L. Miesko, C. Lease, M. Rinehart, M. Agamir, K. Awatramani, J. Barbee, W. C. Barlow, D. Beach, B. Bradley, K. Brenner, L. Butler, J. Bristor, C. Caughman, R. Chanapatna, L. Cranson, J. Desir, K. Donegan, J. Fleming, M. Florczyk, J. Galyon, C. Gordon, C. Han, A. Hendricks, D. Hickman, M. Ho, E. Jackson, D. C. Kahane, A. Khan, M. Laio, A. Lee, B. Lott, D. Lucas-Mudd, D. Moore, A. Morgan, G. Neagu, P. Ohan, M. Revzin, J. Rychlec, R. Samiel, E. Siford, D. Simons, M. Smith, L. Swei, E. Theodorou, A. Vakhlis, J. H. Walsh, B. Wenzel, M. Whitlock, S. Williamson, M. Wu, C. L. Yang, S. Yoda, M. Wu, M. H. Myers, P. A. Young, D. A. Lewis, R. W. Francis, L. A. Saunders, C. Signes, S. Scheck, W. Lake, T. Riley, J. Austin, D. E. Erwin, D. Flynn, J. E. Mabie, J. D. Clapp, M. R. Moore, F. Xu, G. C. Jones, J. M. Rathmell, C. R. Williams, M. Young, A. Goodman, T. P. Hickey, J. M. Commins, P. Wright, S. K. Shaul, E. D. Crawford, S. L. Ogden, S. Tenorio, P. Fyles, D. Golz, S. Hommel, D. McCormick, G. Pashleigh, N. Slimak, N. Turner, N. G. Ayodeji, D. Josse, J. McAfee, E. Meskimen, J. Pennington, W. Suchey, M. Ali-Ahmadi, A. W. Barnett, J. Brothers, N. D. Chronister, D. Cipolla, R. Crawford, S. Chun, K. Gebhart, J. Hernandez, H. Hunter, K. Patel, W. Poage, M. Pozzetta, S. Simms, J. Swingler, C. Taylor, M. Turner, A. Wallack, K. Curtis, D. Pierce, P. V. Borrego, C. Rundus, E. Bonde, E. Gamito, S. Pretzel, J. Dahmer, T. Deines, M. Geske, M. Holladay, H. Jackson, T. Jordan, E. Ordonez, T. Beechum, M. Crawford, K. Dittmer, A. Donohue, F. Garcia, S. Giese, A. Klenfield, M. Kleinman, W. Moss, K. Motomiya, R. Murken, D. Neel, J. Quintela, C. Razook, A. Shoaga, A. Thompson, S. Vargas, D. Lynch, M. O'Driscoll, R. Townsend, E. Stamm, J. Drose, S. Davidson, D. Ahnen, J. Levine, W. Murchison, S. Steinberg, E. P. Gelmann, C. Isaacs, C. McGuire, N. Trocky, C. Bourdeau, P. Ke, L. Martino, I. Apostolides, C. Elbon-Copp, K. Klemm, C. Lippman, C. Klotz, T. McLaurin, S. Cantrell, G. Marsh, A. Tran, C. Wray, B. Yondonsambu, C. Taddeo, K. Bennett, T. Bowen, K. English, K. Seaton, T. Hammond, M. Ford, K. Newman, M. Kren, N. English, D. McKenzie, L. A. Yokochi, F. Gilbert, D. Curb,

J. Davis, B. Kessel, J. Navin, H. Petrovich, V. Shambaugh, F. Tabrah, B. Waitzfelder, B. Willcox, V. Jenkins, R. Chasnoff, J. Vander Does, J. Martin, B. Ideta, K. Stryker, E. Batangan, L. Dolan, K. Horton, K. Taylor, T. Tokumine, R. Troyer, S. Barrow, S. Hayashida, S. Commander, L. Turner, G. Hino, E. Nakano, M. Johnson, L. Villaruz, A. Chung, W. Huynh, N. Hickey, M. Calulot, V. Chun, C. Lewis, J. Morfit, J. Tani, K. Banggo, A. Brunst, W. Francis, L. Grove, B. Holderbaum, B. Holderbaum, K. Kinney, M. Ogino, T. O'Sullivan, P. Rowan-Lau, K. Bow, H. Shiratori, J. Tsukamoto, H. Hodges, S. Hyun, J. Kuiee, L. Lucente, P. Oshiro, K. Shota, P. A. Kvale, R. Demers, R. Fogel, W. Rutt, C. C. Johnson, L. Lamerato, R. S. Bresalier, K. Broski, S. Hensley-Alford, M. E. Ford, J. E. LaFata, B. McCarthy, R. War. Effect of screening on ovarian cancer mortality: the Prostate, Lung, Colorectal and Ovarian (PLCO) Cancer Screening Randomized Controlled Trial. *JAMA*, 305(22):2295–2303, Jun 2011.

[22] H. Kobayashi, Y. Yamada, T. Sado, M. Sakata, S. Yoshida, R. Kawaguchi, S. Kanayama, H. Shigetomi, S. Haruta, Y. Tsuji, S. Ueda, and T. Kitanaka. A randomized study of screening for ovarian cancer: a multicenter study in Japan. *Int. J. Gynecol. Cancer*, 18(3):414–420, 2008.

[23] I. Jacobs and U. Menon. Can ovarian cancer screening save lives? The question remains unanswered. *Obstet Gynecol*, 118(6):1209–1211, Dec 2011.

[24] R. Vang, I. e. M. Shih, and R. J. Kurman. Ovarian low-grade and high-grade serous carcinoma: pathogenesis, clinicopathologic and molecular biologic features, and diagnostic problems. *Adv Anat Pathol*, 16(5):267–282, Sep 2009.

[25] S. Jones, T. L. Wang, R. J. Kurman, K. Nakayama, V. E. Velculescu, B. Vogelstein, K. W. Kinzler, N. Papadopoulos, and I. e. M. Shih. Low-grade serous carcinomas of the ovary contain very few point mutations. *J. Pathol.*, 226(3):413–420, Feb 2012.

[26] V. A. Moyer, M. L. LeFevre, A. L. Siu, L. C. Baumann, K. Bibbins-Domingo, S. J. Curry, M. Ebell, G. Flores, A. G. Cantu, D. C. Grossman, J. Herzstein, J. Melnikow, W. K. Nicholson, D. K. Owens, C. Reyes, and T. J. Wilt. Screening for ovarian cancer: U.S. Preventive Services Task Force reaffirmation recommendation statement. *Ann. Intern. Med.*, 157(12):900–904, Dec 2012.

[27] C. F. Singer, M. K. Tea, G. Pristauz, M. Hubalek, C. Rappaport, C. C. Riedl, and T. H. Helbich. Clinical Practice Guideline for the prevention and early detection of breast and ovarian cancer in women from HBOC (hereditary breast and ovarian cancer) families. *Wien. Klin. Wochenschr.*, 127(23-24):981–986, Dec 2015.

[28] N. M. van der Velde, M. J. Mourits, H. J. Arts, J. de Vries, B. K. Leegte, G. Dijkhuis, J. C. Oosterwijk, and G. H. de Bock. Time to stop ovarian cancer screening in BRCA1/2 mutation carriers? *Int. J. Cancer*, 124(4):919–923, Feb 2009.

[29] J. R. van Nagell, R. W. Miller, C. P. DeSimone, F. R. Ueland, I. Podzielinski, S. T. Goodrich, J. W. Elder, B. Huang, R. J. Kryscio, and E. J. Pavlik. Long-term survival of women with epithelial ovarian cancer detected by ultrasonographic screening. *Obstet Gynecol*, 118(6):1212–1221, Dec 2011.

[30] U. Menon, A. Gentry-Maharaj, R. Hallett, A. Ryan, M. Burnell, A. Sharma, S. Lewis, S. Davies, S. Philpott, A. Lopes, K. Godfrey, D. Oram, J. Herod, K. Williamson, M. W. Seif, I. Scott, T. Mould, R. Woolas, J. Murdoch, S. Dobbs, N. N. Amso, S. Leeson, D. Cruickshank, A. McGuire, S. Campbell, L. Fallowfield, N. Singh, A. Dawnay, S. J. Skates, M. Parmar, and I. Jacobs. Sensitivity and specificity of multimodal and ultrasound screening for ovarian cancer, and stage distribution of detected cancers: results of the prevalence screen of the UK Collaborative Trial of Ovarian Cancer Screening (UKCTOCS). *Lancet Oncol.*, 10(4):327–340, Apr 2009.

[31] C. Marth, M. Hubalek, E. Petru, S. Polterauer, A. Reinthaller, C. Schauer, T. Scholl-Firon, C. F. Singer, J. Zschocke, and A. G. Zeimet. AGO Austria recommendations for genetic testing of patients with ovarian cancer. *Wien. Klin. Wochenschr.*, 127(15-16):652–654, Aug 2015.

[32] M. Petrillo, C. Marchetti, R. De Leo, A. Musella, E. Capoluongo, I. Paris, P. Benedetti Panici, G. Scambia, and A. Fagotti. BRCA mutational status, initial disease presentation, and clinical outcome in high-grade serous advanced ovarian cancer: a multicenter study. *Am. J. Obstet. Gynecol.*, 217(3):1–334, Sep 2017.

[33] J. A. Villella, M. Parmar, K. Donohue, C. Fahey, M. S. Piver, and K. Rodabaugh. Role of prophylactic hysterectomy in patients at high risk for hereditary cancers. *Gynecol. Oncol.*, 102(3):475–479, Sep 2006.

[34] J. B. Madalinska, M. van Beurden, E. M. Bleiker, H. B. Valdimarsdottir, L. Lubsen-Brandsma, L. F. Massuger, M. J. Mourits, K. N. Gaarenstroom, E. B. van Dorst, H. van der Putten, H. Boonstra, and N. K. Aaronson. Predictors of prophylactic bilateral salpingo-oophorectomy compared with gynecologic screening use in BRCA1/2 mutation carriers. *J. Clin. Oncol.*, 25(3):301–307, Jan 2007.

[35] A. Finch, G. Evans, and S. A. Narod. BRCA carriers, prophylactic salpingo-oophorectomy and menopause: clinical management considerations and recommendations. *Womens Health (Lond)*, 8(5):543–555, Sep 2012.

[36] N. D. Kauff, S. M. Domchek, T. M. Friebel, M. E. Robson, J. Lee, J. E. Garber, C. Isaacs, D. G. Evans, H. Lynch, R. A. Eeles, S. L. Neuhausen, M. B. Daly, E. Matloff, J. L. Blum, P. Sabbatini, R. R. Barakat, C. Hudis, L. Norton, K. Offit, and T. R. Rebbeck. Risk-reducing salpingo-oophorectomy for the prevention of BRCA1- and BRCA2-associated breast and gynecologic cancer: a multicenter, prospective study. *J. Clin. Oncol.*, 26(8):1331–1337, Mar 2008.

[37] A. Eisen, J. Lubinski, J. Klijn, P. Moller, H. T. Lynch, K. Offit, B. Weber, T. Rebbeck, S. L. Neuhausen, P. Ghadirian, W. D. Foulkes, R. Gershoni-Baruch, E. Friedman, G. Rennert, T. Wagner, C. Isaacs, C. Kim-Sing, P. Ainsworth, P. Sun, and S. A. Narod. Breast cancer risk following bilateral oophorectomy in BRCA1 and BRCA2 mutation carriers: an international case-control study. *J. Clin. Oncol.*, 23(30):7491–7496, Oct 2005.

[38] T. R. Rebbeck, N. D. Kauff, and S. M. Domchek. Meta-analysis of risk reduction estimates associated with risk-reducing salpingo-oophorectomy in BRCA1 or BRCA2 mutation carriers. *J. Natl. Cancer Inst.*, 101(2):80–87, Jan 2009.

[39] D. D. Bowtell, S. Bohm, A. A. Ahmed, P. J. Aspuria, R. C. Bast, V. Beral, J. S. Berek, M. J. Birrer, S. Blagden, M. A. Bookman, J. D. Brenton, K. B. Chiappinelli, F. C. Martins, G. Coukos, R. Drapkin, R. Edmondson, C. Fotopoulou, H. Gabra, J. Galon, C. Gourley, V. Heong, D. G. Huntsman, M. Iwanicki, B. Y. Karlan, A. Kaye, E. Lengyel, D. A. Levine, K. H. Lu, I. A. McNeish, U. Menon, S. A. Narod, B. H. Nelson, K. P. Nephew, P. Pharoah, D. J. Powell, P. Ramos, I. L. Romero, C. L. Scott, A. K. Sood, E. A. Stronach, and F. R. Balkwill. Rethinking ovarian cancer II: reducing mortality from high-grade serous ovarian cancer. *Nat. Rev. Cancer*, 15(11):668–679, Nov 2015.

[40] U. Menon, M. Griffin, and A. Gentry-Maharaj. Ovarian cancer screening–current status, future directions. *Gynecol. Oncol.*, 132(2):490–495, Feb 2014.

[41] R. Palmirotta, E. Silvestris, S. D'Oronzo, A. Cardascia, and F. Silvestris. Ovarian cancer: Novel molecular aspects for clinical assessment. *Crit. Rev. Oncol. Hematol.*, 117:12–29, Sep 2017.

[42] R. A. Burger. Experience with bevacizumab in the management of epithelial ovarian cancer. *J. Clin. Oncol.*, 25(20):2902–2908, Jul 2007.

[43] G. Aravantinos and D. Pectasides. Bevacizumab in combination with chemotherapy for the treatment of advanced ovarian cancer: a systematic review. *J Ovarian Res*, 7:57, 2014.

[44] J. A. Ledermann, P. Harter, C. Gourley, M. Friedlander, I. Vergote, G. Rustin, C. Scott, W. Meier, R. Shapira-Frommer, T. Safra, D. Matei, A. Fielding, S. Spencer, P. Rowe, E. Lowe, D. Hodgson, M. A. Sovak, and U. Matulonis. Overall survival in patients with platinum-sensitive recurrent serous ovarian cancer receiving olaparib maintenance monotherapy: an updated analysis from a randomised, placebo-controlled, double-blind, phase 2 trial. *Lancet Oncol.*, 17(11):1579–1589, Nov 2016.

[45] R. L. Coleman, A. M. Oza, D. Lorusso, C. Aghajanian, A. Oaknin, A. Dean, N. Colombo, J. I. Weberpals, A. Clamp, G. Scambia, A. Leary, R. W. Holloway, M. A. Gancedo, P. C. Fong, J. C. Goh, D. M. O'Malley, D. K. Armstrong, J. Garcia-Donas, E. M. Swisher, A. Floquet, G. E. Konecny, I. A. McNeish, C. L. Scott, T. Cameron, L. Maloney, J. Isaacson, S. Goble, C. Grace,

T. C. Harding, M. Raponi, J. Sun, K. K. Lin, H. Giordano, J. A. Ledermann, M. Buck, A. Dean, M. L. Friedlander, J. C. Goh, P. Harnett, G. Kichenadasse, C. L. Scott, H. Denys, L. Dirix, I. Vergote, L. Elit, P. Ghatage, A. M. Oza, M. Plante, D. Provencher, J. I. Weberpals, S. Welch, A. Floquet, L. Gladieff, F. Joly, A. Leary, A. Lortholary, J. Lotz, J. Medioni, O. Tredan, B. You, A. El-Balat, C. Hanle, P. Krabisch, T. Neunhoffer, M. Polcher, P. Wimberger, A. Amit, S. Kovel, M. Leviov, T. Safra, R. Shapira-Frommer, S. Stemmer, A. Bologna, N. Colombo, D. Lorusso, S. Pignata, R. F. Sabbatini, G. Scambia, S. Tamberi, C. Zamagni, P. C. Fong, A. O'Donnell, M. A. Gancedo, A. C. Herraez, J. Garcia-Donas, E. M. Guerra, A. Oaknin, I. Palacio, I. Romero, A. Sanchez, S. N. Banerjee, A. Clamp, Y. Drew, H. G. Gabra, D. Jackson, J. A. Ledermann, I. A. McNeish, C. Parkinson, M. Powell, C. Aghajanian, D. K. Armstrong, M. J. Birrer, M. K. Buss, S. K. Chambers, L. M. Chen, R. L. Coleman, R. W. Holloway, G. E. Konecny, L. Ma, M. A. Morgan, R. T. Morris, D. G. Mutch, D. M. O'Malley, B. M. Slomovitz, E. M. Swisher, T. Vanderkwaak, and M. Vulfovich. Rucaparib maintenance treatment for recurrent ovarian carcinoma after response to platinum therapy (ARIEL3): a randomised, double-blind, placebo-controlled, phase 3 trial. *Lancet*, Sep 2017.

[46] C. E. DeSantis, C. C. Lin, A. B. Mariotto, R. L. Siegel, K. D. Stein, J. L. Kramer, R. Alteri, A. S. Robbins, and A. Jemal. Cancer treatment and survivorship statistics, 2014. *CA Cancer J Clin*, 64(4):252–271, 2014.

[47] N. G. Alkema, G. B. Wisman, A. G. van der Zee, M. A. van Vugt, and S. de Jong. Studying platinum sensitivity and resistance in high-grade serous ovarian cancer: Different models for different questions. *Drug Resist. Updat.*, 24:55–69, Jan 2016.

[48] K. Nakayama, A. Kanzaki, K. Ogawa, K. Miyazaki, N. Neamati, and Y. Takebayashi. Copper-transporting P-type adenosine triphosphatase (ATP7B) as a cisplatin based chemoresistance marker in ovarian carcinoma: comparative analysis with expression of MDR1, MRP1, MRP2, LRP and BCRP. *Int. J. Cancer*, 101(5):488–495, Oct 2002.

[49] M. Sakamoto, A. Kondo, K. Kawasaki, T. Goto, H. Sakamoto, K. Miyake, Y. Koyamatsu, T. Akiya, H. Iwabuchi, T. Muroya, K. Ochiai, T. Tanaka, Y. Kikuchi, and Y. Tenjin. Analysis of gene expression profiles associated with cisplatin resistance in human ovarian cancer cell lines and tissues using cDNA microarray. *Hum. Cell*, 14(4):305–315, Dec 2001.

[50] F. F. Rodrigues, R. E. Santos, M. B. Melo, M. A. Silva, A. L. Oliveira, R. L. Rozenowicz, L. B. Ulson, and T. Aoki. Correlation of polymorphism C3435T of the MDR-1 gene and the response of primary chemotherapy in women with locally advanced breast cancer. *Genet. Mol. Res.*, 7(1):177–183, Feb 2008.

[51] W. Sakai, E. M. Swisher, B. Y. Karlan, M. K. Agarwal, J. Higgins, C. Friedman, E. Villegas, C. Jacquemont, D. J. Farrugia, F. J. Couch, N. Urban, and

T. Taniguchi. Secondary mutations as a mechanism of cisplatin resistance in BRCA2-mutated cancers. *Nature*, 451(7182):1116–1120, Feb 2008.

[52] E. M. Swisher, W. Sakai, B. Y. Karlan, K. Wurz, N. Urban, and T. Taniguchi. Secondary BRCA1 mutations in BRCA1-mutated ovarian carcinomas with platinum resistance. *Cancer Res.*, 68(8):2581–2586, Apr 2008.

[53] W. Sakai, E. M. Swisher, C. Jacquemont, K. V. Chandramohan, F. J. Couch, S. P. Langdon, K. Wurz, J. Higgins, E. Villegas, and T. Taniguchi. Functional restoration of BRCA2 protein by secondary BRCA2 mutations in BRCA2-mutated ovarian carcinoma. *Cancer Res.*, 69(16):6381–6386, Aug 2009.

[54] B. Norquist, K. A. Wurz, C. C. Pennil, R. Garcia, J. Gross, W. Sakai, B. Y. Karlan, T. Taniguchi, and E. M. Swisher. Secondary somatic mutations restoring BRCA1/2 predict chemotherapy resistance in hereditary ovarian carcinomas. *J. Clin. Oncol.*, 29(22):3008–3015, Aug 2011.

[55] A. Bashashati, G. Ha, A. Tone, J. Ding, L. M. Prentice, A. Roth, J. Rosner, K. Shumansky, S. Kalloger, J. Senz, W. Yang, M. McConechy, N. Melnyk, M. Anglesio, M. T. Luk, K. Tse, T. Zeng, R. Moore, Y. Zhao, M. A. Marra, B. Gilks, S. Yip, D. G. Huntsman, J. N. McAlpine, and S. P. Shah. Distinct evolutionary trajectories of primary high-grade serous ovarian cancers revealed through spatial mutational profiling. *J. Pathol.*, 231(1):21–34, Sep 2013.

[56] A. M. Patch, E. L. Christie, D. Etemadmoghadam, D. W. Garsed, J. George, S. Fereday, K. Nones, P. Cowin, K. Alsop, P. J. Bailey, K. S. Kassahn, F. Newell, M. C. Quinn, S. Kazakoff, K. Quek, C. Wilhelm-Benartzi, E. Curry, H. S. Leong, A. Hamilton, L. Mileshkin, G. Au-Yeung, C. Kennedy, J. Hung, Y. E. Chiew, P. Harnett, M. Friedlander, M. Quinn, J. Pyman, S. Cordner, P. O'Brien, J. Leditschke, G. Young, K. Strachan, P. Waring, W. Azar, C. Mitchell, N. Traficante, J. Hendley, H. Thorne, M. Shackleton, D. K. Miller, G. M. Arnau, R. W. Tothill, T. P. Holloway, T. Semple, I. Harliwong, C. Nourse, E. Nourbakhsh, S. Manning, S. Idrisoglu, T. J. Bruxner, A. N. Christ, B. Poudel, O. Holmes, M. Anderson, C. Leonard, A. Lonie, N. Hall, S. Wood, D. F. Taylor, Q. Xu, J. L. Fink, N. Waddell, R. Drapkin, E. Stronach, H. Gabra, R. Brown, A. Jewell, S. H. Nagaraj, E. Markham, P. J. Wilson, J. Ellul, O. McNally, M. A. Doyle, R. Vedururu, C. Stewart, E. Lengyel, J. V. Pearson, N. Waddell, A. deFazio, S. M. Grimmond, D. D. Bowtell, D. Bowtell, G. Chenevix-Trench, A. Green, P. Webb, A. DeFazio, D. Gertig, N. Traficante, S. Fereday, S. Moore, J. Hung, K. Harrap, T. Sadkowsky, N. Pandeya, M. Malt, A. Mellon, R. Robertson, T. Vanden Bergh, M. Jones, P. Mackenzie, J. Maidens, K. Nattress, Y. E. Chiew, A. Stenlake, H. Sullivan, B. Alexander, P. Ashover, S. Brown, T. Corrish, L. Green, L. Jackman, K. Ferguson, K. Martin, A. Martyn, B. Ranieri, J. White, V. Jayde, P. Mamers, L. Bowes, L. Galletta, D. Giles, J. Hendley, K. Alsop, T. Schmidt, H. Shirley, C. Ball, C. Young, S. Viduka, H. Tran, S. Bilic, L. Glavinas,

J. Brooks, R. Stuart-Harris, F. Kirsten, J. Rutovitz, P. Clingan, A. Glasgow, A. Proietto, S. Braye, G. Otton, J. Shannon, T. Bonaventura, J. Stewart, S. Begbie, M. Friedlander, D. Bell, S. Baron-Hay, A. Ferrier, G. Gard, D. Nevell, N. Pavlakis, S. Valmadre, B. Young, C. Camaris, R. Crouch, L. Edwards, N. Hacker, D. Marsden, G. Robertson, P. Beale, J. Beith, J. Carter, C. Dalrymple, R. Houghton, P. Russell, M. Links, J. Grygiel, J. Hill, A. Brand, K. Byth, R. Jaworski, P. Harnett, R. Sharma, G. Wain, B. Ward, D. Papadimos, A. Crandon, M. Cummings, K. Horwood, A. Obermair, L. Perrin, D. Wyld, J. Nicklin, M. Davy, M. K. Oehler, C. Hall, T. Dodd, T. Healy, K. Pittman, D. Henderson, J. Miller, J. Pierdes, P. Blomfield, D. Challis, R. McIntosh, A. Parker, B. Brown, R. Rome, D. Allen, P. Grant, S. Hyde, R. Laurie, M. Robbie, D. Healy, T. Jobling, T. Manolitsas, J. McNealage, P. Rogers, B. Susil, E. Sumithran, I. Simpson, K. Phillips, D. Rischin, S. Fox, D. Johnson, S. Lade, M. Loughrey, N. O'Callaghan, W. Murray, P. Waring, V. Billson, J. Pyman, D. Neesham, M. Quinn, C. Underhill, R. Bell, L. F. Ng, R. Blum, V. Ganju, I. Hammond, Y. Leung, A. McCartney, M. Buck, I. Haviv, D. Purdie, D. Whiteman, and N. Zeps. Whole-genome characterization of chemoresistant ovarian cancer. *Nature*, 521(7553):489–494, May 2015.

[57] K. P. Pennington, T. Walsh, M. I. Harrell, M. K. Lee, C. C. Pennil, M. H. Rendi, A. Thornton, B. M. Norquist, S. Casadei, A. S. Nord, K. J. Agnew, C. C. Pritchard, S. Scroggins, R. L. Garcia, M. C. King, and E. M. Swisher. Germline and somatic mutations in homologous recombination genes predict platinum response and survival in ovarian, fallopian tube, and peritoneal carcinomas. *Clin. Cancer Res.*, 20(3):764–775, Feb 2014.

[58] D. A. Botesteanu, J. M. Lee, and D. Levy. Modeling the Dynamics of High-Grade Serous Ovarian Cancer Progression for Transvaginal Ultrasound-Based Screening and Early Detection. *PLoS ONE*, 11(6):e0156661, 2016.

[59] A. Lorz, D. A. Botesteanu, and D. Levy. Modeling cancer cell growth dynamics in vitro in response to antimitotic drug treatment. *Frontiers in Oncology*, 7 (Special Issue: Cancer Models)(189), Aug 2017.

[60] A. Lorz, D. A. Botesteanu, and D. Levy. Modeling single cell heterogeneity in response to distinct antimitotic therapies in the RKO colon cancer cell line. *submitted*, Sep 2017.

[61] Cristini V. and Lowengrub J. *Multiscale Modeling of Cancer: An Integrated Experimental and Mathematical Modeling Approach.* Cambridge University Press.

[62] Epstein C. *Introduction to the Mathematics of Medical Imaging.* Society for Industrial and Applied Mathematics, 2 edition, 9 2007.

[63] R. Eftimie, J. L. Bramson, and D. J. Earn. Interactions between the immune system and cancer: a brief review of non-spatial mathematical models. *Bull. Math. Biol.*, 73(1):2–32, Jan 2011.

[64] W. M. Gregory, M. A. Richards, M. L. Slevin, and R. L. Souhami. A mathematical model relating response durations to amount of subclinical resistant disease. *Cancer Res.*, 51(4):1210–1216, Feb 1991.

[65] H. M. Byrne. Dissecting cancer through mathematics: from the cell to the animal model. *Nat. Rev. Cancer*, 10(3):221–230, Mar 2010.

[66] J. H. Goldie and A. J. Coldman. A mathematic model for relating the drug sensitivity of tumors to their spontaneous mutation rate. *Cancer Treat Rep*, 63(11-12):1727–1733, 1979.

[67] H. E. Skipper, F. M. Schabel, and W. S. Wilcox. Experimental evaluation of potential anticancer agents. XXI. Scheduling of arabinosylcytosine to take advantage of its S-phase specificity against leukemia cells. *Cancer Chemother Rep*, 51(3):125–165, Jun 1967.

[68] W. M. Gregory, C. J. Twelves, R. Bell, S. W. Smye, D. R. Howard, R. E. Coleman, and D. A. Cameron. Characterizing and quantifying the effects of breast cancer therapy using mathematical modeling. *Breast Cancer Res. Treat.*, 155(2):303–311, Jan 2016.

[69] F. Michor and K. Beal. Improving Cancer Treatment via Mathematical Modeling: Surmounting the Challenges Is Worth the Effort. *Cell*, 163(5):1059–1063, Nov 2015.

[70] C. H. Y. Cheung and H. F. Juan. Quantitative proteomics in lung cancer. *J. Biomed. Sci.*, 24(1):37, Jun 2017.

[71] K. Danesh, R. Durrett, L. J. Havrilesky, and E. Myers. A branching process model of ovarian cancer. *J. Theor. Biol.*, 314:10–15, Dec 2012.

[72] P. O. Brown and C. Palmer. The preclinical natural history of serous ovarian cancer: defining the target for early detection. *PLoS Med.*, 6(7):e1000114, Jul 2009.

[73] C. P. Crum, F. D. McKeon, and W. Xian. The oviduct and ovarian cancer: causality, clinical implications, and "targeted prevention". *Clin Obstet Gynecol*, 55(1):24–35, Mar 2012.

[74] J. T. Rabban, K. Garg, B. Crawford, L. M. Chen, and C. J. Zaloudek. Early detection of high-grade tubal serous carcinoma in women at low risk for hereditary breast and ovarian cancer syndrome by systematic examination of fallopian tubes incidentally removed during benign surgery. *Am. J. Surg. Pathol.*, 38(6):729–742, Jun 2014.

[75] M. J. Callahan, C. P. Crum, F. Medeiros, D. W. Kindelberger, J. A. Elvin, J. E. Garber, C. M. Feltmate, R. S. Berkowitz, and M. G. Muto. Primary fallopian tube malignancies in BRCA-positive women undergoing surgery for ovarian cancer risk reduction. *J. Clin. Oncol.*, 25(25):3985–3990, Sep 2007.

[76] M. L. Carcangiu, B. Peissel, B. Pasini, G. Spatti, P. Radice, and S. Manoukian. Incidental carcinomas in prophylactic specimens in BRCA1 and BRCA2 germline mutation carriers, with emphasis on fallopian tube lesions: report of 6 cases and review of the literature. *Am. J. Surg. Pathol.*, 30(10):1222–1230, Oct 2006.

[77] S. S. Hori and S. S. Gambhir. Mathematical model identifies blood biomarker-based early cancer detection strategies and limitations. *Sci Transl Med*, 3(109):109ra116, Nov 2011.

[78] S. J. Skates. Ovarian cancer screening: development of the risk of ovarian cancer algorithm (ROCA) and ROCA screening trials. *Int. J. Gynecol. Cancer*, 22 Suppl 1:S24–26, May 2012.

[79] S. Singh, M. Guetzko, and K. Resnick. Preoperative predictors of delay in initiation of adjuvant chemotherapy in patients undergoing primary debulking surgery for ovarian cancer. *Gynecol. Oncol.*, 143(2):241–245, Nov 2016.

[80] L. Kumar, R. Pramanik, S. Kumar, N. Bhatla, and S. Malik. Neoadjuvant chemotherapy in gynaecological cancers - Implications for staging. *Best Pract Res Clin Obstet Gynaecol*, 29(6):790–801, Aug 2015.

[81] A. E. Garcia-Soto, J. J. Java, W. Nieves Neira, J. M. Pearson, D. E. Cohn, S. B. Lele, K. S. Tewari, J. L. Walker, A. Alvarez Secord, D. K. Armstrong, and L. J. Copeland. Does time interval between surgery and intraperitoneal chemotherapy administration in advanced ovarian cancer carry a prognostic impact? An NRG Oncology/Gynecologic Oncology Group study ancillary study. *Gynecol. Oncol.*, 143(3):484–489, Dec 2016.

[82] M. Kohandel, S. Sivaloganathan, and A. Oza. Mathematical modeling of ovarian cancer treatments: sequencing of surgery and chemotherapy. *J. Theor. Biol.*, 242(1):62–68, Sep 2006.

[83] J. Morrison, K. Haldar, S. Kehoe, and T. A. Lawrie. Chemotherapy versus surgery for initial treatment in advanced ovarian epithelial cancer. *Cochrane Database Syst Rev*, (8):CD005343, Aug 2012.

[84] D. Mauri, N. Pavlidis, and J. P. Ioannidis. Neoadjuvant versus adjuvant systemic treatment in breast cancer: a meta-analysis. *J. Natl. Cancer Inst.*, 97(3):188–194, Feb 2005.

[85] H. V. Jain, A. Richardson, M. Meyer-Hermann, and H. M. Byrne. Exploiting the synergy between carboplatin and ABT-737 in the treatment of ovarian carcinomas. *PLoS ONE*, 9(1):e81582, 2014.

[86] H. V. Jain and M. Meyer-Hermann. The molecular basis of synergism between carboplatin and ABT-737 therapy targeting ovarian carcinomas. *Cancer Res.*, 71(3):705–715, Feb 2011.

[87] H. V. Jain, J. E. Nor, and T. L. Jackson. Quantification of endothelial cell-targeted anti-Bcl-2 therapy and its suppression of tumor growth and vascularization. *Mol. Cancer Ther.*, 8(10):2926–2936, Oct 2009.

[88] J. C. Panetta. A mathematical model of breast and ovarian cancer treated with paclitaxel. *Math Biosci*, 146(2):89–113, Dec 1997.

[89] F.S. Montalenti, G. Cappella, and P.P Ubezio. Simulating cancer-cell kinetics after drug treatment: Application to cisplatin on ovarian carcinoma. *Physical Review*, 57:58–77, 1998.

[90] A. Ciampi, L. Kates, R. Buick, Y. Kriukov, and J. E. Till. Multi-type Galton-Watson process as a model for proliferating human tumour cell populations derived from stem cells: estimation of stem cell self-renewal probabilities in human ovarian carcinomas. *Cell Tissue Kinet*, 19(2):129–140, Mar 1986.

[91] Q. Zhan, C. Wang, and S. Ngai. Ovarian cancer stem cells: a new target for cancer therapy. *Biomed Res Int*, 2013:916819, 2013.

[92] N. Staropoli, D. Ciliberto, S. Chiellino, F. Caglioti, T. D. Giudice, S. Gualtieri, A. Salvino, A. Strangio, C. Botta, S. Pignata, P. Tassone, and P. Tagliaferri. Is ovarian cancer a targetable disease? A systematic review and meta-analysis and genomic data investigation. *Oncotarget*, 7(50):82741–82756, Dec 2016.

[93] E. C. Kohn, S. Romano, and J. M. Lee. Clinical implications of using molecular diagnostics for ovarian cancers. *Ann. Oncol.*, 24 Suppl 10:22–26, Dec 2013.

[94] C. P. Crum, R. Drapkin, A. Miron, T. A. Ince, M. Muto, D. W. Kindelberger, and Y. Lee. The distal fallopian tube: a new model for pelvic serous carcinogenesis. *Curr. Opin. Obstet. Gynecol.*, 19(1):3–9, Feb 2007.

[95] O. Blyuss, A. Gentry-Maharaj, E. O. Fourkala, A. Ryan, A. Zaikin, U. Menon, I. Jacobs, and J. F. Timms. Serial Patterns of Ovarian Cancer Biomarkers in a Prediagnosis Longitudinal Dataset. *Biomed Res Int*, 2015:681416, 2015.

[96] P. F. Pinsky, C. Zhu, S. J. Skates, A. Black, E. Partridge, S. S. Buys, and C. D. Berg. Potential effect of the risk of ovarian cancer algorithm (ROCA) on the mortality outcome of the Prostate, Lung, Colorectal and Ovarian (PLCO) trial. *Int. J. Cancer*, 132(9):2127–2133, May 2013.

[97] J. F. Speer, V. E. Petrosky, M. W. Retsky, and R. H. Wardwell. A stochastic numerical model of breast cancer growth that simulates clinical data. *Cancer Res.*, 44(9):4124–4130, Sep 1984.

[98] J. R. van Nagell, P. D. DePriest, F. R. Ueland, C. P. DeSimone, A. L. Cooper, J. M. McDonald, E. J. Pavlik, and R. J. Kryscio. Ovarian cancer screening with annual transvaginal sonography: findings of 25,000 women screened. *Cancer*, 109(9):1887–1896, May 2007.

[99] J. R. van Nagell and J. T. Hoff. Transvaginal ultrasonography in ovarian cancer screening: current perspectives. *Int J Womens Health*, 6:25–33, Dec 2013.

[100] S. D. Harlow, M. Gass, J. E. Hall, R. Lobo, P. Maki, R. W. Rebar, S. Sherman, P. M. Sluss, T. J. de Villiers, S. E. Appt, V. L. Baker, F. J. Broekmans, M. I. Cedars, R. Greenblatt, S. Crawford, L. L. Sievert, L. Dennerstein, E. W. Freeman, M. Sammel, M. Gass, G. Hale, J. E. Hall, K. R. Hansen, S. D. Harlow, R. Little, P. Paramsothy, J. F. Randolph, N. Jaff, H. Joffe, J. Shifren, P. M. Sluss, R. Lobo, M. Warren, P. Maki, K. O'Connor, N. F. Woods, R. Rebar, G. Richard-Davis, D. M. Robertson, S. Sherman, C. N. Soares, H. Su, J. Romaguera, W. Utian, H. VandenBrink, T. J. de Villiers, M. T. Weber, and M. F. Wellons. Executive summary of the Stages of Reproductive Aging Workshop + 10: addressing the unfinished agenda of staging reproductive aging. *J. Clin. Endocrinol. Metab.*, 97(4):1159–1168, Apr 2012.

[101] A. Horiuchi, K. Itoh, M. Shimizu, I. Nakai, T. Yamazaki, K. Kimura, A. Suzuki, I. Shiozawa, N. Ueda, and I. Konishi. Toward understanding the natural history of ovarian carcinoma development: a clinicopathological approach. *Gynecol. Oncol.*, 88(3):309–317, Mar 2003.

[102] U. Del Monte. Does the cell number 10^9 still really fit one gram of tumor tissue? *Cell Cycle*, 8(3):505–506, Feb 2009.

[103] L. Carduner, C. R. Picot, J. Leroy-Dudal, L. Blay, S. Kellouche, and F. Carreiras. Cell cycle arrest or survival signaling through v integrins, activation of PKC and ERK1/2 lead to anoikis resistance of ovarian cancer spheroids. *Exp. Cell Res.*, 320(2):329–342, Jan 2014.

[104] H. Xing, S. Wang, K. Hu, W. Tao, J. Li, Q. Gao, X. Yang, D. Weng, Y. Lu, and D. Ma. Effect of the cyclin-dependent kinases inhibitor p27 on resistance of ovarian cancer multicellular spheroids to anticancer chemotherapy. *J. Cancer Res. Clin. Oncol.*, 131(8):511–519, Aug 2005.

[105] Z. Lu, R. Z. Luo, Y. Lu, X. Zhang, Q. Yu, S. Khare, S. Kondo, Y. Kondo, Y. Yu, G. B. Mills, W. S. Liao, and R. C. Bast. The tumor suppressor gene ARHI regulates autophagy and tumor dormancy in human ovarian cancer cells. *J. Clin. Invest.*, 118(12):3917–3929, Dec 2008.

[106] R. J. Correa, Y. R. Valdes, T. G. Shepherd, and G. E. DiMattia. Beclin-1 expression is retained in high-grade serous ovarian cancer yet is not essential for autophagy induction in vitro. *J Ovarian Res*, 8:52, Aug 2015.

[107] R. F. Schwarz, C. K. Ng, S. L. Cooke, S. Newman, J. Temple, A. M. Piskorz, D. Gale, K. Sayal, M. Murtaza, P. J. Baldwin, N. Rosenfeld, H. M. Earl, E. Sala, M. Jimenez-Linan, C. A. Parkinson, F. Markowetz, and J. D. Brenton. Spatial and temporal heterogeneity in high-grade serous ovarian cancer: a phylogenetic analysis. *PLoS Med.*, 12(2):e1001789, Feb 2015.

[108] A. Diaz, M. R. Laufer, and L. L. Breech. Menstruation in girls and adolescents: using the menstrual cycle as a vital sign. *Pediatrics*, 118(5):2245–2250, Nov 2006.

[109] J. A. Ledermann, F. A. Raja, C. Fotopoulou, A. Gonzalez-Martin, N. Colombo, and C. Sessa. Newly diagnosed and relapsed epithelial ovarian carcinoma: ESMO Clinical Practice Guidelines for diagnosis, treatment and follow-up. *Ann. Oncol.*, 24 Suppl 6:24–32, Oct 2013.

[110] C. Bodelon, R. M. Pfeiffer, S. S. Buys, A. Black, and M. E. Sherman. Analysis of serial ovarian volume measurements and incidence of ovarian cancer: implications for pathogenesis. *J. Natl. Cancer Inst.*, 106(10), Oct 2014.

[111] D. Stirling, D. G. Evans, G. Pichert, A. Shenton, E. N. Kirk, S. Rimmer, C. M. Steel, S. Lawson, R. M. Busby-Earle, J. Walker, F. I. Lalloo, D. M. Eccles, A. M. Lucassen, and M. E. Porteous. Screening for familial ovarian cancer: failure of current protocols to detect ovarian cancer at an early stage according to the international Federation of gynecology and obstetrics system. *J. Clin. Oncol.*, 23(24):5588–5596, Aug 2005.

[112] B. B. Hermsen, R. I. Olivier, R. H. Verheijen, M. van Beurden, J. A. de Hullu, L. F. Massuger, C. W. Burger, C. T. Brekelmans, M. J. Mourits, G. H. de Bock, K. N. Gaarenstroom, H. H. van Boven, T. M. Mooij, and M. A. Rookus. No efficacy of annual gynaecological screening in BRCA1/2 mutation carriers; an observational follow-up study. *Br. J. Cancer*, 96(9):1335–1342, May 2007.

[113] V. McGuire, A. Felberg, M. Mills, K. L. Ostrow, R. DiCioccio, E. M. John, D. W. West, and A. S. Whittemore. Relation of contraceptive and reproductive history to ovarian cancer risk in carriers and noncarriers of BRCA1 gene mutations. *Am. J. Epidemiol.*, 160(7):613–618, Oct 2004.

[114] A. Antoniou, P. D. Pharoah, S. Narod, H. A. Risch, J. E. Eyfjord, J. L. Hopper, N. Loman, H. Olsson, O. Johannsson, A. Borg, B. Pasini, P. Radice, S. Manoukian, D. M. Eccles, N. Tang, E. Olah, H. Anton-Culver, E. Warner, J. Lubinski, J. Gronwald, B. Gorski, H. Tulinius, S. Thorlacius, H. Eerola, H. Nevanlinna, K. Syrjakoski, O. P. Kallioniemi, D. Thompson, C. Evans, J. Peto, F. Lalloo, D. G. Evans, and D. F. Easton. Average risks of breast and ovarian cancer associated with BRCA1 or BRCA2 mutations detected in case Series unselected for family history: a combined analysis of 22 studies. *Am. J. Hum. Genet.*, 72(5):1117–1130, May 2003.

[115] S. Jones, W. D. Chen, G. Parmigiani, F. Diehl, N. Beerenwinkel, T. Antal, A. Traulsen, M. A. Nowak, C. Siegel, V. E. Velculescu, K. W. Kinzler, B. Vogelstein, J. Willis, and S. D. Markowitz. Comparative lesion sequencing provides insights into tumor evolution. *Proc. Natl. Acad. Sci. U.S.A.*, 105(11):4283–4288, Mar 2008.

[116] R. Meza, J. Jeon, S. H. Moolgavkar, and E. G. Luebeck. Age-specific incidence of cancer: Phases, transitions, and biological implications. *Proc. Natl. Acad. Sci. U.S.A.*, 105(42):16284–16289, Oct 2008.

[117] S. Yachida, S. Jones, I. Bozic, T. Antal, R. Leary, B. Fu, M. Kamiyama, R. H. Hruban, J. R. Eshleman, M. A. Nowak, V. E. Velculescu, K. W. Kinzler, B. Vogelstein, and C. A. Iacobuzio-Donahue. Distant metastasis occurs late during the genetic evolution of pancreatic cancer. *Nature*, 467(7319):1114–1117, Oct 2010.

[118] D. Bell, A. Berchuck, M. Birrer, J. Chien, D. Cramer, F. Dao, R. Dhir, P. DiSaia, H. Gabra, P. Glenn, A. Godwin, J. Gross, L. Hartmann, M. Huang, D. Huntsman, M. Iacocca, M. Imielinski, S. Kalloger, B. Karlan, D. Levine, G. Mills, C. Morrison, D. Mutch, N. Olvera, S. Orsulic, K. Park, N. Petrelli, B. Rabeno, J. Rader, B. Sikic, K. Smith-McCune, A. Sood, D. Bowtell, R. Penny, J. Testa, K. Chang, H. Dinh, J. Drummond, G. Fowler, P. Gunaratne, A. Hawes, C. Kovar, L. Lewis, M. Morgan, I. Newsham, J. Santibanez, J. Reid, L. Trevino, Y. Wu, M. Wang, D. Muzny, D. Wheeler, R. Gibbs, G. Getz, M. Lawrence, K. Cibulskis, A. Sivachenko, C. Sougnez, D. Voet, J. Wilkinson, T. Bloom, K. Ardlie, T. Fennell, J. Baldwin, S. Gabriel, E. Lander, L. L. Ding, R. Fulton, D. Koboldt, M. McLellan, T. Wylie, J. Walker, M. O'Laughlin, D. Dooling, L. Fulton, R. Abbott, N. Dees, Q. Zhang, C. Kandoth, M. Wendl, W. Schierding, D. Shen, C. Harris, H. Schmidt, J. Kalicki, K. Delehaunty, C. Fronick, R. Demeter, L. Cook, J. Wallis, L. Lin, V. Magrini, J. Hodges, J. Eldred, S. Smith, C. Pohl, F. Vandin, B. Raphael, G. Weinstock, E. Mardis, R. Wilson, M. Meyerson, W. Winckler, G. Getz, R. Verhaak, S. Carter, C. Mermel, G. Saksena, H. Nguyen, R. Onofrio, M. Lawrence, D. Hubbard, S. Gupta, A. Crenshaw, A. Ramos, K. Ardlie, L. Chin, A. Protopopov, J. Zhang, T. Kim, I. Perna, Y. Xiao, H. Zhang, G. Ren, N. Sathiamoorthy, R. Park, E. Lee, P. Park, R. Kucherlapati, M. Absher, L. Waite, G. Sherlock, J. Brooks, J. Li, J. Xu, R. Myers, P. W. Laird, L. Cope, J. Herman, H. Shen, D. Weisenberger, H. Noushmehr, F. Pan, T. Triche, B. Berman, D. Van Den Berg, J. Buckley, S. Baylin, P. Spellman, E. Purdom, P. Neuvial, H. Bengtsson, L. Jakkula, S. Durinck, J. Han, S. Dorton, H. Marr, Y. Choi, V. Wang, N. Wang, J. Ngai, J. Conboy, B. Parvin, H. Feiler, T. Speed, J. Gray, A. Levine, N. Socci, Y. Liang, B. Taylor, N. Schultz, L. Borsu, A. Lash, C. Brennan, A. Viale, C. Sander, M. Ladanyi, K. Hoadley, S. Meng, Y. Du, Y. Shi, L. Li, Y. Turman, D. Zang, E. Helms, S. Balu, X. Zhou, J. Wu, M. Topal, D. Hayes, C. Perou, G. Getz, D. Voet, G. Saksena, J. Zhang, H. Zhang, C. Wu, S. Shukla, K. Cibulskis, M. Lawrence, A. Sivachenko, R. Jing, R. Park, Y. Liu, P. Park, M. Noble, L. Chin, H. Carter, D. Kim, R. Karchin, P. Spellman, E. Purdom, P. Neuvial, H. Bengtsson, S. Durinck, J. Han, J. Korkola, L. Heiser, R. Cho, Z. Hu, B. Parvin, T. Speed, J. Gray, N. Schultz, E. Cerami, B. Taylor, A. Olshen, B. Reva, Y. Antipin, R. Shen, P. Mankoo, R. Sheridan, G. Ciriello, W. Chang,

J. Bernanke, L. Borsu, D. Levine, M. Ladanyi, C. Sander, D. Haussler, C. Benz, J. Stuart, S. Benz, J. Sanborn, C. Vaske, J. Zhu, C. Szeto, G. Scott, C. Yau, K. Hoadley, Y. Du, S. Balu, D. Hayes, C. Perou, M. Wilkerson, N. Zhang, R. Akbani, K. Baggerly, W. Yung, G. Mills, J. Weinstein, R. Penny, T. Shelton, D. Grimm, M. Hatfield, S. Morris, P. Yena, P. Rhodes, M. Sherman, J. Paulauskis, S. Millis, A. Kahn, J. Greene, R. Sfeir, M. Jensen, J. Chen, J. Whitmore, S. Alonso, J. Jordan, A. Chu, J. Zhang, A. Barker, C. Compton, G. Eley, M. Ferguson, P. Fielding, D. Gerhard, R. Myles, C. Schaefer, K. Mills Shaw, J. Vaught, J. Vockley, P. Good, M. Guyer, B. Ozenberger, J. Peterson, and E. Thomson. Integrated genomic analyses of ovarian carcinoma. *Nature*, 474(7353):609–615, Jun 2011.

[119] M. C. Lloyd, J. J. Cunningham, M. M. Bui, R. J. Gillies, J. S. Brown, and R. A. Gatenby. Darwinian Dynamics of Intratumoral Heterogeneity: Not Solely Random Mutations but Also Variable Environmental Selection Forces. *Cancer Res.*, 76(11):3136–3144, Jun 2016.

[120] M. Gerlinger, A. J. Rowan, S. Horswell, M. Math, J. Larkin, D. Endesfelder, E. Gronroos, P. Martinez, N. Matthews, A. Stewart, P. Tarpey, I. Varela, B. Phillimore, S. Begum, N. Q. McDonald, A. Butler, D. Jones, K. Raine, C. Latimer, C. R. Santos, M. Nohadani, A. C. Eklund, B. Spencer-Dene, G. Clark, L. Pickering, G. Stamp, M. Gore, Z. Szallasi, J. Downward, P. A. Futreal, and C. Swanton. Intratumor heterogeneity and branched evolution revealed by multiregion sequencing. *N. Engl. J. Med.*, 366(10):883–892, Mar 2012.

[121] A. Pribluda, C. C. de la Cruz, and E. L. Jackson. Intratumoral Heterogeneity: From Diversity Comes Resistance. *Clin. Cancer Res.*, 21(13):2916–2923, Jul 2015.

[122] A. Sottoriva, I. Spiteri, S. G. Piccirillo, A. Touloumis, V. P. Collins, J. C. Marioni, C. Curtis, C. Watts, and S. Tavare. Intratumor heterogeneity in human glioblastoma reflects cancer evolutionary dynamics. *Proc. Natl. Acad. Sci. U.S.A.*, 110(10):4009–4014, Mar 2013.

[123] C. A. Sherman-Baust, K. G. Becker, W. H. Wood Iii, Y. Zhang, and P. J. Morin. Gene expression and pathway analysis of ovarian cancer cells selected for resistance to cisplatin, paclitaxel, or doxorubicin. *J Ovarian Res*, 4(1):21, Dec 2011.

[124] P. Borst. Cancer drug pan-resistance: pumps, cancer stem cells, quiescence, epithelial to mesenchymal transition, blocked cell death pathways, persisters or what? *Open Biol*, 2(5):120066, May 2012.

[125] J. G. Chen and S. B. Horwitz. Differential mitotic responses to microtubule-stabilizing and -destabilizing drugs. *Cancer Res.*, 62(7):1935–1938, Apr 2002.

[126] A. Janssen, E. Beerling, R. Medema, and J. van Rheenen. Intravital FRET imaging of tumor cell viability and mitosis during chemotherapy. *PLoS ONE*, 8(5):e64029, 2013.

[127] J. E. Hornick, J. R. Bader, E. K. Tribble, K. Trimble, J. S. Breunig, E. S. Halpin, K. T. Vaughan, and E. H. Hinchcliffe. Live-cell analysis of mitotic spindle formation in taxol-treated cells. *Cell Motil. Cytoskeleton*, 65(8):595–613, Aug 2008.

[128] J. Chien, R. Kuang, C. Landen, and V. Shridhar. Platinum-sensitive recurrence in ovarian cancer: the role of tumor microenvironment. *Front Oncol*, 3:251, Sep 2013.

[129] J.-G. Chen and S. B. Horwitz. Differential mitotic responses to microtubule-stabilizing and -destabilizing drugs. *Cancer research*, 62(7):1935–8, apr 2002.

[130] P. B. Schiff and S. B. Horwitz. Taxol stabilizes microtubules in mouse fibroblast cells. *Proceedings of the National Academy of Sciences of the United States of America*, 77(3):1561–5, mar 1980.

[131] R. F. Ozols, B. N. Bundy, B. E. Greer, J. M. Fowler, D. Clarke-Pearson, R. A. Burger, R. S. Mannel, K. DeGeest, E. M. Hartenbach, and R. Baergen. Phase III trial of carboplatin and paclitaxel compared with cisplatin and paclitaxel in patients with optimally resected stage III ovarian cancer: a Gynecologic Oncology Group study. *J. Clin. Oncol.*, 21(17):3194–3200, Sep 2003.

[132] M.J Piccart and Cardoso F. Progress in systemic therapy for breast cancer: an overview and perspectives. *European Journal of Cancer*, 1(2):56–69, Sep 2003.

[133] P. Bonomi, K.B. Kim, and Kugler J. Comparison of survival for stage IIIB versus IV non-small cell lung cancer (NSCLC) patients with etopiside-cisplatin versus taxol-cisplatin: an Eastern Cooperative Oncology (ECOG) Group trial. *Proceedings of the American Society of Clinical Oncology*, 16(2):623–631, Sep 2000.

[134] R. Woessner, B. Tunquist, C. Lemieux, E. Chlipala, S. Jackinsky, W. Dewolf, W. Voegtli, A. Cox, S. Rana, P. Lee, and D. Walker. ARRY-520, a novel KSP inhibitor with potent activity in hematological and taxane-resistant tumor models. *Anticancer Res.*, 29(11):4373–4380, Nov 2009.

[135] C. Hirschmann-Jax, A. E. Foster, G. G. Wulf, J. G. Nuchtern, T. W. Jax, U. Gobel, M. A. Goodell, and M. K. Brenner. A distinct ”side population” of cells with high drug efflux capacity in human tumor cells. *Proc. Natl. Acad. Sci. U.S.A.*, 101(39):14228–14233, Sep 2004.

[136] R. Aneja, J. Zhou, S. N. Vangapandu, B. Zhou, R. Chandra, and H. C. Joshi. Drug-resistant T-lymphoid tumors undergo apoptosis selectively in response to an antimicrotubule agent, EM011. *Blood*, 107(6):2486–2492, Mar 2006.

[137] J. Shi and T. J. Mitchison. Cell death response to anti-mitotic drug treatment in cell culture, mouse tumor model and the clinic. *Endocr. Relat. Cancer*, 24(9):T83–T96, Sep 2017.

[138] I. Marzo and J. Naval. Antimitotic drugs in cancer chemotherapy: promises and pitfalls. *Biochem. Pharmacol.*, 86(6):703–710, Sep 2013.

[139] J. R. Jackson, D. R. Patrick, M. M. Dar, and P. S. Huang. Targeted anti-mitotic therapies: can we improve on tubulin agents? *Nat. Rev. Cancer*, 7(2):107–117, Feb 2007.

[140] E. A. Perez. Microtubule inhibitors: Differentiating tubulin-inhibiting agents based on mechanisms of action, clinical activity, and resistance. *Mol. Cancer Ther.*, 8(8):2086–2095, Aug 2009.

[141] D. Fanale, G. Bronte, F. Passiglia, V. Calo, M. Castiglia, F. Di Piazza, N. Barraco, A. Cangemi, M. T. Catarella, L. Insalaco, A. Listi, R. Maragliano, D. Massihnia, A. Perez, F. Toia, G. Cicero, and V. Bazan. Stabilizing versus destabilizing the microtubules: a double-edge sword for an effective cancer treatment option? *Anal Cell Pathol (Amst)*, 2015:690916, 2015.

[142] E. Mukhtar, V. M. Adhami, and H. Mukhtar. Targeting microtubules by natural agents for cancer therapy. *Mol. Cancer Ther.*, 13(2):275–284, Feb 2014.

[143] X. S. Ye, L. Fan, R. D. Van Horn, R. Nakai, Y. Ohta, S. Akinaga, C. Murakata, Y. Yamashita, T. Yin, K. M. Credille, G. P. Donoho, F. F. Merzoug, H. Li, A. Aggarwal, K. Blanchard, and E. H. Westin. A Novel Eg5 Inhibitor (LY2523355) Causes Mitotic Arrest and Apoptosis in Cancer Cells and Shows Potent Antitumor Activity in Xenograft Tumor Models. *Mol. Cancer Ther.*, 14(11):2463–2472, Nov 2015.

[144] C. F. Brogdon, F. Y. Lee, and R. M. Canetta. Development of other microtubule-stabilizer families: the epothilones and their derivatives. *Anticancer Drugs*, 25(5):599–609, May 2014.

[145] P. Cheetham and D. P. Petrylak. Tubulin-targeted agents including docetaxel and cabazitaxel. *Cancer J*, 19(1):59–65, 2013.

[146] M. N. Islam and M. N. Iskander. Microtubulin binding sites as target for developing anticancer agents. *Mini Rev Med Chem*, 4(10):1077–1104, Dec 2004.

[147] M. A. Jordan and L. Wilson. Microtubules as a target for anticancer drugs. *Nat. Rev. Cancer*, 4(4):253–265, Apr 2004.

[148] J. Shi, J. D. Orth, and T. Mitchison. Cell type variation in responses to antimitotic drugs that target microtubules and kinesin-5. *Cancer Res.*, 68(9):3269–3276, May 2008.

[149] H. C. Huang, T. J. Mitchison, and J. Shi. Stochastic competition between mechanistically independent slippage and death pathways determines cell fate during mitotic arrest. *PLoS ONE*, 5(12):e15724, Dec 2010.

[150] M. E. Bekier, R. Fischbach, J. Lee, and W.R. Taylor. Length of mitotic arrest induced by microtubule-stabilizing drugs determines cell death after mitotic exit. *Molecular cancer therapeutics*, 8(6):1646–1654, 2009.

[151] K. E. Gascoigne and S. S. Taylor. Cancer cells display profound intra- and interline variation following prolonged exposure to antimitotic drugs. *Cancer Cell*, 14(2):111–122, Aug 2008.

[152] C.F. Aspinall, D. Zheleva, A. Tighe, and S. S. Taylor. Mitotic entry: Non-genetic heterogeneity exposes the requirement for Plk1. *Oncotarget*, 6(34):36472–88, nov 2015.

[153] K. O. Hain, D. J. Colin, S. Rastogi, L. A. Allan, and P. R. Clarke. Prolonged mitotic arrest induces a caspase-dependent DNA damage response at telomeres that determines cell survival. *Sci Rep*, 6:26766, May 2016.

[154] J. D. Orth, Y. Tang, J. Shi, C. T. Loy, C. Amendt, C. Wilm, F. T. Zenke, and T. J. Mitchison. Quantitative live imaging of cancer and normal cells treated with Kinesin-5 inhibitors indicates significant differences in phenotypic responses and cell fate. *Mol. Cancer Ther.*, 7(11):3480–3489, Nov 2008.

[155] D.A. Brito and C. L. Rieder. The ability to survive mitosis in the presence of microtubule poisons differs significantly between human nontransformed (RPE-1) and cancer (U2OS, HeLa) cells. *Cell Motility and the Cytoskeleton*, 66(8):437–447, aug 2009.

[156] C. Topham, A. Tighe, P. Ly, O. J. Sansom, D. W. Cleveland, A. Bennett, O. Sloss, L. Nelson, R. A. Ridgway, D. Huels, S. Littler, C. Schandl, Y. Sun, B. Bechi, D. J. Procter, and S.S. Taylor. MYC Is a Major Determinant of Mitotic Cell Fate. *Cancer Cell*, 28:129–140, 2015.

[157] D. J. Colin, K. O. Hain, L. A. Allan, and P. R. Clarke. Cellular responses to a prolonged delay in mitosis are determined by a DNA damage response controlled by Bcl-2 family proteins. *Open Biol*, 5(3):140156, Mar 2015.

[158] H. J. Choi and B. T. Zhu. Role of cyclin B1/Cdc2 in mediating Bcl-XL phosphorylation and apoptotic cell death following nocodazole-induced mitotic arrest. *Mol. Carcinog.*, 53(2):125–137, Feb 2014.

[159] H. J. Choi, M. Fukui, and B. T. Zhu. Role of cyclin B1/Cdc2 up-regulation in the development of mitotic prometaphase arrest in human breast cancer cells treated with nocodazole. *PLoS ONE*, 6(8):e24312, 2011.

[160] R. H. Chisholm, T. Lorenzi, A. Lorz, A. K. Larsen, L. N. de Almeida, A. Escargueil, and J. Clairambault. Emergence of drug tolerance in cancer cell populations: an evolutionary outcome of selection, nongenetic instability, and stress-induced adaptation. *Cancer Res.*, 75(6):930–939, Mar 2015.

[161] H. Enderling and M. A. Chaplain. Mathematical modeling of tumor growth and treatment. *Curr. Pharm. Des.*, 20(30):4934–4940, Oct 2014.

[162] W. Wang, Y. Quan, Q. Fu, Y. Liu, Y. Liang, J. Wu, G. Yang, C. Luo, Q. Ouyang, and Y. Wang. Dynamics between cancer cell subpopulations reveals a model coordinating with both hierarchical and stochastic concepts. *PLoS ONE*, 9(1):e84654, 2014.

[163] G.G. Powathil, M.A. Chaplain, and M. Swat. Investigating the development of chemotherapeutic drug resistance in cancer: a multiscale computational study. *IET Systems Biology*, 1(1):1–23, Jun 2015.

[164] A. Lorz, T. Lorenzi, M.E. Hochberg, J. Clairambault, and B. Perthame. Populational adaptive evolution, chemotherapeutic resistance and multiple anti-cancer therapies. *ESAIM. Mathematical Modelling and Numerical Analysis*, 47(8):377–399, 2013.

[165] B. Basse, B. C. Baguley, E. S. Marshall, W. R. Joseph, B. van Brunt, G. Wake, and D. J. Wall. A mathematical model for analysis of the cell cycle in cell lines derived from human tumors. *J. Math. Biol.*, 47(4):295–312, Oct 2003.

[166] L. Spinelli, A. Torricelli, P. Ubezio, and B. Basse. Modelling the balance between quiescence and cell death in normal and tumour cell populations. *Math Biosci*, 202(2):349–370, Aug 2006.

[167] J. M. Greene, D. Levy, K. L. Fung, P. S. Souza, M. M. Gottesman, and O. Lavi. Modeling intrinsic heterogeneity and growth of cancer cells. *J. Theor. Biol.*, 367:262–277, Feb 2015.

[168] J. M. Greene, D. Levy, S. P. Herrada, M. M. Gottesman, and O. Lavi. Mathematical Modeling Reveals That Changes to Local Cell Density Dynamically Modulate Baseline Variations in Cell Growth and Drug Response. *Cancer Res.*, 76(10):2882–2890, May 2016.

[169] William R. Determining the birth function for an age structured population. *Mathematical Population Studies*, 1(4):377–395, 1989. PMID: 12281955.

[170] Michael P. and William R. Determining the initial age distribution for an age structured population. *Mathematical Population Studies*, 3(1):3–20, 1991. PMID: 12343114.

[171] F. Bekkal Brikci, J. Clairambault, B. Ribba, and B. Perthame. An age-and-cyclin-structured cell population model for healthy and tumoral tissues. *J. Math. Biol.*, 57(1):91–110, Jul 2008.

[172] M. Gyllenberg and F. Webb. A nonlinear structured population model of tumor growth with quiescence. *J. Math. Biol.*, 28(6):671–694, 1990.

[173] O. Arino and M. Kimmel. Asymptotic analysis of models of cell production systems. *Math. Modeling*, 7(6):1269–1300, 1986.

[174] O. Arino and M. Kimmel. Asymptotic analysis of a cell cycle model based on unequal division. *SIAM J. Appl. Math.*, 47(6):128–145, 1987.

[175] H. Y. Kueh, Y. Zhu, and J. Shi. A simplified Bcl-2 network model reveals quantitative determinants of cell-to-cell variation in sensitivity to anti-mitotic chemotherapeutics. *Sci Rep*, 6:36585, Nov 2016.

[176] M. V. Blagosklonny. Mitotic arrest and cell fate: why and how mitotic inhibition of transcription drives mutually exclusive events. *Cell Cycle*, 6(1):70–74, Jan 2007.

[177] J. D. Orth, A. Loewer, G. Lahav, and T. J. Mitchison. Prolonged mitotic arrest triggers partial activation of apoptosis, resulting in DNA damage and p53 induction. *Mol. Biol. Cell*, 23(4):567–576, Feb 2012.

[178] L. A. Allan and P. R. Clarke. Phosphorylation of caspase-9 by CDK1/cyclin B1 protects mitotic cells against apoptosis. *Mol. Cell*, 26(2):301–310, Apr 2007.

[179] Y. Hou, L. A. Allan, and P. R. Clarke. Phosphorylation of XIAP by CDK1-cyclin-B1 controls mitotic cell death. *J. Cell. Sci.*, 130(2):502–511, Jan 2017.

[180] X. Jiang, H. Li, P. Zhao, J. Xie, D. Khabele, J. Xu, and J. C. Gore. Early Detection of Treatment-Induced Mitotic Arrest Using Temporal Diffusion Magnetic Resonance Spectroscopy. *Neoplasia*, 18(6):387–397, Jun 2016.

[181] M. V. Blagosklonny. Mitotic arrest and cell fate: why and how mitotic inhibition of transcription drives mutually exclusive events. *Cell Cycle*, 6(1):70–74, Jan 2007.

[182] C. A. Messam and R. N. Pittman. Asynchrony and commitment to die during apoptosis. *Exp. Cell Res.*, 238(2):389–398, Feb 1998.

[183] I. Vorobjev and N. S. Barteneva. Temporal Heterogeneity Metrics in Apoptosis Induced by Anticancer Drugs. *J. Histochem. Cytochem.*, 63(7):494–510, Jul 2015.

[184] J. M. Eichhorn, A. Kothari, and T. C. Chambers. Cyclin B1 overexpression induces cell death independent of mitotic arrest. *PLoS ONE*, 9(11):e113283, 2014.

[185] J. M. Eichhorn, N. Sakurikar, S. E. Alford, R. Chu, and T. C. Chambers. Critical role of anti-apoptotic Bcl-2 protein phosphorylation in mitotic death. *Cell Death Dis*, 4:e834, Oct 2013.

[186] K. E. Gascoigne and S. S. Taylor. How do anti-mitotic drugs kill cancer cells? *Journal of Cell Science*, 122(15), 2009.

[187] R. Dixit and B. Gold. Inhibition of N-methyl-N-nitrosourea-induced mutagenicity and DNA methylation by ellagic acid. *Proc. Natl. Acad. Sci. U.S.A.*, 83(21):8039–8043, Nov 1986.

[188] Developmental Therapeutics Program (DTP-NCI). NCI-60 Human Tumor Cell Lines. `http://dtp.nci.nih.gov/`, 2015. [Online; accessed January-16-2017].

[189] L. M. Zasadil, K. A. Andersen, D. Yeum, G. B. Rocque, L. G. Wilke, A. J. Tevaarwerk, R. T. Raines, M. E. Burkard, and B. A. Weaver. Cytotoxicity of paclitaxel in breast cancer is due to chromosome missegregation on multipolar spindles. *Sci Transl Med*, 6(229):229ra43, Mar 2014.

[190] B. A. Weaver. How Taxol/paclitaxel kills cancer cells. *Mol. Biol. Cell*, 25(18):2677–2681, Sep 2014.

[191] H. A. Coller, L. Sang, and J. M. Roberts. A new description of cellular quiescence. *PLoS Biol.*, 4(3):e83, Mar 2006.

[192] N. Kangwan, J. M. Park, E. H. Kim, and K. B. Hahm. Chemoquiescence for ideal cancer treatment and prevention: where are we now? *J Cancer Prev*, 19(2):89–86, Jun 2014.

[193] N. Moore and S. Lyle. Quiescent, slow-cycling stem cell populations in cancer: a review of the evidence and discussion of significance. *J Oncol*, 2011, 2011.

[194] J. E. Visvader and G. J. Lindeman. Cancer stem cells in solid tumours: accumulating evidence and unresolved questions. *Nat. Rev. Cancer*, 8(10):755–768, Oct 2008.

[195] M. A. Dickson and G. K. Schwartz. Development of cell-cycle inhibitors for cancer therapy. *Curr Oncol*, 16(2):36–43, Mar 2009.

[196] G. I. Shapiro and J. W. Harper. Anticancer drug targets: cell cycle and checkpoint control. *J. Clin. Invest.*, 104(12):1645–1653, Dec 1999.

[197] G. Deep and R. Agarwal. New combination therapies with cell-cycle agents. *Curr Opin Investig Drugs*, 9(6):591–604, Jun 2008.

[198] J. R. Jackson, D. R. Patrick, M. M. Dar, and P. S. Huang. Targeted anti-mitotic therapies: can we improve on tubulin agents? *Nat. Rev. Cancer*, 7(2):107–117, Feb 2007.

[199] H. L. Gomez, M. Philco, P. Pimentel, M. Kiyan, M. L. Monsalvo, M. G. Conlan, K. G. Saikali, M. M. Chen, J. J. Seroogy, A. A. Wolff, and R. D. Escandon. Phase I dose-escalation and pharmacokinetic study of ispinesib,

a kinesin spindle protein inhibitor, administered on days 1 and 15 of a 28-day schedule in patients with no prior treatment for advanced breast cancer. *Anticancer Drugs*, 23(3):335–341, Mar 2012.

[200] H. Katayama and S. Sen. Aurora kinase inhibitors as anticancer molecules. *Biochim. Biophys. Acta*, 1799(10-12):829–839, 2010.

[201] J. Shi, Y. Zhou, H. C. Huang, and T. J. Mitchison. Navitoclax (ABT-263) accelerates apoptosis during drug-induced mitotic arrest by antagonizing Bcl-xL. *Cancer Res.*, 71(13):4518–4526, Jul 2011.

[202] I. Marzo and J. Naval. Antimitotic drugs in cancer chemotherapy: promises and pitfalls. *Biochem. Pharmacol.*, 86(6):703–710, Sep 2013.

[203] K. S. Chan, C. G. Koh, and H. Y. Li. Mitosis-targeted anti-cancer therapies: where they stand. *Cell Death Dis*, 3:e411, Oct 2012.

[204] O. Rath and F. Kozielski. Kinesins and cancer. *Nat. Rev. Cancer*, 12(8):527–539, Jul 2012.

[205] C. McInnes and M. D. Wyatt. PLK1 as an oncology target: current status and future potential. *Drug Discov. Today*, 16(13-14):619–625, Jul 2011.

[206] J. W. Purcell, J. Davis, M. Reddy, S. Martin, K. Samayoa, H. Vo, K. Thomsen, P. Bean, W. L. Kuo, S. Ziyad, J. Billig, H. S. Feiler, J. W. Gray, K. W. Wood, and S. Cases. Activity of the kinesin spindle protein inhibitor ispinesib (SB-715992) in models of breast cancer. *Clin. Cancer Res.*, 16(2):566–576, Jan 2010.

[207] H. C. Huang, J. Shi, J. D. Orth, and T. J. Mitchison. Evidence that mitotic exit is a better cancer therapeutic target than spindle assembly. *Cancer Cell*, 16(4):347–358, Oct 2009.

[208] P. Galan-Malo, L. Vela, O. Gonzalo, R. Calvo-Sanjuan, L. Gracia-Fleta, J. Naval, and I. Marzo. Cell fate after mitotic arrest in different tumor cells is determined by the balance between slippage and apoptotic threshold. *Toxicol. Appl. Pharmacol.*, 258(3):384–393, Feb 2012.

[209] W. Tao, V. J. South, Y. Zhang, J. P. Davide, L. Farrell, N. E. Kohl, L. Sepp-Lorenzino, and R. B. Lobell. Induction of apoptosis by an inhibitor of the mitotic kinesin KSP requires both activation of the spindle assembly checkpoint and mitotic slippage. *Cancer Cell*, 8(1):49–59, Jul 2005.

[210] A. L. Blajeski, V. A. Phan, T. J. Kottke, and S. H. Kaufmann. G(1) and G(2) cell-cycle arrest following microtubule depolymerization in human breast cancer cells. *J. Clin. Invest.*, 110(1):91–99, Jul 2002.

[211] O. Sloss, C. Topham, M. Diez, and S. Taylor. Mcl-1 dynamics influence mitotic slippage and death in mitosis. *Oncotarget*, 7(5):5176–5192, Feb 2016.

[212] D. A. Brito and C. L. Rieder. Mitotic Checkpoint Slippage in Humans Occurs via Cyclin B Destruction in the Presence of an Active Checkpoint. *Current Biology*, 16(12):1194–1200, Jun 2006.

[213] Y. Choi. Taxol-induced growth arrest and apoptosis is associated with the upregulation of the Cdk inhibitor, p21WAF1/CIP1, in human breast cancer cells. *Oncology Reports*, September 2012.

[214] N. Bah, L. Maillet, J. Ryan, S. Dubreil, F. Gautier, A. Letai, P. Juin, and S. Barille-Nion. Bcl-xL controls a switch between cell death modes during mitotic arrest. *Cell Death Dis*, 5:e1291, Jun 2014.

[215] S. Barille-Nion, N. Bah, E. Vequaud, and P. Juin. Regulation of cancer cell survival by BCL2 family members upon prolonged mitotic arrest: opportunities for anticancer therapy. *Anticancer Res.*, 32(10):4225–4233, Oct 2012.

[216] P. L. Bedard, A. R. Hansen, M. J. Ratain, and L. L. Siu. Tumour heterogeneity in the clinic. *Nature*, 501(7467):355–364, Sep 2013.

[217] V. Bavetsias and S. Linardopoulos. Aurora Kinase Inhibitors: Current Status and Outlook. *Front Oncol*, 5:278, 2015.

[218] R. Lowry. VassarStats. `http://vassarstatsnet/kw5.html`, 2017. [Online; accessed 15-May-2017].

[219] R. Lowry. VassarStats. `http://www.vassarstats.net/utest.html`, 2017. [Online; accessed 15-May-2017].

[220] A. Mjaavatten. MATLAB function polyfix(x,y,n,xfix,yfix,xder,dydx). `https://wwwmathworkscom/matlabcentral/fileexchange/54207-polyfix-x-y-n-xfix-yfix-xder-dydx-.l`, 2015. [Online; accessed 15-May-2017].

[221] L. M. Zasadil, E. M. Britigan, S. D. Ryan, C. Kaur, D. J. Guckenberger, D. J. Beebe, A. R. Moser, and B. A. Weaver. High rates of chromosome missegregation suppress tumor progression but do not inhibit tumor initiation. *Mol. Biol. Cell*, 27(13):1981–1989, Jul 2016.

[222] A. Bennett, O. Sloss, C. Topham, L. Nelson, A. Tighe, and S. S. Taylor. Inhibition of Bcl-xL sensitizes cells to mitotic blockers, but not mitotic drivers. *Open Biol*, 6(8), Aug 2016.

[223] O. Sloss, C. Topham, M. Diez, and S. Taylor. Mcl-1 dynamics influence mitotic slippage and death in mitosis. *Oncotarget*, 7(5):5176–5192, Feb 2016.

[224] L. A. Diaz-Martinez, Z. N. Karamysheva, R. Warrington, B. Li, S. Wei, X. J. Xie, M. G. Roth, and H. Yu. Genome-wide siRNA screen reveals coupling between mitotic apoptosis and adaptation. *EMBO J.*, 33(17):1960–1976, Sep 2014.

[225] S. B. Kaye. Progress in the treatment of ovarian cancer-lessons from homologous recombination deficiency-the first 10 years. *Ann. Oncol.*, 27 Suppl 1:i1–i3, Apr 2016.

[226] E. Dean, M. R. Middleton, T. Pwint, H. Swaisland, J. Carmichael, P. Goodege-Kunwar, and M. Ranson. Phase I study to assess the safety and tolerability of olaparib in combination with bevacizumab in patients with advanced solid tumours. *Br. J. Cancer*, 106(3):468–474, Jan 2012.

[227] H. Liu, H. W. Zhang, X. F. Sun, X. H. Guo, Y. N. He, S. D. Cui, and Q. X. Fan. Tamoxifen-resistant breast cancer cells possess cancer stem-like cell properties. *Chin. Med. J.*, 126(16):3030–3034, Aug 2013.